A study of selected problems related to accidental process fires

A doctoral dissertation

by

Leiv Anfin Drange

Submitted in partial fulfillment of
the requirements for the degree of

Philosophiae Doctor

Faculty of Mathematics and Natural Sciences - Department of
Physics and Technology - Process Technology Section
University of Bergen
N-5007 Bergen, Norway

January 2011

Preface

This thesis is the final part of the work on my PhD that has lasted over a decade. It is strange how much change a person experience through a period like this. My wife, Wenche Irene, and I, have four children. During this period they have added more than 40 years of life experience to their minds.

I bought my first mobile telephone about ten years ago. At that time we had one TV set at home and no computer. Now, there are six telephones, five computers and four TVs. The children can communicate with their friends through microphone, camera and keyboard. Watching these rapid changes certainly underlines the fact that knowledge becomes updated and outdated very fast.

In the early stages of the project, the experiments were put on hold, waiting for the propane test rig to be built. In our first experiment, using brand new radiometers, my fellow student, Zia Kazemi, and I, managed to lose four out of ten. The jet fire was more powerful than we anticipated.

Teaching myself typesetting using LaTeX, has been another side effect of working with the PhD. When I graduated from the University of Strathclyde in 1987, even TeX, the language that LaTeX is based upon, was not made. Today´s students at UiB use LaTeX in their undergraduate studies. I have gained skills, at different levels, using MatLab, Kameleon FireEx, FLACS, Fortran, AutoCAD and Autodesk Inventor. In order to do this, I have worked on a set of different platforms: Windows 95, -98, NT, XP + Linux, UNIX and finally Mac OSX, which has been used for most of this thesis. In that sense, the work with this PhD has become an update of my undergraduate studies, where we saved our Basic programming files on cassette tapes.

This tiny contribution to the available knowledge of accidental process fires has been obtained through a scholarship at Stord/Haugesund University College. It was an obvious choice to contact the environment around Prof.Rolf Eckhoff at the University of Bergen in order to get the process running. His program for process technology was very relevant for my studies.

The work has mainly been carried out in Haugesund, Res$\dot{Q}$, Ølensvåg, the Norwegian Ocean, and at home, in Etne at the Norwegian west coast.

Etne, January 10, 2011

Leiv Anfin Drange

Acknowledgements

I would first and foremost express a sincere gratitude for love and continuous support from my beloved wife, Wenche Irene, for her never ending patience during the time I have spent working on the PhD. Wenche Irene has helped to keep me going, as well as handling the logistics that comes with running a family with four children.

I am also deeply grateful for the support and advise from my excellent supervisor, Prof. Rolf Eckhoff, at the University of Bergen (UiB). He has been of great help, both in terms of organizing the path through the formal system, and guiding me in the right directions experimental wise. His knowledge has been of invaluable importance.

Prof. Torgrim Log at Stord/Haugesund University College, who has offered excellent supervision, motivation and shown a sincere interest in the field of gas jet fires. He has a remarkable eye for understanding a problem, both experimental and theoretical, and finding a way to solve it.

Dr. Bjørn Johan Arntzen at UiB, who has been of great help throughout the project period. He has acted both as supervisor for the experimental/thesis part, as well as a lecturer in one of the taught subjects.

Dr. Kees van Wingerden was of great help in the early stage, before moving abroad. In cooperation with Prof. Eckhoff, he contributed in getting the project onto the path that ended with this thesis.

I would like to address special thanks to dr. Zia Kazemi for months of work at our joint project of characterizing the jet flame in the first half of Part I. Kazemi and I contributed with equal amounts of work, both scientifically and practically in this part of the project. Most of all, I wish to thank dr. Kazemi for the many fruitful theoretical and practical discussions and actions during the experimental period.

This has been an expensive project. Without my former employer SHUC (Stord/Haugesund University College), it would not have been possible to build the gas rig, purchase the experimental equipment, make the test cylinder etc. I am greatly thankful both for the financial support and the confidence they showed in me, by recommending me for the scholarship.

The list of contributors whom I owe sincere thanks is long, and I want to mention the following in particular:
-Dr.Monika Metallinou, for running the project of building the gas rig
-Mr.Gisle Kleppe, who always managed to help when I had problems with LabView, and gave valuable advice regarding instrumentation
-Mr.Arjen Kraaijeveld, who helped with many lab. related issues
-Res$\dot{Q}$, the safety center where all the experimental works in Parts I and II of

this thesis were carried out
-Mr. Olav Vågen and Mr. Jomar Brakedal at Res$\dot{Q}$, for all practical help during experiments
-Mr. Arthur Abell at Saipem S.p.A, for all help with the offshore measurements in Part III, and valuable discussions regarding heat absorption in water curtains
-Statoil/Hydro, for allowing the heat radiation measurements from the water curtain project to be published
-West Contractors AS, my employer, for allowing me to continue working on the full scale flare project after the system was built and handed over to the customer. I am also grateful for the financial support of the high speed photography of water droplets, and financing a period working on the project in 2008

ZK denotes Zia Kazemi, LAD denotes Leiv Anfin Drange

Part I, heat transfer to cylinder, was carried out entirely by LAD
Part II was carried out entirely by LAD
Part III was carried out entirely by LAD

Co-author declaration:

Part I, flame characterisation, was a joint project between ZK and LAD, with an approximately 50% participation from each, as shown below:

Activity	**Contributor(s) and comments**
1. Building the propane gas rig	Dr. Monika Metallinou was the project leader, ZK and LAD contributed only with proposals for the design criteria for the rig
2. Experiments	Definitely the largest part of the project. ZK and LAD contributed with an equal amount of work in this part. It included planning, running all procedures for the rig, instrumentation and set-up for experiments, running experiments, logging, repair work etc, i.e all activities carried out at the test site
3. Calibration of instruments	ZK did all the calibration,
4. Plotting of experimental results	LAD made all plots, but in cooperation with ZK
5. Photographs/figures of experimental setup etc	ZK and LAD contributed with an equal amount of work. Both used the same photo- and video cameras, and ZK/LAD have agreed on shared rights
6. Simulations	ZK made all simulations, but in cooperation with LAD
7. Plotting of simulated results	ZK made all plots generated by KFX/excel. LAD made all plots generated by MatLab
8. Writing poster paper	LAD wrote the first LaTex version, in cooperation with ZK. Towards the end, the file was exchanged back and forth with contributions from both

13.01.11 Torgrim Log

Summary

An experimental full scale characterization of a turbulent propane jet flame has been made in terms of temperatures and radiation. Sonic propane gas releases were achieved at steady pressure and near steady flow. Commercial propane was used, consisting of a mixture of propane with very small admixtures of sulphur and methanol. The size of the fire was 13-14MW (average burning rate 0,3kg/s). The pressure drop across the horizontally mounted nozzle was 10.3 barg. The experimental setup was simulated using the CFD-code Kameleon FireEx, and characterizations were made for temperature, radiation and gas velocity. The results from experiments and simulations were compared using interpolation techniques for reducing the errors of measurements, and MatLab for visualization. Both transient and time-averaged values were plotted. The main findings in this work were:

- the length of the visible flame was $\approx 5.5m$, with a lift-off distance of $0.6m$
- the highest temperature region of the jet flame was $\approx 70\%$ along the visible flame length (i.e not including lift-off). The maximum temperature in the flame was in the region $1200 - 1300^0C$
- up to $\approx 3m$, there was a fuel rich region along the centre trajectory of the flame, where the temperature was $\approx 200^0C$ less than in the stoichiometric region, $0.3m$ away from the centre line
- the radiation fraction along the jet trajectory at positions 25%, 50%, 70%, and 95% downstream of the visible flame length was 28%, 57%, 73%, and 63%, respectively
- moving outside the flame perpendicular to the jet axis, the radiation fraction gradually increased. At $3m$ distance from the centerline, it was equal to the total heat flux. This indicated that the convection fraction was close to zero
- the radiation heat flux sensors were extremely sensitive to unclean environment. Even when applying nitrogen for purging, it did not keep the soot and other particles away from the inner surface of the gauge's restrictor
- the CFD-code KFX predicted a correct flame length, but estimated a slightly shorter lift-off distance
- the end part of the KFX-flame was more influenced by buoyancy and deviated some from that of the experiment

- the measurements showed more irregular shaped temperature fields compared to the simulated
- the measurements showed larger fluctuations in the temperature fields compared to the simulated
- the maximum measured radiative heat flux inside the flame was $185 kW/m^2$. The maximum simulated radiative heat flux was $193 kW/m^2$, representing a deviation of 4.3%
- the maximum measured total heat flux was $256 kW/m^2$

A steel cylinder of radius $160 mm$ was placed at various positions in the jet, and the relative heat transfer was assessed by means of thermocouples placed radially inside the cylinder. This work showed that:

- convection is the major contributor to the total heat transfer from a turbulent jet flame to a steel cylinder impinged by the flame
- the largest rate of heat transfer is at the side facing the flame, i.e no high levels of turbulence induced thermal loading could be detected at the back
- the heat transfer coefficient, h, is a function of the velocity of the gas flow relative to the impinged object

The stability of ignited propane gas jets, discharged from circular cross section outlets of varying diameters and inclinations were examined. This resulted in:

- a model, with an accuracy of 0.89, that predicts the upper and lower blowout limits for propane in gas phase, as well as a critical outlet diameter of $14 mm$
- no observations were made indicating that the outlet inclination has any effect on the blowout limits

The heat attenuation in water spray in a full scale offshore flare situation was examined by applying a known model for calculations and comparing with measurements. The result of this work was:

- the model predictions slightly under estimated the capacity of the water curtain. There were, however, uncertainties regarding the water curtain properties, and more detailed measurements are necessary in order to present a verified model for engineering use
- for the extreme situations of an underestimate of drop sizes, where the actual drop sizes are 50% larger than estimated, or where the actual small drop fraction is doubled, calculation errors will be caused in the range -7% to +18%, in absolute terms
- the calculation model is not capable of identifying irregularities within the water curtain. This will have importance relating to maximum allowable radiation limits where people are exposed

Nomenclature

A	area	[m^2]
a	constant in soot model	[-]
a	strain rate	[-]
a_o	constant in soot model	[-]
B	flame lift-off distance	[m]
b	constant in soot model	[-]
C	stoichiometric molar concentration of fuel	[mol/mol]
c	molar density	[mol/m^3]
c	molar concentration	[mol/mol]
C_p	heat capacity	[J/K]
c_p	specific heat capacity	[J/kgK]
C_μ	constant in $k-\varepsilon$ model	[-]
$C_{\varepsilon 1}$	constant in ε equation	[-]
$C_{\varepsilon 2}$	constant in ε equation	[-]
c	concentration	[kg/m^3]
$\mathcal{D}$	mass diffusivity	[m^2/s]
D	cylinder or sphere diameter, orifice diameter	[m]
D	mass diffusion coefficient	[-]
D_a	Damköhler number (θ/τ_c)	[-]
D_{aK}	Damköhler-Karlovitz number (τ/τ_c)	[-]
D_m	multi component binary diffusion coefficient	[-]
d	diameter	[m]
E	radiative power	[kW/m^2]
F	body forces	[N]
F	radiation fraction	[-]
F_r	Froude number	[-]
f	constant in soot model	[-]
f	mass concentration	[kg/kg]
f	acceleration	[m/s^2]
g	constant in soot model	[-]
g	gravitational acceleration	[m/s^2]
H	heat	[kJ/kg]
H	height	[m]
h	convective heat transfer coefficient	[W/m^2K]
h	static specific enthalpy	[J/kg=m^2/s^2]
h	heat of vaporization	[J/kg]
h	heat coefficient	[W/m^2K]
J	molar diffusion concentration	[mol/mol]

k	turbulent kinetic energy	[J/kg=m^2/s^2]
k	conductivity	[W/mK]
k	coorrection factor	[-]
K_a	Karlovitz number	[-]
L	length	[m]
l	characteristic turbulent length scale, thickness	[m]
j	diffusive mass flux	[kg/sm^2]
M_w	molecular weight of fuel	[g/mol]
M	molar mass	[g/mol]
m	molar ratio of reactants to products	[mol/mol]
m	molecular weight	[g/mol]
m	mass	[g]
N	soot particle concentration	[kg/kg]
n	radical nuclei concentration	[parts/m^{3}s]
n_o	spontaneous formation rate of radical nuclei	[parts/m^{3}s]
Nu	Nusselt number	[-]
P_k	production term in k equation	[W/kg=m^2/s^3]
p	static pressure	[N/m^2]
Pr	Prandtl number	[-]
Q	heat release	[W]
Q	flow	[kg/s]
q	dissipation in Cascade model	[W/kg=m^2/s^3]
q	energy	[J]
R	reaction rate	[mol/ls]
R	rate of formation	[parts/m^{3}s]
R	rate of particle formation	[kg/m^{3}s]
Re	Reynolds number	[-]
Re_K	turbulent Reynolds number ($=u'\lambda/\nu$)	[-]
R_i	Richardson number	[-]
R_M	ratio of source momentum to total momentum	[-]
r	oxidant-to-fuel weight ratio	[kg/kg]
r	radius	[m]
S	source term in basic flow eqn.	
S	surface emissive power	[kW/m^2]
S_h	reaction energy at static enthalpy	[kg/ms^3]
s	curvilinear distance along flame axis	[m]
T	temperature	[K]
t	time	[s]
U	total heat coefficient	[W/m^{2}K]
u	velocity	[m/s]
U	flow speed	[m/s]
U	overall heat transfer coefficient	[W/m^{2}K]
u	fluid or jet velocity	[m/s]
V	volume	[m^3]
v	Kolmogorov's micro velocity scale	[m/s]
v	velocity	[m/s]
W	mass fraction of fuel in stoichiometric mixture	[kg/kg]
W	width	[-]
w	energy transfer in Cascade model	[W/kg=m^2/s^3]
w	mass fraction	[kg/kg]
x	mole fraction	[mol/mol]
x	axis direction	
y	axis direction	
Y	mass fraction	[kg/kg]
z	axis direction	
z	non-dimensional radius (r/R)	[m/m]

Greek symbols

α	thermal diffusivity	[m^2/s]
β	shape factor or wetting parameter	[-]
χ	scalar dissipation rate	[-]
δ_t	thickness of a thermal layer	[m]
ε	dissipation rate of turbulent kinetic energy	[W/kg=m^2/s^3]
ϵ	surface emissivity, sensor absorptance	[-]
θ	turbulence time scale	[s]
θ	angle	[-]
δ	shape parameter	[-]
δ_{ij}	Kronecker-delta (=1 when $i = j$; =0 when $i \neq j$)	[-]
δ_L	laminar flame thickness	[m]
η	Kolmogorov length scale	[m]
λ	viscosity coefficient	[kg/ms]
λ	fraction (excess air number)	[-]
μ	dynamic molecular viscosity	[kg/ms]
ν	kinematic molecular viscosity	[m^2/s]
ψ	parameter	[-]
ξ	mixture fraction	[-]
ξ_{max}	maximum spread factor	[-]
ρ	density	[kg/m^3]
σ	Stefan-Boltzmann constant (5.67×10^{-8})	[W/m^2K^4]
σ	surface tension of drop	[N/m]
σ_ε	Schmidt number for dissipation ε	[-]
σ_k	Schmidt number for turbulence energy k	[-]
Φ	viscous dissipation function	[J/m^2kg]
ϕ	view factor	[-]
ϕ	axial coordinate in spherical coordinates	[m]
τ	atmospheric transmissivity	[-]
τ	Kolmogorov's micro time scale	[s]
τ	viscous shear tensor	[N/m^2]
τ	time scale	[s]
υ	stoichiometric coefficient	[-]
φ	a variable in the basic flow eqn.	[-]
ω	characteristic strain rate	[1/s]
ω	chemical kinetic reaction	[]

Superscripts

$'$	fluctuating value
$'$, $''$	characteristic turbulent scale
$''$	per unit area
$'''$	per unit volume
$*$	fine structure in EDC, critical value
$-$	mean value
$\hat{}$	dispersed phase quantity
$\cdot$	per second
$\rightarrow$	vector

Subscripts

0	initial value
a	air, average
b	boiling
c	convection, combustion, chemical, carbon
d	diffuse emitter
e	excess, exit, effective, expanded value
F	flame, furnace
f	liquid phase
fg	liquid-vapor phase
fu	fuel
g	vapor phase
h	heat flux gauge
i	inner, isotropic emitter, species i
j	species j
L	laminar, latent
o	outer, oxidizer
p	particle
pr	product
r	radiation
sat	saturation
s	surface
ss	steady state
t	turbulent, transient
v	vaporization
w	water, surface
∞	ambient

PART I - PROPERTIES OF PROPANE JET FLAMES; TEMPERATURE, RADIATION AND HEAT TRANSFER TO SOLIDS

Contents

List of Figures

List of Tables

Chapter 1

Introduction

The handling of combustible materials in the process industries require uttermost care, skills and attitude in order to prevent accidental fires. The consequences of fires in these industries are often severe, due to the high heat release rates often associated with combustion of many industrial materials.

Breakage of pipes containing pressurized gases, will normally produce discharges of powerful turbulent gas jets. If the gas is combustible, and a jet gets ignited, the combustion will be very fast due to the high rate of gas entrainment to the ambient air.

In these studies the pressure drop for propane in gas phase across a nozzle was increased compared to the vapor pressure at ambient temperature. It was done by increasing the pressure of propane in liquid phase, and evaporating it into gas phase by preheating prior to release. This increased the turbulence energy in the jet compared to a release at ambient temperature. The effects of these mechanisms were measured by placing a number of thermocouples, radiometers and total heat flux gauges, the latter two commonly called heat flux gauges, into and around the region of combustion. This part of the work was done in cooperation with fellow PhD student Zia Kazemi [1], [2], and a summary of the work was presented as a poster paper in the 10^{th} International Fire Science & Engineering Conference Interflam 2004, see appendix A.

The combustion processes follow patterns that can be described mathematically, both the physical mixing of reactants in a turbulent fluid flow, and the chemical reactions in terms of reaction times and heat releases.

A number of numerical models have been developed to predict fluid flow characteristics in general. Several computer simulation models use these as a foundation (e.g Flow-3D and CFD-ACE), often in combination with other software in order to visualize the results. To predict the behavior of combustion, fire and explosion, more specific models have been developed, e.g Kameleon FireEx, FLACS (explosion), SOFIE, SMARTFIRE, JASMINE and UNICORN. The models are verified by checking for consistency with experimental results.

The temperature and radiation from an undisturbed gas jet flame is of interest when assessing the thermal loads inflicted upon an object. But when the object itself is impinged by a jet flame, it will inflict with the flow, and even the combustion. This situation has been studied by inserting a steel cylinder into a propane jet flame. The cylinder axis was at 90^0 to the axis of the nozzle releasing the jet stream. During the temperature rise of the cylinder in the start

of the experiments, there is a non linear relation between convective/radiative heat transfer to the cylinder, and a corresponding and increasing radiative heat transfer away from the cylinder. Therefore, the centre of the cylinder was cooled by a water flow in order to obtain a steady heat flux being transported radially through the cylinder. Tests were carried out for different positions of the cylinder in the flame. Measurements were done around the circumference of the cylinder, as well as radially from near the outer surface to near the inner surface.

Chapter 2

Objects of work

Some of the major objects of this part of the work have been to provide detailed information of a propane jet flame, and to compare experimental results with results obtained by simulation of a high momentum turbulent jet flame, in order to validate the results obtained from simulations. The parameters of interest were temperature and radiation. Also, information of the velocities involved at different points in the flow field was of interest. However, there were no available equipment or method to measure this. Therefore, the fluid dynamic effects were studied only by simulation. But it was expected that the comparison between experiments and simulations for the other parameters would give useful information of how well the velocity was predicted. By obtaining a good consistency of results between experiments and simulations, confidence would be achieved in using related simulations in further studies where the fluid mechanics is involved.

The characterization was done for a $13-14MW$ propane gas jet flame. This included measuring the temperature and heat flux. The purpose of characterizing the flame was to understand the flame properties better both thermo- and aerodynamically and find the highest temperatures and the most erosive zones of the flame where a test object was to be located. Since erosion of a metal object is related to gas velocity, or more precisely, the convective heat transfer, both radiation and convection, inside and around the flame, was measured.

The pressure drop for propane in gas phase across the nozzle was increased compared to the vapor pressure at ambient temperature. It was done by increasing the pressure by preheating prior to release of propane in liquid phase, before evaporating it into gas phase. This increased the turbulent energy of the jet compared to a release at ambient temperature. The effects of these mechanisms were measured by placing a number of thermocouples, radiometers and total heat flux gauges, into and around the region of combustion.

Another object has been to investigate the heat transfer from a flame described above, onto a pipe, impinged by the flame. The aim was to point out the zones with the highest heat transfer, and the position of a pipe or tube in the flame that yielded the peak, heat transfer values. To simulate the pipe or tube, a steel cylinder was put into the flame, in different positions. The peak values for the heat transfer were assumed to be in the exact same radial zones as the peak values of the temperatures inside the cylinder.

The aim was to find out if the highest thermal loading was:

- where the pressure was highest, i.e where the cylinder was facing the flame, around the forward stagnation point
- where the flow velocity over the cylinder's surface was highest, i.e over the top and under the bottom
- somewhere else, e.g if the cylinder caused some unpredicted change in the flow, like new, large eddies, giving rise to a high thermal loading at the surface facing away from the flow, around the separation point, or any other unforeseen location

Chapter 3

Basic theory

3.1 Flame characterization

3.1.1 Introduction

An in depth, basic characterization of jet flames, is one of the major challenges for the participants of the fire science community. Attempts have been made to make models of flames by breaking down this phenomenon into single, different contributors, and put them back together again to form a close to nature description of the jet flame. This complex mixture of fluid flow, chemical reactions or heat transport are all varying with (differentials of) pressure, viscosity, temperature, geometry, velocity, the ambient etc.

An example: The fluid flow in a jet flame is turbulent. A description of the turbulence, without mixing of reactants or combustion, very fast becomes complex in itself. Even with today´s computing power, it is not possible to model a fluid flow, down to the interaction of the molecules. Large scale parameters are normally introduced, like length scales. Even the smallest, like the Kolmogorov length scale, is large in a molecular context. This scale can be regarded as the diameter of a whirl that is so small that it is about to dissipate, due to the viscous forces of the fluid.

Adding combustion into a model, will introduce different chemical reactants in the order of 10^2 for propane. For longer molecules, this number increases to an order of 10^3 (e.g upwards of butane) to 10^4 (e.g crude oil) [3]. One can easily see the complexity being built up by attempting to fully describe even the simplest examples of turbulent combustion. The use of models is therefore limited to a choice of which information that is of interest in a particular situation, and the availability of a well verified model suitable for the purpose.

The same applies to characterization of jet flames by doing measurements. Here, the challenge often is to collect information without disturbing the process itself. Some measurements are conducted from outside the combustion or flow zone, but others need to be done by positioning instruments near, or inside, this zone. In addition, instruments can only collect a limited amount of information.

Therefore, this chapter and chapter 4 will give a brief introduction to the topic of modeling and measuring jet flames, with a focus on what is relevant for the experimental apparatus and procedures described in chapter 5.

3.1.2 A qualitative characterization

Many different expressions have been used to describe the characteristics of jet fires. Terms like intensity, severity, torching, high velocities or localised impact have tended to become closely associated with jet fires. However, these properties can, to some extent, also be used to describe pool fires or fire balls. For example, a jet fire is often considered to be a high velocity fire, but also low velocity jet fires exist. These are from discharges of liquids with relatively low vapour pressure (butane upwards)[4]. The evaporating liquid jet persists for a considerable distance in the flame, and the actual gas velocities and air entrainment are similar to those in pool fires.

A jet fire can be described as ***"a turbulent diffusion flame resulting from the combustion of a fuel continuously released with some significant momentum in a particular range of directions"*** [4].

It has got zero inertia, i.e the flame reaches full intensity almost instantaneously, and it can be turned off very quickly. There are no feedback mechanisms like it is for pool fires, where the radiation from a flame causes an increased rate of evaporation of the liquid from the pool. As shown throughout this thesis, this does not mean that there is no radiation from a gas jet flame. It merely means that the radiation does not contribute to the jet flame´s own rate of release of combustibles.

3.1.3 Basic flow equations

A mathematical model of turbulent combustion will have to go through a verification of the quantities returned, by comparing them to experimental results. If there is a good correlation between a set of modeled and experimental results, it is acceptable to assume that the model can be used for prediction of the combustion inside the envelope of verified results. However, any extrapolation of results outside of this, is not recommended.

Modeling turbulent flow and combustion is basically a combination of transport equations, differentials of mass concentrations, chemical reactions, pressure and velocity. A general equation used to describe these differentials, is stated by Ertesvåg [5]:

$$\frac{\partial}{\partial t}(\rho\varphi) + \frac{\partial}{\partial x_j}(\rho\varphi u_j) = \frac{\partial}{\partial x_j}(-j_{\varphi,j}) + S_\varphi \tag{3.1}$$

This is the balance- or transport equation for some variable φ. It can be mass, momentum, energy or some statistical variable. The terms represent, from left to right: accumulation of φ; convective transport of φ; diffusive transport of φ and source term.

In the simulations performed as part of the experimental work in this thesis, the software Kameleon FireEx was used. This is a CFD code solving a k-ε model for the turbulent flow. The k-ε model is widely used, and verified for the experimental situation. The basic equations in this model are the same for turbulent and laminar flow.

For more details on modeling of turbulent flow and combustion, it is recommended to read Ertesvåg [5].

For a single phase flow, the equations of continuity and momentum are

$$\frac{\partial \rho}{\partial t} + \frac{\partial}{\partial x_j}(\rho u_j) = 0 \tag{3.2}$$

$$\frac{\partial}{\partial t}(\rho u_j) + \frac{\partial}{\partial x_j}(\rho u_i u_j) = -\frac{\partial p}{\partial x_i} + \frac{\partial \tau_{ij}}{\partial x_j} + \rho f_i \tag{3.3}$$

where ρ is density, t is time, x_j is axis direction j, u_j is velocity component in direction x_j, p is static pressure, τ_{ij} is stress tensor and f_i is acceleration due to distant forces.

3.1.4 Chemical reactions

Combustion is an oxidation of a fuel, often with air as oxidant. The simplest form of a chemical reaction can be written as:

mass of fuel + $\lambda \times$ mass of air $\rightarrow$ mass of product + $(\lambda - 1) \times$ mass of air

An example can be the combustion of propane in air[1]:

$$\begin{aligned} C_3H_8 + \lambda \times (5O_2 + 5 \times 3.76N_2) \rightarrow & \underbrace{3CO_2 + 4H_2O + 5 \times 3.76N_2}_{product} \\ & + \underbrace{(\lambda - 1) \times (5O_2 + 5 \times 3.76N_2)}_{excess\ air} \end{aligned} \tag{3.4}$$

This is a very simplified way of describing the complex chemistry involved in the combustion. The equation tells something about the starting point and the final result of the reactions, but nothing about what is going on in between. The main reaction is a sum of many intermediate steps, or elementary reactions. Many unstable, chemical compositions are formed, several hundreds for this reaction [3]. For propane burning in O_2, Warnatz [3] made a list of 231 elementary reactions. For the creation of NO, e.g for propane burning in air, another 82 elementary reactions were added. The intermediate chemical compounds react with other unstable compositions to form the end products. In addition, the reactions always go both forward and backward. This means that if product molecules collide with any chemical compound in the mixture, at a certain speed in certain direction(s), they will split up and form intermediate compositions or even the original fuel. In that sense, the above description of the reaction can be regarded as an uneven balance between chemical compounds, where the arrow points towards the side where the amount of material is the largest. Also, a set of low fraction compounds on the right side of the equation has been avoided. There will always be some CO, H_2, non combusted fuel, free radicals etc.

[1] $\lambda \geq 1$, is the excess air number, can also be expressed as excess fuel number, $\Phi = \lambda^{-1}$. The number 3.76 comes from the relative mole fractions of N_2 and O_2 in air ($\frac{79}{21}$)

For a system of N_R chemical reactions, including N_S materials A_k, the reaction equations can be written in the general form [5]:

$$\sum_{k=1}^{N_S} \nu_{kl}^{'} A_k \rightarrow \sum_{k=1}^{N_S} \nu_{kl}^{''} A_k, l = 1, ..., N_R \tag{3.5}$$

where $\nu_{kl}^{'}$ and $\nu_{kl}^{''}$ are stoichiometric coefficients for the material A_k in reaction l.

It is obvious that it will be hard to model the full chemistry mathematically for any geometry the size of the order of meters cubed. Therefore, modeling the chemistry is, at present, solved by using large scale parameters, such as the fraction of the different combustibles in a mixture, the rate of reaction for each fuel, or the total turbulence energy involved for the fuel/air mixture. These large scale parameters can be further described as probability densities in time and space, by using probability density functions, PDF´s. Repeated computations of the combustion by e.g Monte Carlo simulation can thus return a reasonably accurate result.

3.1.5 Turbulence modeling; the $k - \varepsilon$ model

The argument from the chemistry section above, for using large scale parameters, is also applied when modeling turbulence. Modeling the physical interaction between molecules, although it is less complex than for the chemistry, is still not obtainable. Therefore, a larger scale parameter like average turbulence energy, k, is defined. This is the kinetic energy pr. unit mass, and $k = \frac{1}{2}\overline{u_i' u_j'}$ for an average fluctuating fluid in motion. The dissipation of energy, ε, is defined as the average rate of loss of turbulence kinetic energy.

The turbulence causes an increased transport in the flow. In the momentum equation this can be regarded as an extra stress, or an additional viscosity [5]:

$$\tau_{eff} = \tau + \tau_{turb}; \quad \mu_{eff} = \mu + \mu_{turb} \tag{3.6}$$

The turbulence viscosity has a typical value of $\mu_{turb} = 100 - 500 \times \mu$. Therefore, for high Reynolds number flow, μ has little influence on the flow, i.e the turbulence is much more dominant than the viscous forces. However, for low Reynolds number flow, the viscous forces can have a significant influence on the flow. For this purpose, low Reynolds number models have been developed. Rotta has a viscous dissipation term, while Jones and Launder applies empirical functions of turbulence Reynolds numbers in order to adjust the constants in the model. By adding a smaller change as done by Launder and Sharma [6], this model is regarded as a standard [5]. Low Reynolds number models are not discussed further.

Time and length scales

Turbulent flows have characteristic time and length scales that are continuously spread over a specter. These scales are used to model a flow properly. For the length scales, it is important to model the smallest whirls in the turbulence, as these are of significant importance to e.g the mixing of materials and dissipation of energy. The size of this scale, the Kolmogorov scale, is determined by the viscous forces. The size can be regarded as the diameter of a whirl, so small, that it breaks up. It is the point at which the viscous forces take over, and the whirl ceases to exist. The energy from these small whirls are, at this stage, transferred to heat, i.e a faster molecular motion in the fluid.

The largest length scales determine the transport, or convection, of the materials involved. See subsection 3.1.6 for more details on scales. The total size of the geometry, and its subdivision into finite elements need to take the length scales into account. But the size of the elements do not have to be uniform. In simulations, one will normally reduce the size of the finite elements in areas with detailed geometry, e.g near obstacles.

Similar to the length scales, the time scales are important for modeling. The time scale for a characteristic flow speed, U, for the main flow, can be defined as

$$\tau_U = \frac{\eta}{U} \tag{3.7}$$

where τ_U is time and η is the Kolmogorov length scale, i.e this is the time it takes for the Kolmogorov length scale to flow passed a point in the flow field. This scale is less than the Kolmogorov time scale. The time resolution in the simulation must be less than τ_U [5]. Therefore, in simulations, one will normally reduce the time resolution for high velocity flows.

The first $k-\varepsilon$ model was published by Jones and Launder in 1972 [7]. This model could also be used for flows with low Reynolds numbers. The numerical values of these constants should be adjusted for the Reynolds number of the flow. The most applied version was the model published by Launder and Spalding in 1974 [8]. The model is developed for incompressible flow, i.e. for a constant density [1].

A $k-\varepsilon$ model that is regarded as a standard for flows with high Reynolds numbers is summarized by Ertesvåg [5], and is given as:

Turbulence viscosity:

$$\mu_t = \rho\nu_t = C_\mu \rho \frac{k^2}{\varepsilon} \tag{3.8}$$

Reynolds stresses:

$$-\rho\overline{u_i' u_j'} = \mu_t \left(\frac{\partial \overline{u}_i}{\partial x_j} + \frac{\partial \overline{u}_j}{\partial x_i} \right) - \frac{2}{3}\rho k \delta_{ij} \tag{3.9}$$

The turbulence (k) equation:

$$\frac{\partial}{\partial t}(\rho k) + \frac{\partial}{\partial x_j}(\rho k \overline{u}_j) = \frac{\partial}{\partial x_j}\left(\left(\mu + \frac{\mu_t}{\sigma_k} \right) \frac{\partial k}{\partial x_j} \right) + \rho P_k - \rho\varepsilon \tag{3.10}$$

The dissipation (ε) equation:

$$\frac{\partial}{\partial t}(\rho \varepsilon) + \frac{\partial}{\partial x_j}(\rho \varepsilon \overline{u}_j) = \frac{\partial}{\partial x_j}\left(\left(\mu + \frac{\mu_t}{\sigma_\varepsilon} \right) \frac{\partial \varepsilon}{\partial x_j} \right) + C_{\varepsilon 1}\frac{\varepsilon}{k}\rho P_k - C_{\varepsilon 2}\frac{\varepsilon}{k}\rho\varepsilon \tag{3.11}$$

where

$$\rho P_k = \mu_t \left(\frac{\partial \overline{u}_i}{\partial x_j} + \frac{\partial \overline{u}_j}{\partial x_i} \right) \frac{\partial \overline{u}_i}{\partial x_j}. \tag{3.12}$$

The numerical values of the constants are [5, 8]:

$$\sigma_k = 1.0 \quad \sigma_\varepsilon = 1.3 \quad C_{\varepsilon 1} = 1.44 \quad C_{\varepsilon 2} = 1.92 \quad C_\mu = 0.09 \tag{3.13}$$

Here, the three terms on the right-hand side of equations (3.10) and (3.11) represent the diffusion, production, and dissipation terms respectively.

Adjustments of the $k-\varepsilon$ model for combustion purposes

In combustion, the density of the fluid varies significantly, due to the temperature differences in the flow. In that case, the equation for the Reynolds stresses (3.9) takes the form [5]:

$$-\overline{\rho u_i' u_j'} = -\rho\widetilde{u_i' u_j'} = \mu_t \left(\frac{\partial \tilde{u}_i}{\partial x_j} + \frac{\partial \tilde{u}_j}{\partial x_i} \right) - \frac{2}{3} \left(\overline{\rho}\tilde{k} + \mu_t \frac{\partial \tilde{u}_l}{\partial x_l} \right) \delta_{ij} \tag{3.14}$$

The "tilde" notation (e.g $\widetilde{u_i' u_j'}$) is to express that the turbulence and dissipation energies are mass weighed.

Similarly, the equation for the production term (3.12) becomes [5]:

$$\overline{\rho} P_k = \mu_t \left(\frac{\partial \tilde{u}_i}{\partial x_j} + \frac{\partial \tilde{u}_j}{\partial x_i} \right) \frac{\partial \tilde{u}_i}{\partial x_j} - \frac{2}{3} \left(\overline{\rho}\tilde{k} + \mu_t \frac{\partial \tilde{u}_l}{\partial x_l} \right) \frac{\partial \tilde{u}_i}{\partial x_i} \tag{3.15}$$

3.1.6 Characterization of turbulent flames

As discussed in several of the former sections, chemical reactions and turbulent flow, separately, are complicated phenomena. Combining the two, makes it even more complicated to model turbulent combustion at a molecular level. Warnatz, Maas and Dibble [3] suggest that even in the hypothetical case where a full DNS (direct numerical simulation) were obtainable, one would most likely average the time dependent output to obtain what is typically desired: average fuel consumption, average power, average pollutant formation etc. Thus, the need for applying characteristic *scales*, *parameters* and *flow regimes*, is enhanced:

Scales

For large turbulence structures the velocity scale is u', the length scale ℓ' and the time scale $\theta = \ell'/u'$. Thus, the resulting Reynolds number is $Re_{\ell'} = u'\ell'/\nu$. The Taylor length scale λ gives the $Re_\lambda = u'\lambda/\nu \sim Re_{\ell'}^{1/2}$. In non premixed flames, θ is characteristic time for mixing of the reactants [1].

The Kolmogorov microscale has a defined velocity scale v, length scale η and time scale τ [5]. In this case, there is no need to define a scale with fluctuating properties, as for the large structures, since it is the smallest dimension that forms this scale. By definition $v = (\nu/\tau)^{1/2}$ and $\eta = (\nu\tau)^{1/2}$. These scales are characteristic for motions with large dissipation of turbulence energy, i.e. where the viscous forces are large. The Reynolds number based on Kolmogorov's length scale is $Re_K = u'\eta/\nu$.

The relations between large and small turbulence scales are [5]:

-length scale: $\ell'/\eta \sim Re_\lambda^{3/2} \sim Re_{\ell'}^{3/4}$

-time scale: $\theta/\tau \sim Re_{\ell'}^{1/2}$

-Reynolds numbers: $Re_K \sim Re_\lambda^{1/2} \sim Re_{\ell'}^{1/4}$

Parameters

It is often found useful to express some parameters in terms of a ratio of another parameter, in order to produce new non dimensional parameters. This helps generalizing results, and thus make them more widely applicable. From the Reynolds number above, there is a relation between the length scales η/δ_L and ℓ'/δ_L; the velocity scales u'/u_L; time scales: $Da = \theta/\tau_c$ and $Da_K = \tau/\tau_c$. The last two expressions are called Damköhler number, the latter is also called Karlovitz number K_a. For a rapid chemical reaction (small τ_c) the Damköhler number is large [1].

The relationships between these groups can be calculated as [1]:

$$\frac{u'}{u_L} \sim Re_{\ell'} \cdot \frac{\delta_L}{\ell'} \sim Re_{\ell'}^{-1/4} \cdot \frac{\delta_L}{\eta}, \tag{3.16}$$

$$Da_K = \frac{\tau}{\tau_c} \sim \left(\frac{\eta}{\delta_L}\right)^2 \sim Da \cdot Re_{\ell'}^{-1/2}, \tag{3.17}$$

$$Da = \frac{\theta}{\tau_c} \sim \frac{\ell'}{\delta_L}\frac{u_L}{u'} \sim \left(\frac{\ell'}{\delta_L}\right)^2 Re_{\ell'}^{-1} \sim \left(\frac{\eta}{\delta_L}\right)^2 Re_{\ell'}^{1/2}, \tag{3.18}$$

$$\frac{\ell'}{\delta_L} \sim Re_{\ell'}^{3/4}\left(\frac{\eta}{\delta_L}\right). \tag{3.19}$$

Other examples of non dimensional parameters applicable to flow are: The Froude number, $Fr = \frac{U^2}{gL}$, which is the ratio of inertia and gravitational forces, Richardson number, $Ri = \frac{g}{\rho}\frac{d\rho}{dx_3}\left(\frac{du_1}{dx_3}\right)^{-2}$, the ratio of potential to kinetic energy, Stanton number, $\frac{h}{c_p \rho V}$, the ratio of heat transferred into a fluid to the thermal capacity of the fluid, and Prandtl number, the ratio of momentum diffusivity (kinematic viscosity) to the thermal diffusivity.

Flow regimes

Starting with the lower part of the Borghi diagram in figure 3.1, where the flow velocity is relatively small, a laminar flame front can be considered as a thin, flat reaction zone. With fast reactions, as for propane (small τ_c and δ_L, large u_L) and a weak turbulence(large θ, τ, ℓ', small u'), the reaction will take place in layers as for laminar combustion, causing a wrinkled reaction zone [5].

Moving up in the Borghi diagram, by increasing the fluctuations, the wrinkles become pockets and larger wrinkles. The combustion still takes place in zones, but but the zones are thicker, and a number of small flames called flamelets, can be observed.

When the turbulence gets intense (small θ, τ, ℓ', large u') and slow reactions (large τ_c, small u_L), the reactions will take place over a wide reaction volume. In an idealized case, where the flame covers the whole combustion space, it is called a "perfectly stirred reactor" [5].

A connection between the different regimes can be seen in a Borghi diagram for turbulent non premixed flames (differs a little from the similar diagram for premixed flames) [5]:

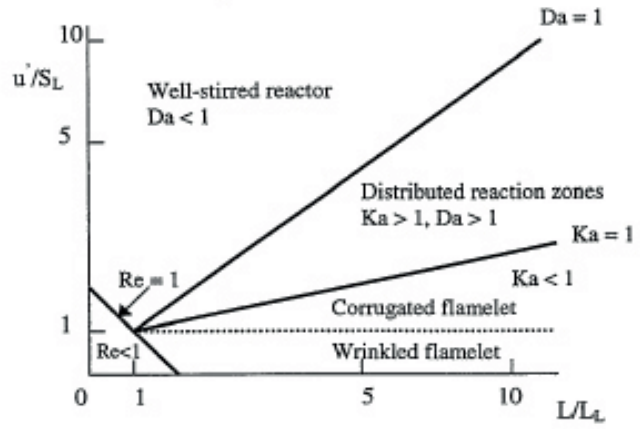

Figure 3.1: Borghi diagram for turbulent non premixed flames. The horizontal axis is the ratio of the turbulent integral scale and laminar flame thickness; the vertical axis is the ratio of the turbulent velocity fluctuation and the laminar flame speed, from Zhang [9]

The Karlovitz number, $Ka = t_{ch}/t_K$, is an important parameter in this diagram. Here, t_{ch} is the chemical time scale, and t_K is the micro turbulent time scale associated with the small eddies at the Kolmogorov dissipation scale. The Damköhler number, $Da = t_t/t_{ch}$, where t_t is the integral time scale of turbulence. In the regime where $Ka < 1$, the turbulent flame can be observed as a "brush" of laminar flames, and can be modeled using the flamelet models which have been developed extensively during the past decades. Outside of this regime, the intensity of turbulence is sufficiently large compared to the reaction rate, thus resulting in a "thick" distributed flame and local quenching. This is a regime where turbulence competes with chemical reaction on all scales [9]. Borghi uses the lines $Ka = 1$ and $Da = 1$ as limits between the three principal types of flame. For $Ka < 1$, the flame is "wrinkled". For $Da < 1$, the flame is "thickened" (well stirred reactor), and in the intermediate region, where both Da and $Ka > 1$, the flame is "wrinkled-thickened" [10]. An example of a thickened flame is given in figure 3.2. A flame becomes thickened at the stage where the average thickness of the thickened flamelet becomes equal to the integral length scale of the turbulence.

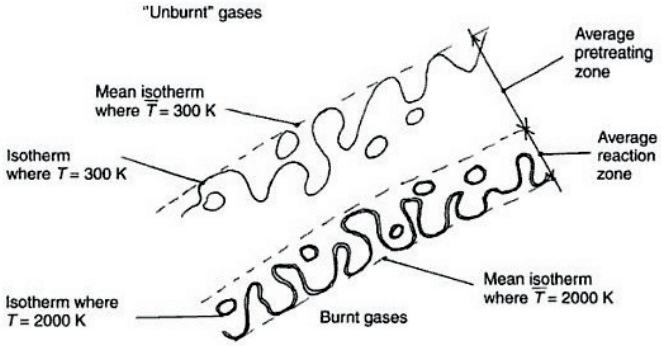

Figure 3.2: Instantaneous view of thickened flame, from Borghi [10]

3.2 Heat transfer to a cross flow cylinder

3.2.1 A general description of convection

Due to the difference in temperature of a flame and the surface of an object impinged by the flame, convective heat transfer will occur from the flame to the surface. The convection will vary over the surface of the object, due to the variation in radiation from the flame at different positions, varying flow over the surface, and these factors varying with time for a turbulent flow [11]. The general equation for a local heat flux q'', called Newton's law of cooling, is:

$$q'' = h(T_s - T_\infty) \tag{3.20}$$

where h is the local heat transfer coefficient, T_s and T_∞ are surface and flame temperatures, respectively. Both q'' and h varies with temperature, see section 4.2 for a more detailed discussion. The total heat flux rate q may be obtained by integrating the local fluxes over the entire surface, i.e.:

$$q = \int_{A_s} q'' \, dA_s \tag{3.21}$$

or, from equation 3.20:

$$q = (T_s - T_\infty) \int_{A_s} h \, dA_s \tag{3.22}$$

Due to the temperature difference, a thermal boundary layer between the solid and the flame is developed. At the surface, the temperature of the solid and the gases are the same. But at distances $y > 0$, away from the solid, the temperature is gradually higher with increasing y.

Since the velocity of the gases at the surface is zero, the energy transfer here, only occurs by conduction, and the *local* heat flux can be expressed by applying Fourier's law to the fluid at $y = 0$:

$$q_s'' = -k_\infty \left.\frac{\partial T}{\partial y}\right|_{\mathbf{y=0}} \tag{3.23}$$

By combining equation 3.23 with Newton's law of cooling, equation 3.20, an expression for the convective heat transfer coefficient is obtained:

$$h = \frac{-k_\infty \frac{\partial T}{\partial y}|_{y=0}}{T_s - T_\infty} \tag{3.24}$$

Hence, conditions in the thermal boundary layer, which strongly influence the wall temperature gradient $-k_\infty \frac{\partial T}{\partial y}|_{y=0}$, determine the rate of heat transfer across the boundary layer.

An example of a thermal layer over an isothermal, horizontal surface, is shown in figure 3.3 below. Note that the solid in this case is of a higher temperature than the free stream fluid [11].

Since $(T_s - T_\infty)$ is a constant, independent of a lateral distance x from the position where a flame hits the object, while the thickness of the thermal layer, δ_t, increases with increasing x, temperatures in the boundary layer must decrease with increasing x, and it follows that q_s'' and h decrease with increasing x.

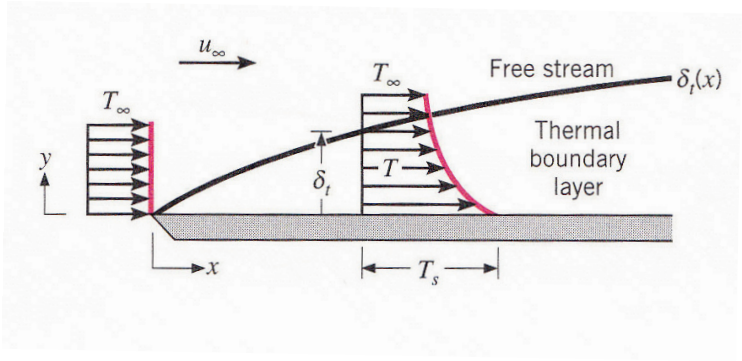

Figure 3.3: An example of a thermal layer over an isothermal, horizontal surface. In the case shown, the surface has got a higher temperature than the free stream gas, giving rise to the thermal layer of thickness δ_t at a distance x, from the tip, from Incropera/DeWitt [11]

The principle is the same for a flame impinging a surface. But the temperature variation is reverted. Still, δ_t, increases with increasing x, but temperatures in the boundary layer increase with increasing x. And, opposite of the example in figure 3.3, q_s'' and h increase with increasing x.

3.2.2 The circular cylinder in a cross flow

The flow studied in this work, is the external flame impingement on a circular steel cylinder. The impingement is normal to the axis of the cylinder. As shown in the general description of a cross flow case, figure 3.4, the flow is brought to rest at the forward stagnation point, with an accompanying rise in pressure. From this point, the pressure decreases with increasing x, the streamline coordinate, and the boundary layer, defined by the distance from the surface to the point where $u = 0.99u_\infty$, develops under the influence of a favorable pressure gradient ($dp/ds < 0$). But the pressure must at some stage reach a minimum, and toward the rear of the cylinder, further boundary layer occurs in the presence of an adverse pressure gradient ($dp/dx > 0$). In figure 3.4, the distinction between the upstream velocity V and the free stream velocity u_∞ should be noted. The value of u_∞ can now be larger or smaller than V, depending on the streamline distance x from the forward stagnation point.

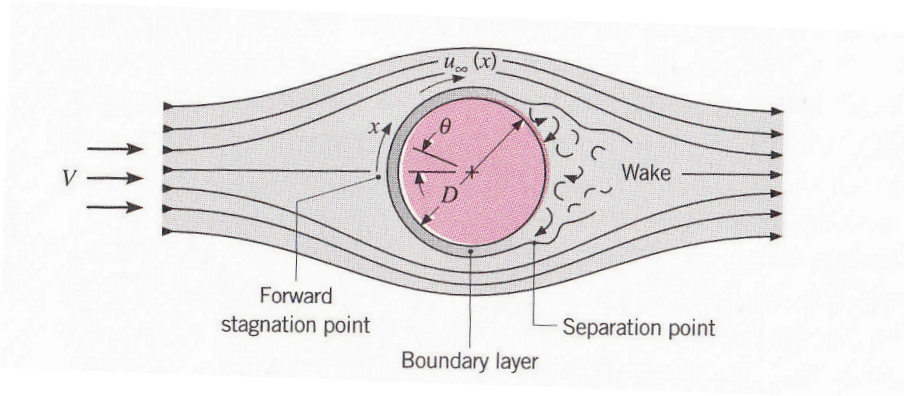

Figure 3.4: Boundary layer formation and separation on a circular cylinder in cross flow. The gas velocity = 0 at the stagnation point and is >V over the top and under the bottom. At the separation point, the flow becomes turbulent, from Incropera/DeWitt [11]

From Euler's equation for an inviscid flow, $u_\infty(x)$ must exhibit behavior opposite to that of $p(x)$. That is, from $u_\infty = 0$ at the forward stagnation point, the fluid accelerates because of the favorable pressure gradient ($du_\infty/dx > 0$ when $dp/dx < 0$), reaches a maximum velocity when $dp/dx < 0$, and decelerates as a result of the adverse pressure gradient ($du_\infty/dx < 0$ when $dp/dx > 0$). As the fluid decelerates, the velocity gradient at the surface, $\frac{\partial u}{\partial y}|_{y=0}$, eventually becomes zero, see figure 3.5. At this location, termed the separation point, fluid near the surface lacks sufficient momentum to overcome the pressure gradient, and continued downstream movement is impossible. Since the oncoming fluid also precludes flow back upstream, boundary layer separation must occur. This is shown as the separation point in figure 3.5. It is characterized by the condition $(\frac{\partial u}{\partial y})_s = 0$. The downstream side of the separation point is called the wake.

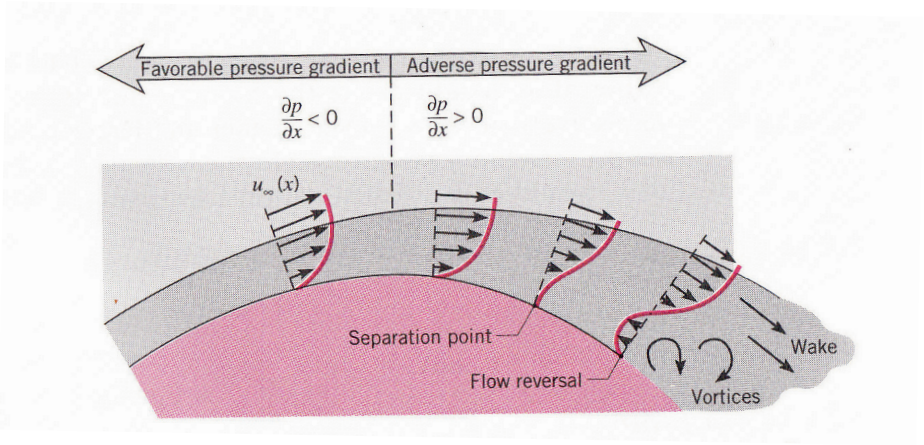

Figure 3.5: Velocity profile associated with separation on a circular cylinder in cross flow. The point at which the flow is just about to go in the reverse direction, is called the separation point. Beyond this point, vortices are formed and thus produce turbulence, from Incropera/DeWitt [11]

3.2.3 The Nusselt number, - a significant parameter in convection

When dealing with convection, the term called the *Nusselt number*, Nu, is an important parameter. It is defined as, [11]:

$$Nu \equiv \frac{hL}{k_f} = +\frac{\partial T^*}{\partial y^*}\bigg|_{y^*=0} \tag{3.25}$$

This parameter is equal to the dimensionless temperature gradient at the surface, and it provides a measure of the convection heat transfer occuring at the surface. For a *prescribed geometry*,

$$Nu = f(x^*, Re_L, Pr) \tag{3.26}$$

The Nusselt number is to the boundary layer what the friction coefficient is to the velocity boundary layer. Equation 3.26 implies that, for a given geometry, the Nusselt number must be some universal function of x^*, Re_L and Pr. If this function were known, it could be used to compute the value of Nu for different fluids and for different values of V and L. From knowledge of Nu, the local convection coefficient h may be found and the local heat flux may then be computed from equation 3.20.

Since the *average* heat transfer coefficient is obtained by integrating over the surface of the solid, it must be independent of the spatial variable x^*. Hence, the functional dependence of the *average* Nusselt number, is:

$$\overline{Nu} = \frac{\overline{h}L}{k_f} = f(Re_L, Pr) \tag{3.27}$$

The value of the expression above, states that heat transfer results, whether obtained theoretically or experimentally, can be represented in terms of three dimensionless groups. Once the form of the functional dependence of equation 3.27 has been obtained for a particular surface geometry, e.g from experiments, it is known to be *universally* applicable. This means it may be applied for different fluids, velocities and length scales, as long as the assumptions implicit in the originating boundary layer equations remain valid (like negligible viscous dissipation and body forces).

3.2.4 The effect of turbulence

The transition of the boundary layer discussed in section 3.2.2, which influences the position of the separation point, is dependent of the Reynolds number. For a circular cylinder, the characteristic length is the diameter, and the Reynolds number is defined as:

$$Re_D \equiv \frac{\rho V D}{\mu} = \frac{V D}{\nu} \tag{3.28}$$

Since the momentum of fluid in a turbulent boundary layer is larger than in a laminar boundary layer, it is reasonable to expect transition to delay the occurrence of separation. If $Re_D \leq 2\times10^5$, the boundary layer remains laminar, and separation occurs at $\theta \approx 80^0$, as shown in figure 3.6. If $Re_D \geq 2 \times 10^5$, boundary layer transition occurs, and separation is delayed to $\theta \approx 140^0$.

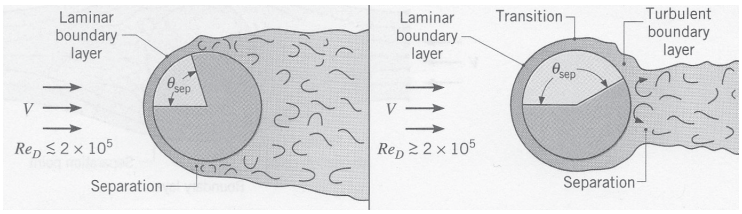

Figure 3.6: The effect of turbulence on separation. The figure shows that with increasing Reynolds number, i.e increasing turbulence, the separation point is moved downstream. The angle of separation, θ_{sep}, between the stagnation point, the centre of the cylinder, and the separation point, will thus increase with increasing turbulence, from Incropera/DeWitt [11]

3.2.5 Jet impingement from a single round nozzle

An example of a gas jet being discharged from a round nozzle of diameter D, into a quiescent ambient, is shown in figure 3.7. The figure is general, and also show discharge from a rectangular slot of width W [11], which is of lesser interest in this case. The jet is turbulent, and at the nozzle exit, is characterized by a uniform velocity profile. With increasing distance from the nozzle, the

momentum exchange between the jet and the ambient causes the free boundary of the jet to broaden, and the potential core, within which the maximum (center) velocity decreases with increasing distance from the nozzle exit. The region of the flow over which conditions are unaffected by the impingement surface is termed the *free* jet.

Within the impingement zone, flow is influenced by the target surface and is decelerated and accelerated in the normal z and transverse r or x directions, respectively. However, since the flow continues to entrain zero momentum fluid from the ambient, horizontal acceleration cannot continue indefinitely, and accelerating flow in the stagnation zone is transformed to a decelerating wall jet. Hence, with increasing r, or x, velocity components parallel to the surface increase from a value of zero to some maximum, before it decays to zero. Velocity profiles within the wall jet are characterized by zero velocity at both the impingement and free surfaces. If $T_s \neq T_e$, convection heat transfer occurs in both the stagnation and wall jet regions.

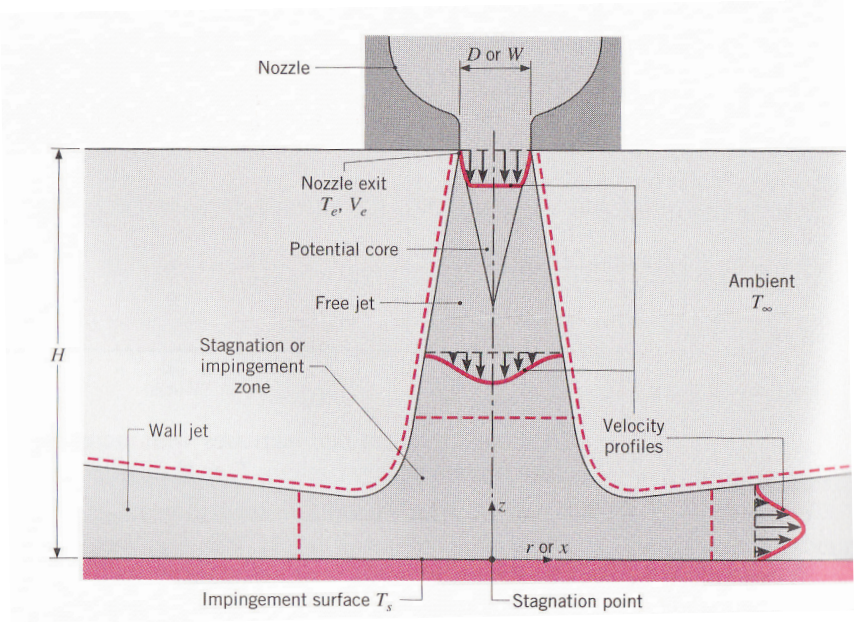

Figure 3.7: Surface impingement of a single round (or slot) gas jet. The area limited by the red stapled lines from the nozzle and the horizontal red stapled line, is called the free jet. Below this point, the flow is affected by the impingement area, and eventually diverted into a horizontal, but still turbulent, flow, from Incropera/DeWitt [11]

Chapter 4

Previous work; flames and heat transfer

A basic theory is, in many ways, a review of the previous work done in a field being studied. One may ask why there is a need for extending the basic theory into a review chapter. But the purpose is to update the description of the field with the latest reported findings.

4.1 Characterization of jet flames

4.1.1 Flame lengths

In this study, the characterization of the propane jet flames have been made mainly in terms of temperatures and radiation, but also the flame lengths have been assessed. Cumber and Spearpoint ([12], 2006) present a model for flame length assessment of propane jet fires. The model will not be reproduced here, but in a thorough discussion, the authors point out the problems of defining where a flame starts, and where it ends. Research in this area has mainly focused on identifying the most important dimensionless groups and the development of flame length correlations. An example of this is Heskestad's model ([13], 1983):

$$\frac{f_{L,M}}{D} = (15.6N^{1/5} - 1.02)R_M \tag{4.1}$$

where R_M represents the ratio of the source momentum to the total momentum, including that due to buoyancy, and is given by:

$$R_M = \frac{\dot{m}_0 U_0}{\int_0^\infty \rho u^2 2\pi r \, dr} \tag{4.2}$$

N relates to the dimensionless heat release rate $\dot{Q}^*$, sometimes called the fire Froude number, given by:

$$N = \left(\frac{r c_p T_{amb}}{H_{fu}}\right)^3 \dot{Q}^{*2} \tag{4.3}$$

Becker and Liang ([14], 1978) chose to correlate their flame length measurements using a Richardson number,

$$Ri^{1/3} = \xi_L = \left(\frac{g}{D^2(\rho_0/\rho_{amb})U_0^2} \right)^{1/3} f_L \tag{4.4}$$

and a parameter, ψ

$$\psi = \frac{D(\rho_0/\rho_{amb})^{0.5}\beta}{f_L m_{fu,st}} \tag{4.5}$$

where

$$\beta = \left(\frac{M_{w,air}T_{adia,st}}{M_{w,prod}T_{amb}} \right)^{0.5} \tag{4.6}$$

For propane, β is approximately 2.8 [14]. Using ψ and ξ_L, Becker and Liang showed that their flame length measurements collapsed onto the curve

$$\psi = 0.18 + 0.022\xi_L \tag{4.7}$$

Hawthorne et al. ([15], 1949) derived a correlation for the flame length in the high momentum limit, that is dependent of the ratio of the flame temperature to the ambient air temperature, and the flame stoichiometry. Defining flame lengths relating to some dimensionless parameter, most often a ratio of two parameters of the same dimension(s), can produce uncertain, or fluctuating results. Even defining the *visible* flame length, will be subject to the same problems. As an example, Kalghatgi [16] used a film speed of $1/30s$, and averaged three images to calculate the average mean length of the flame. Sugawa and Sakai ([17] 1997) measured the flame height using a video system, averaging 90 images. Cumber and Spearpoint ([12], 2006) also point out the problem of retinal retention of instantaneous flame images in averaging of rapidly fluctuating flames. Typical pulsation frequencies are approximately by the relation:

$$f = 47.4D^{-0.5} \tag{4.8}$$

where f is in Hz and D is in mm. Frequencies higher than $10Hz$ can induce retinal retention. Therefore, based on equation 4.8, jet fires with diameters of less than $23mm$, induce retinal retention that will tend to overestimate mean flame lengths based on visual observation. Also, large scale fires in the open air, can not be directly correlated to the smaller scale laboratory experimental flames. This is mainly due to the presence of wind across the direction of the jet, which have a tendency to reduce the flame length.

4.1.2 Heat flux gauge calibration

A round robin study of total heat flux gauge calibration, range $0 - 100kW/m^2$, was conducted at five fire and two calibration laboratories [18]. The aim of the study, was to find out if the different methods for calibration produced different, scattering, or systematic differences in the results. The main conclusion

was that although systematic variations between calibrations from the different laboratories were identified, the *degree of agreement was viewed as being satisfactory for most fire testing and research purposes.*

However, the studies also concluded that there was a need to develop a better understanding of the relative response of this type of gauge to radiative and conductive heat transfer. There were gauges from two manufacturers being tested, of which one, Medtherm's Schmidt-Boelter gauge, is similar to the ones used in this work, although the sensitivities of these gauges differ (round robin test: $0-100kW/m^2$, this work: $0-10kW/m^2$, $0-50kW/m^2$ and $0-300kW/m^2$). The facilities utilized by the different participating laboratories, differ substantially from each other. However, one of the participants, SINTEF, used the exact same calibration device as has been done in this work. This is the MIKRON M300. This is a spherical furnace with a small opening in it for placing the heat flux gauge. A solution for the relative response for this instrument is discussed in the paper:

If a reference total heat flux gauge with a well characterized response, i.e. low uncertainty, is available, the convective heat transfer component can be obtained by inserting the gauge flush with the furnace inner opening and measuring its response for each furnace temperature and using its known sensitivity to determine the total heat flux, E_{total}. The convective heat flux component, $E_{convective}$, is calculated as $E_{convective} = E_{total} - E_{radiative}$, where E_{total} is the measured heat flux, and $E_{radiative}$ is determined from the known black body temperature. The response of the heat flux gauge to be calibrated is also recorded for the same conditions, and its output is compared to the reference. Provided that the two heat flux meters have similar convective characteristics, the convective contribution to the heat flux can be determined for the gauge being calibrated. The uncertainty in the calibration of the reference heat flux gauge is quantified and added to the total uncertainty.

If a reference flux meter with sufficiently low uncertainty is not available, it is necessary to estimate the convective component and add this to the radiative heat flux in order to calculate E_{total} for each furnace setting. The response of the heat flux gauge to be calibrated is then measured at each level, and the appropriate amount of convective heat transfer is added to the known radiative component. The uncertainty of the convective contribution has to be quantified and added to the total uncertainty. The temperature of the cooling water representing the temperature of the heat flux gauge body is also measured in order to allow the next heat flux to the gauge to be determined [18].

For the MIKRON M300, some indications were shown for systematic lower response than the other calibration facilities, as seen in figure 4.1

Here, the SINTEF calibration is the upper line, showing that for a given heat flux, the mV signal out is slightly less than for the other gauges. This is shown as a steeper curve in table 4.1.

There were two round robin series of calibrations, and the second series yielded similar results as the first, see table 4.2. Thus it can be concluded that by using the M300 calibration setup on the Schmidt-Boelter gauges, a somewhat lower response will be produced than by using any of the other facilities.

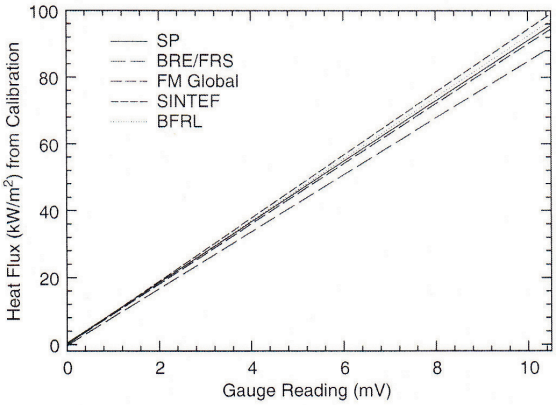

Figure 4.1: Calibration results from the five participating fire laboratories for the Schmidt-Boelter total heat flux gauge during the first round robin, -plotted as heat flux vs gauge reading (the axes in this section are opposite of what is presented in the rest of this work). Note that the SINTEF calibration, i.e the same calibration as in this work, is the upper line, showing that for a given heat flux, the mV signal out, is slightly less than for the other gauges [18]

4.1.3 Multiscale modeling

The models for combustion have normally been solved in the form of homogenous methods, sometimes multiscale. This means that a single model has been used to solve for the different turbulence scales. To account for the different physical scales, the grid has been refined e.g in volumes where there have been small turbulence scales, close to boundaries, or generally a volume that has been of particular interest to investigate in detail.

An exception from the homogenous methods, is the flow turbulence modeling, see section 3.1.5. Here, the macroscales are are represented by the integral length scale l, whereas the Kolmogorov scale

$$\eta = \left(\frac{\nu^3}{\varepsilon}\right)^{1/4} \tag{4.9}$$

may be viewed as the microscale. Here, ν is the kinematic viscosity, and ε is the mean dissipation rate. The Kolmogorov scale determines the cut-off of the self similar inertial range. Self similarity means that there exists no characteristic length scale in this intermediate range. Whether the Kolmogorov scale should be considered as a scale for microscale modeling in flow turbulence is not clear.

A general framework for developing and analyzing computational multiscale methods was proposed by Engquist [19]. It was called the Heterogeneous Multiscale Method (HMM). Peters ([20], 2009) discusses this problem. Whereas multi-grid or multi-resolution techniques may be classified as homogeneous, in

Table 4.1: Results of linear least square curve fits for calibrations for the Schmidt-Boelter gauge used in the first round robin. Note that the SINTEF curve (same calibration procedure as in this work), is forced through point (0,0) [18]

Fire Laboratory	*y-intercept*		*Slope*	
	Value	*Uncertainty*	*Value*	*Uncertainty*
SP	0.375	0.009	9.055	0.002
BRE/FRS	-0.40	0.20	8.51	0.05
FM Global	0.0	-	8.99	0.06
SINTEF	0.0	0.04	9.42	0.11
BFRL	-0.03	0.04	9.24	0.04

Table 4.2: Results of linear least square curve fits for calibrations for the Schmidt-Boelter gauge used in the second round robin. Note that the SINTEF curve (same calibration procedure as in this work), is forced through point (0,0) [18]

Fire Laboratory	*y-intercept*		*Slope*	
	Value	*Uncertainty*	*Value*	*Uncertainty*
SP	0.21	0.15	12.54	0.04
BRE/FRS	0.8	0.4	11.31	0.13
FM Global	0.0	-	12.52	0.08
SINTEF	0.0	0.04	13.8	0.3
BFRL	-0.04	0.04	12.79	0.06

the sense that they employ the same physical model on different scales, HMM uses different physical formulations at different scales and typically different numerical grids, shown in figure 4.2.

By applying different models at different scales, it is possible to model e.g a chemical system where descriptions at the atomic level can be used locally, and classical, larger scale mechanics can be used elsewhere.

Other applicable models that can be used in an HMM is the Discrete Droplet Model (DDM), used for spray calculations, soot formation models, or radiation models. HMM's require mathematically well formulated interface and boundary conditions between the macroscale and the microscale levels.

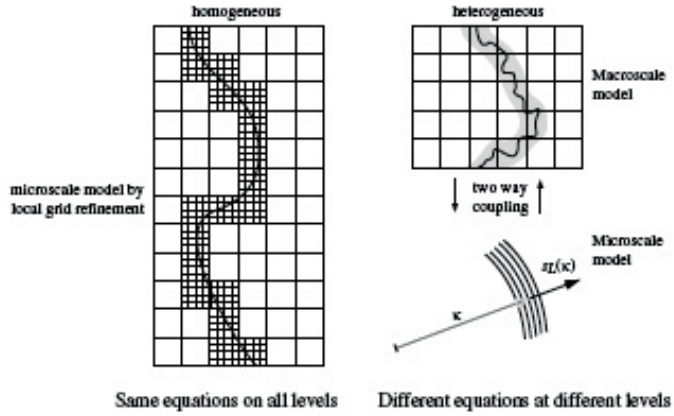

Figure 4.2: Schematic diagram showing the difference between homogenous and heterogenous multiscale methods. While homogenous multiscale methods solve the same equations using adaptive grid refinement to account for physical processes at separated scales, heterogeneous multiscale methods use different model equations with typically reduced spatial dimensions at the microscale level. The example on the right hand side is a premixed flame simulation using a curvature dependent laminar burning velocity as a microscale model, from Peters [20]

4.2 Heat transfer to cross-flow cylinder

In chapter 3, the mechanisms of heat transfer from a fluid of high temperature to a solid surface was discussed. However, as the temperature of the solid increases, there will be a reradiation and a convection from the solid back to the ambient.

Findings on emissivity and heat transfer coefficients

Mowrer ([21], 2005) discussed the ignition and flame spread characteristics of thermally thick, solid materials. Although it is not focused on ignition and flame spread in the present work, Mowrer made a general observation relevant for the heat transfer to a cross flow cylinder.

He observed that the actual thermal inertias for solids, $k\rho c$ tend to be lower by a factor of 1.3 to 2.7 when compared with reported effective values for a wide range of conditions. He pointed out that the total reradiative heat transfer coefficient, h_r varies with the third power of the absolute surface temperature. This means that there will be a non linear connection between the surface temperature and the total heat transfer coefficient, since the reradiation increases significantly with the increasing surface temperature of the solid. Translated to the situation where a temperature is measured inside a cylinder subjected to an impinging jet flame, this means that the temperature measurements can not directly yield *absolute* values for the heat transport to the cylinder. But the measured temperatures inside the cylinder will provide information of the

relative values of the heat transport.

Gardner and Ng ([22], 2006) have also taken the temperature dependence of the heat transfer coefficient for steel at different temperatures into account. In their study of temperature development in structural stainless steel sections exposed to fire, it was found that the thermal properties of stainless steel differ from those of carbon steel in a manner that favors the stainless steel. The recommended values for emissivity and convective heat transfer coefficient for stainless steel found in Euronorm EN 1991-1-2 were also investigated. This resulted in a recommendation for changing the emissivity, ϵ_m, from 0.4 to 0.2, and changing the value for convective heat transfer coefficient α_c, from 25 to $35 W/m^2K$ in the calculation model for temperature development:

$$\Delta\theta_{a,t} = k_{sh}\frac{A_m/V}{c_a\rho_a}\dot{h}_{net,d}\Delta t \tag{4.10}$$

Here $\Delta\theta_{a,t}$ is the temperature rise (^0C) in a time interval Δt (s), k_{sh} is the correction factor for the shadow effect, A_m/V is the section factor (m^{-1}), c_a is the specific heat of the material ($Jkg^{-1}K^{-1}$), ρ_a is the material density (kgm^{-3}) and $\dot{h}_{net,d}$ is the design value of the net heat flux per unit area ($Wm^{-2}K^{-1}$).

The recommended new values yielded time-temperature curves very close to measured values. It must be noted that the emissivity is dependent on the state of the steel surface. The sensitivity of the models to variation in the heat transfer coefficient and emissivity were also carried out, and two examples are given in figures 4.3 and 4.4.

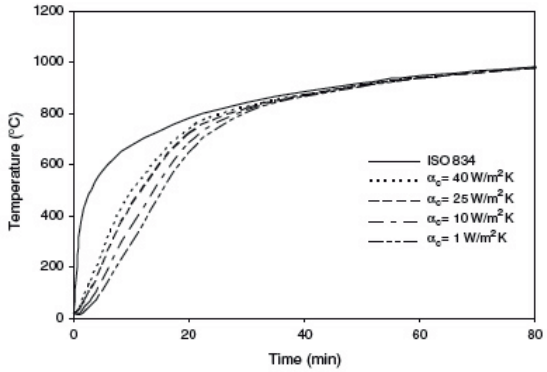

Figure 4.3: Comparison of temperature development in a steel hollow section, exposed to a standard ISO 834 temperature-Time curve, with constant emissivity, $\epsilon_m = 0.4$, and varying heat transfer coefficient. Note that for time, $t < 1min$ and $t > 30min$, there is virtually no difference in the temperatures for the different heat transfer coefficients, from Gardner/Ng [22]

From these figures, it can be seen that lower values of both heat transfer coefficient and emissivity lead to slower temperature development, and that heat transfer by convection (controlled by the heat transfer coefficient) is more

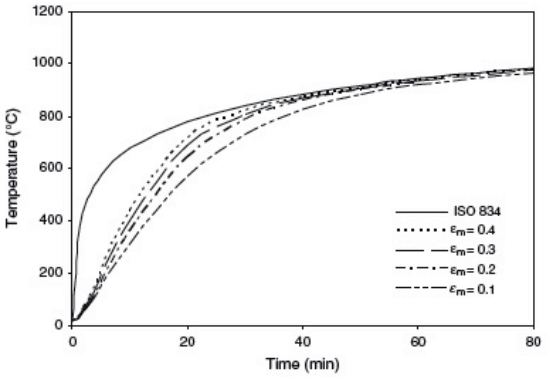

Figure 4.4: Comparison of temperature development in a steel hollow section, exposed to a standard ISO 834 temperature-Time curve, with constant heat transfer coefficient, $\alpha_c = 25W/m^2K$, and varying emissivity. Note that for time, $t < 1min$ and $t > 60min$, there is virtually no difference in the temperatures for the different emissivities. This means that the emissivity has got a greater impact on the thermal inertia than the heat transfer coefficient (see figure 4.3 above), but neither of these parameters will affect the peak temperatures to a significant extent for fires lasting more than $60min$, from Gardner/Ng [22].

significant at low temperatures, whereas heat transfer by radiation (controlled by emissivity), is dominant at higher temperatures.

This observation is discussed by Staggs and Phylaktou ([23], 2008), in their cone calorimeter tests of steel samples coated with either a low emissivity paint ($\epsilon = 0.49$) or a high emissivity paint ($\epsilon = 0.81$). Their experiments showed that the net heat flux from *convection* is dominant in the low temperature region, whereas the heat flux in the high temperature region is dominated by the *radiation*. Taking into account that $\dot{q}'' \propto T^4$, this is as expected. But it was also shown that emissivity had a low order effect on heat transfer, see figures 4.5 (both plots) and 4.6 (plot to the right).

It was also shown that the available theory for convective heat transfer coefficient for their experimental setup, which included a high temperature plate with a high temperature surface uppermost, returned values that were too low (something in the region of $10 - 15kW/m^2$). A value of $28kW/m^2$ was found more appropriate. More studies should be conducted before it is possible to tell if this too low prediction also applies for heat transfer coefficients where a steel cylinder (i.e different geometry), is impinged by a jet flame (i.e both the impingement and the gas velocities in this work are very different from the setup by Staggs and Phylaktou).

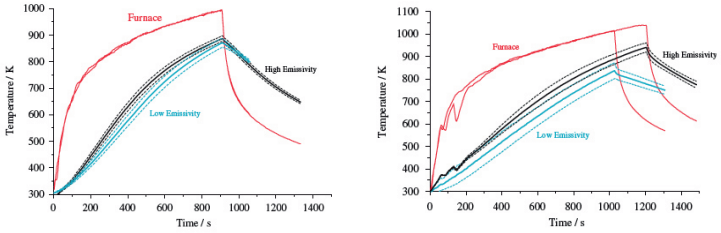

Figure 4.5: Cone calorimeter furnace tests for small beam section (left) and large beam section (right). In both experiments, it is shown that a low emissivity surface reacts slower to the increased ambient temperature than a high emissivity surface. One can also see the effect the large mass has on the rate of temperature increase. The large section in the plot to the right, has a slower temperature increase than the smaller section in the left plot, from Staggs and Phylaktou [23]

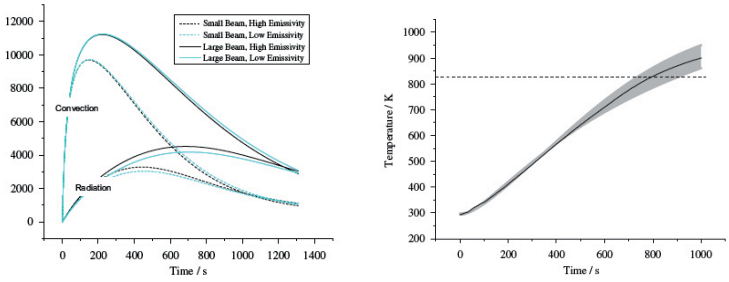

Figure 4.6: Relative convective and radiative contributions to net heat flux (left). In the early stage, when both the ambient and the section temperatures are low, the convective contribution is dominant. Later, when the temperatures are higher, the heat transfer by radiation becomes more dominant. The effects of emissivity on temperature range, is shown on the right, where the range increases with increasing temperature, from Staggs and Phylaktou [23]

Chapter 5

Experimental apparatus and procedures

5.1 Introduction

Two different projects were carried out in Part I. The first was a characterization of a propane jet flame, a joint project with Kazemi [1], [2].

The second project was a fire loading experiment. This project was carried out without cooperation from others.

5.2 Overview of main experimental setup

A rig capable of producing a propane jet flame with a discharge rate of $0.30 kg/s$, corresponding to a heat release rate, HRR, of $13-14 MW$ was built at the Res$\dot{Q}$ test site outside Haugesund. The rig consisted of a $14 m^3$ gas tank, a pump and an evaporator, see figures 5.1 and 5.2.

The available pressure without the pump was in the region $5-7 barg$. Therefore, the gas was extracted from the bottom, i.e where it was originally in liquid phase. This way, by the help of the pump and the evaporator, the rate of release could be increased beyond the natural evaporation rate at ambient conditions.

The gas was led through an outlet nozzle positioned 1500 mm above ground level. It expanded to ambient pressure via a series of visible shock waves. The physical dimensions of the nozzle are shown in figure 5.3. Steps were taken, in order to ensure that the propane was in gas phase before reaching the outlet nozzle. This included the evaporator and liquid sensors. The liquid sensors would send a signal to a valve once it detected droplets in the flow, and the valve would shut down the propane supply immediately. By careful handling of the equipment, a steady, single phase flow was obtained. The driving pressure differential across the nozzle was $10.3 barg$.

Due to problems maintaining a steady combustion during experiments, three pilot burners were installed at approximately $400 mm$ downstream of the outlet, see figure 5.1. The pilots had a separate gas supply at low pressure. This observation of a self induced blowout of the flame at high pressures caused a separate investigation to be carried out. This is the work reported in Part II of

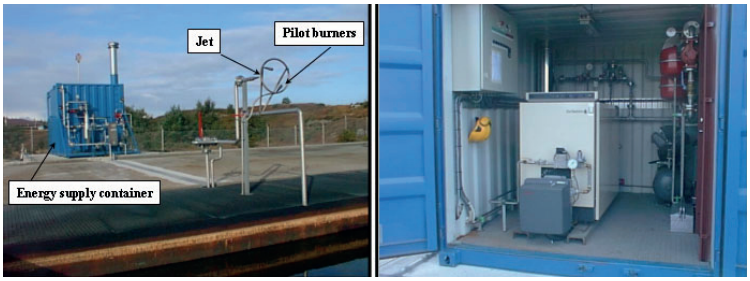

Figure 5.1: Nozzle, pilot burners and energy supply container externally, and internally, showing burner for evaporators (glycol system), compressor, control panel etc. The evaporator, mounted on the outside, was fed by heated glycol from the burner at the inside of the energy supply container. The burner system is placed on the floor of the container, and is seen on the right side image (photos: ZK/LAD)

this dissertation, resulting in a blowout model.

The above mentioned equipment was the main experimental setup used for all experiments in Part I and Part II. In addition, special equipment and arrangements were made for each individual experiment.

In the following section, additional descriptions of the setups for three different experiments are presented:

- the setup for temperature, radiation and total heat flux measurements that were carried out for the $13 - 14MW$ jet flame. This was done by using thermocouples, radiometers and total heat flux gauges
- a thick walled steel cylinder was made. Thermocouples were mounted inside the cylinder in order to measure temperatures in a section when the cylinder was put, at cross flow, into different positions in the flame
- a CFD simulation was carried out of the propane jet flame that was obtained at the test site. It was initially made before the propane rig was built. The simulation went through several revisions, before a satisfactory result was obtained. This was due to new information of the geometry of the physical setup, available pressure etc. The simulation results are from [1] and [2].

5.3 Instrumentation for jet flame experiment

The instrumentation used in this work consisted of thermocouples and heat flux meters. They are briefly discussed below.

5.3.1 Thermocouples

The terms "flame temperature" or "fire temperature" is best avoided unless it is treated with care and the use of the term is well defined. The reason is that

Figure 5.2: Exterior of energy supply container: Evaporators, liquid switches, flow- and pressure gauges, valves and pipes on the outside of the process container. The dark grey "box" to the left in the image, is the evaporator for the propane (photo: ZK/LAD)

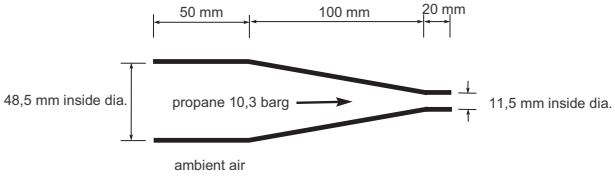

Figure 5.3: Outlet nozzle showing a typical pressure for the experiments (sketch: ZK/LAD)

a "fire temperature" only has a conventional meaning for an idealized isotropic, isothermal, hot gas and soot mixture that is optically thick at all wavelengths [4].

Hydrocarbon flames have a whole range of spatial and temporary different translational gas temperatures. There is vibrational disequilibrium in reacting regions. Soot particle temperatures may differ from those of the surrounding gas. It is not useful, and even misleading, to characterize such flames by a single temperature. In this case, thermally slow thermocouples, i.e fairly thick steel casing surrounding the electrical conductors, where used. Recordings were taken over a long time relative to the translational gas temperatures, and at many different points in the flame geometry. The latter produced temperature fields within the flame, rather than a single temperature.

Two different K-type thermocouples were used to determine the temperature, one operating at temperatures up to 1000^0C, and the other operating up to 1200^0C. The same principle applies to both types: Electrical wires of two different types are connected at the tip of the thermocouple. For K-type thermocouples, one of the wires is chromel (made of approximately 90 percent nickel and 10 percent chromium), and the other is alumel (approximately 95% nickel, 2% manganese, 2% aluminium and 1% silicon). When the wires are connected at the other end as well, a temperature difference between the two connections will cause a difference in electrical potential over the connections. At first, a mixture of water and ice was used at the "far end", in order to keep a steady temperature for the connection which was not used in the measurement zone. Now, the ice bath has been replaced with an electrical solution. In order to protect the wires from the environment within the flame, they are covered by glass fiber and metal casing. The thermocouples used were single-shield, $1.6mm$ outside diameter with $0.23mm$ conductors insulated by magnesium oxide.

The temperatures were measured at 840 separate points corresponding to 120 points in each of 7 cross sections in the flame. The grids had their center points on the jet axis, and they were positioned in x-direction as shown in figure 5.4. The available 40 thermocouples were arranged in a grid of 10 rows ($150mm$ apart) and 4 columns ($150mm$ apart), and the arrangement could easily be moved across and along the jet axis. This caused three sets of experiments to be performed for each section. Thus, a total number of 21 experiments were performed in order to cover all 840 points.

The thermocouples in each column were supported by steel angles $20 \times 20 \times 2mm$. In order to minimize disturbances of the flow, the four angles in each arrangement were oriented so that the outsides of the angles faced upstream. The thermocouple tips were placed approximately $100mm$ upstream of the steel angles in order to minimize the effect of radiation from the angles. Photographs from one of the experiments can be seen in figure 5.5.

The experiments were conducted outdoors, and the wind speed varied from $0.0 - 2.0m/s$ at angles from $45^0 - 270^0$ measured anti clockwise from a direction pointing upstream of the jet. The wind velocity was mostly in the range of $0.5 - 1.5m/s$ at approximately 150^0, see section 6.1.1 for details on how the wind conditions were treated.

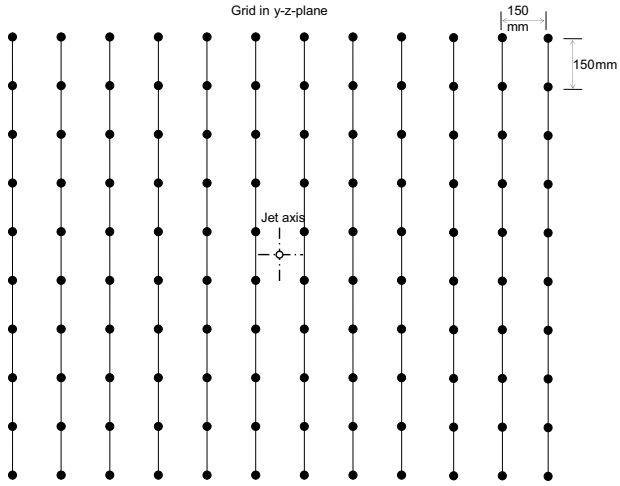

Figure 5.4: Setup for temperature measurements. The 40 available thermocouples were mounted onto 4 angle bars, shown as vertical lines here. After each experiment, the angle bars were moved to the right, in order to cover the next 40 positions. Thus, 3 experiments had to be conducted for each of the 7 sections, i.e altogether 21 experiments were carried out (sketch: ZK/LAD)

5.3.2 Heat Flux Gauges

Radiation measurements

In order to verify that the same flame was examined during the heat flux measurements as for the temperature measurements, 20 thermocouples, 1.6mm dia. K-type, were placed in four sections as shown in figure 5.6. By comparing temperatures, it was found that the conditions were the same.

Six pairs of total flux meters and radiation flux meters were mounted as shown in figure 5.7. All flux meters were placed at the same level as the jet axis, i.e at $z = 0.0m$. Four pairs were directly located in the flame zone, along the jet axis, while the other two pairs were placed outside the flame at locations $x = 3.95m$, $y = 1.50m$, and $x = 3.95m$, $y = -3.00m$. All flux meters were pointed horizontally, normal to the nozzle axis, and supported in the same manner as described for the temperature measurements earlier in this section. Each pair of flux meters were water cooled, except for F11 and F12, which were placed outside the flame. In addition, the open casing around the black body of the radiation flux meters (the view restrictor) were nitrogen purged in order to keep the sensor surfaces clean from soot and other particles.

The radiation measurements were carried out in calm conditions, with wind

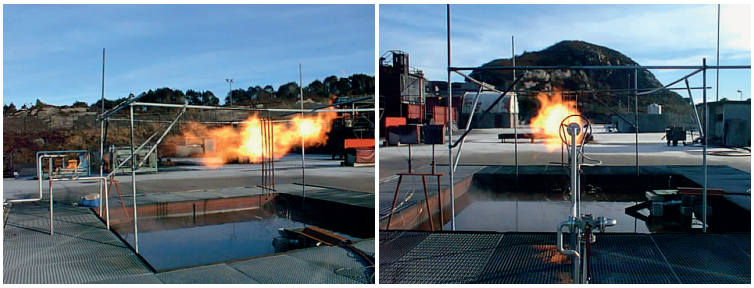

Figure 5.5: One of the 21 experiments carried out in connection with temperature measurements. The photograph to the right shows how sensitive the flow was to cross wind. The conditions were nearly calm, but the flame was still diverted slightly to the left (photos: ZK/LAD)

speeds of $0-2m/s$ at 20^0 measured anti clockwise from a vector pointing in the direction of the gas jet.

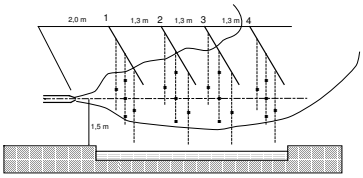

Figure 5.6: Thermocouple arrangements in radiation experiment. The purpose of using thermocouples in this part, was to confirm that the conditions were the same when measurements of radiation were conducted, compared to when the temperature measurements were carried out (sketch: ZK/LAD)

A rig was made in order to mount the devices. It is partly shown in the figures, and it consisted of steel chains hanging from steel pipes, and protected by $20 \times 20 \times 2mm$ steel angles. The thermocouples were mounted in the chain behind the angle, except for the outer $100mm$ at the tip. The part of the mounting placed in the flame, would affect the fluid flow, and possibly the readings from the thermocouples, radiometers and heat flux gauges, see section 7.1. To minimize this effect, the tip of the thermocouples were pointed upstream, parallel to the jet axis, and the heat flux gauges were oriented perpendicular to the jet axis. In addition, to minimize the error source represented by heat flux gauges, reading radiation from the mounting, the mounting was moved $100mm$ behind the gauges.

In order to distinguish between radiative and convective heat fluxes, two heat flux sensors were used. One was a radiative heat flux sensor, a radiometer, and the other was a total heat flux sensor. The readings were made in an indirect manner, by measuring a millivolt signal which was translated to a corresponding

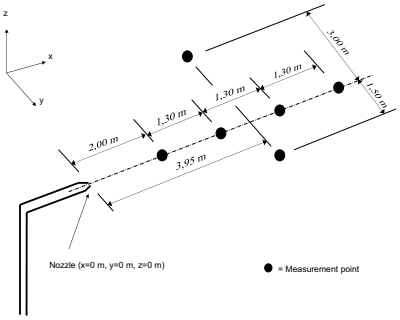

Figure 5.7: Location of heat flux measurement points, relative to the outlet. Each black dot in the sketch symbolize a radiometer/total heat flux pair (sketch: ZK/LAD)

heat flux. The radiative heat flux was read from the radiometer, whereas the convective heat flux could be found by subtracting the readings of the radiometer from the readings of the total heat flux sensor. The radiative heat flux was of main interest, since the radiometer was calibrated for reading the radiative heat flux in absolute terms. The convection part was a function of the material properties of the casing of the total heat flux sensor. A different casing would produce a different convective heat transfer to the probe, and therefore this value would only give an indication of the convective fraction. Although it was not possible to calculate the radiative fraction in the flame, a calculation of the convection from the flame to the meter could be assessed accurately. This possibility was used for the meters placed inside the flame, because the black coated sensors inside the cavities of the four radiometers were all covered with soot particles. The readings could therefore not be used for these radiometers. The values presented in figures 6.15 and 6.16 are therefore total heat flux meter readings minus the calculated convective part. See subsection 6.1.3 for further explanation on how this was treated, and subsection 7.1.3 for a discussion of the problem.

As can be seen in figure 5.8, the same principle is applied for measuring heat flux as for temperature [24]. But instead of using one pair of wires connected at both ends, a set of connections are made by winding a spiral of constantan wire around an electrically insulating wafer, then plating the turns on half of the wafer with copper. This process creates thermocouple connections at the points on both sides of the wafer where the plating ends, see figure 5.8. This way, i.e by using a differential thermopile, a complete measuring system is built into one probe. This also makes it unnecessary to provide a reference connection, unlike the thermocouples. There have been some problems with a secondary signal when the wave of heat energy reaches the connections at the back of the wafer. The two signals combine to produce a second-order response. A fast response is achieved by using a thin wafer. Recent developments claim to have solved this

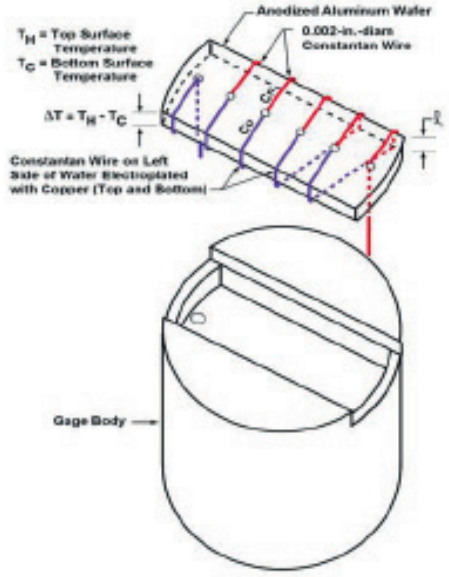

Figure 5.8: Concept of a Scmidt-Boelter heat flux transducer [24]. A set of connections are made by winding a spiral of constantan wire around an electrically insulating wafer, then plating the turns on half of the wafer with copper. This process creates thermocouple connections at the points on both sides of the wafer where the plating ends

problem.

Both the radiometers and the total heat flux transducers used were delivered by Medtherm Corporation. They had a 1" ($25mm$) casing, unthreaded. Both types were equipped with water cooling possibilities. Due to the construction, where the black coated sensor was positioned within a small cavity in the casing, the radiometer had a possibility of nitrogen purging. The purging would help soot and other particles from attaching to the surface of the sensor.

According to Medtherm Corp., the response time is less than $120ms$ for heat fluxes in the range $500 - 1000kW/m^2$, $250ms$ in the range $20 - 300kW/m^2$ and $350ms$ at $2 - 10kW/m^2$. It was also informed that the absorptance of the black coated sensors was 0.96. For the uncoated casing, this value was 0.80.

A schematic view and a photo of a total heat flux gauge is shown in figure 5.10.

The heat flux ranges for both total and radiation used in this work were $0 - 10$, $0 - 50$, and $0 - 300kW/m^2$, with a linear output signal up to $20mV$ at the design heat flux level full range. They had anyhow a capacity up to 150%

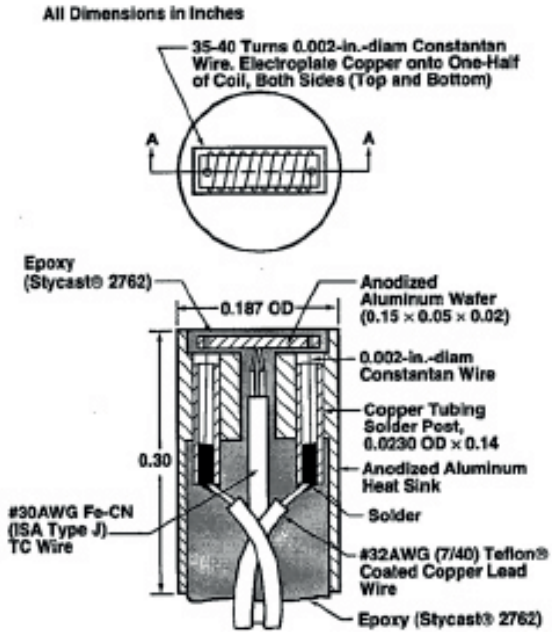

Figure 5.9: Example of section of a Scmidt-Boelter heat flux transducer [24]. This is a total heat flux transducers. The radiometers used, had a cavity within which the black coated sensor was positioned, see figure 5.11 for details

of full range.

5.3.3 Calibration of heat flux gauges

All gauges were calibrated by the manufacturer before delivery, and the calibrations are traceable to the National Institute of Standards and Technology, NIST.

To ensure reliable readings in the experiments, all gauges exposed to the high temperature zones, needed to be calibrated frequently. Detailed description of the calibration works can be found in [1].

A Micron M300, similar to the one used by SINTEF, was used in this work, see subsection 4.1.2. By kind permission from Kazemi, the results from the calibrations are shown in subsection 6.1.1. A detailed description of the applied calibration equipment and procedures can be found in Kazemi´s dissertation [1].

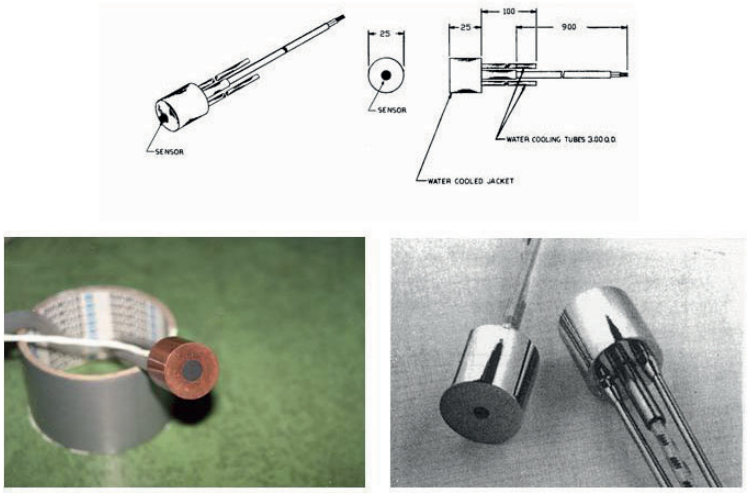

Figure 5.10: Physical specification and image of a heat flux transducer. Additional shielding was necessary when putting the sensors into the flame. In this work, the sensor cables and water hoses were put into an insulating material (Rockwool), before it was put into a steel pipe. The steel pipe was then covered by a pipe insulating material (sketch and right photo: Medtherm manual, left photo: ZK/LAD)

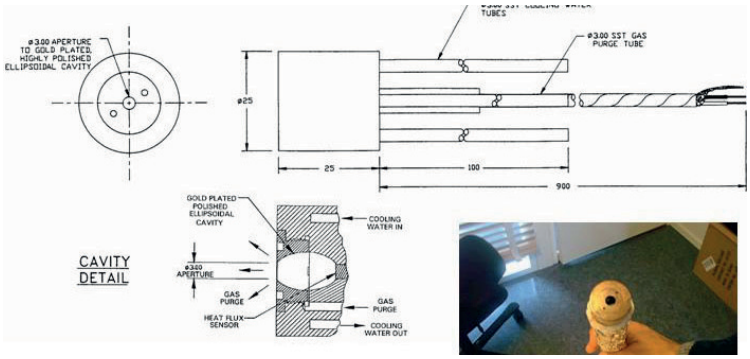

Figure 5.11: Physical specification and image of an ellipsoidal radiometer. Additional protection was necessary, and it was done in the same manner as for the heat flux transducers, see figure 5.10 above (sketch: Medtherm manual, photo: ZK)

5.4 Instrumentation for heat transfer measurements

After a thorough description of the turbulent jet flame arising from the release of $\approx 0.3 kg/s$ of propane from an $11 mm\ dia$ nozzle had been carried out, it was

of interest to find out more about the thermal loading inflicted upon a steel unit impinged by this kind of flame.

In order to do so, a hollow $160mm$ outer, and $73mm$ inner diameter, AISI 316, stainless steel cylinder was made, see figures 5.12 and 5.13. Due to the low cylinder to nozzle diameter ratio (= 14.5) it was of particular interest to find out *where* around the cylinder's circumference the highest thermal loading would be. Since the two diameters differed by an order of only 1, it was hard to predict the consequences of the flow interacting with the cylinder.

5.4.1 Test cylinder

Since the area exposed to the highest thermal loads also would have the highest temperature, 12 thermocouples, type K, were placed into the steel cylinder, see the red/green indications in figure 5.13. The eight thermocouples nearest the cylinder's external surface, were numbered from 1 to 8, and the four thermocouples nearest the cylinder's inner surface were numbered from 9-12, in accordance with table 5.1, below:

Table 5.1: Positions of thermocouples in steel cylinder, see the red/green circles in figure 5.13 for more details

Thermocouple no.	*Position*	
	outer circle	*inner circle*
1	top	
2	top/rear	
3	rear	
4	bottom/rear	
5	bottom	
6	front/bottom	
7	front	
8	top/front	
9		top
10		rear
11		bottom
12		front

A supply was connected, causing a cooling water flow through the inside of the cylinder. The purpose was to achieve a state of heat transfer radially through the cylinder as near as possible to being steady. Also, it was to prevent over heating of the steel. Measures were taken, so that the hollow section of the cylinder always was completely water filled, but at a low water pressure, to prevent water from getting in contact with the thermocouples. In addition, where the compensation cables connected to the thermocouples were lead out through a hole in the pipe, a seal was applied.

5.4.2 Measurements

Six experiments were carried out. All measurements were made in a vertical plane along the axis of the jet. During the first three experiments, the horizontal distances between the nozzle and the cylinder were appoximately $3.0m$ (see table 5.2). The cylinder was originally placed underneath the trajectory of the centre of the jet, before it was moved upwards to the level of the trajectory, and then

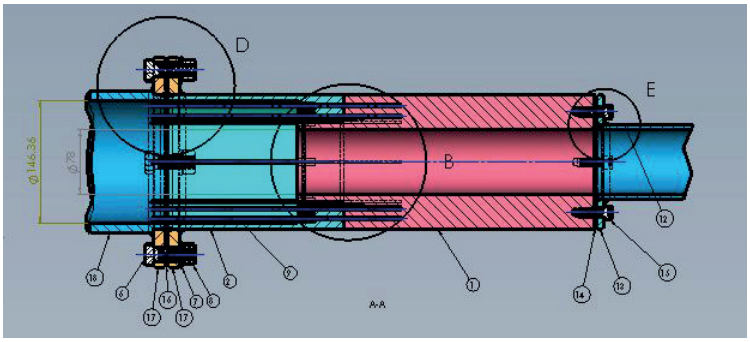

Figure 5.12: Longitudinal section of test cylinder. The tip of the thermocouples were placed inside the pink coloured part at the right hand end of the blue lines that indicate the drilled holes for the thermocouples. See key dimensions in figure 5.13 below (sketch: Steinsvik Maskinindustri AS)

Table 5.2: Setup for heat transfer to cross flow cylinder, where x-value denotes the horizontal distance from the nozzle outlet to the centre of the cylinder, and y-value denotes the corresponding vertical distance. From the table, it can be seen that the cylinder was placed at two different horizontal distances away from the outlet. For each of these two distances, one position was below, one was at, and one was above the jet axis

Exp. no.	$x(m)$	$y(m)$	*flow* kg/s)	P (bar)	*Air temp.*(^0C)
1	2.95	-0.35	0.30	9.2	5
2	3.03	-0.04	0.30	10.5	6
3	3.05	0.40	0.30	10.4	6
4	5.40	-0.51	0.30	10.2	7
5	5.39	0.10	0.29	10.0	6
6	5.40	0.48	0.30	10.0	2

at a higher level. The same procedure was repeated at a distance approximately $x = 5.40m$ from the cylinder. However, in these three experiments, the vertical distances were larger. The reason was that the jet had expanded more here than at $x = 3.0m$, and it was necessary to ensure that measurements were made both below, at, and above the centre line of the trajectory. This also meant that, in experiment 5, the centre of the flame would be a distance approximately $y = 0.10m$ above the nozzle. This was due to the decrease in flow velocity, thus a corresponding relative increase in buoyant forces which gave a lifted trajectory.

The experiments were carried out outdoors, in calm conditions. The wind speed never exceeded $3.0m/s$, and the transverse component of the wind, relative to the jet, never exceeded $2.0m/s$.

Due to the danger of damaging the test cylinder, it was considered sufficient to stop the experiments immediately after the log showed a curve where $\frac{\delta T}{\delta t} \approx 0$,

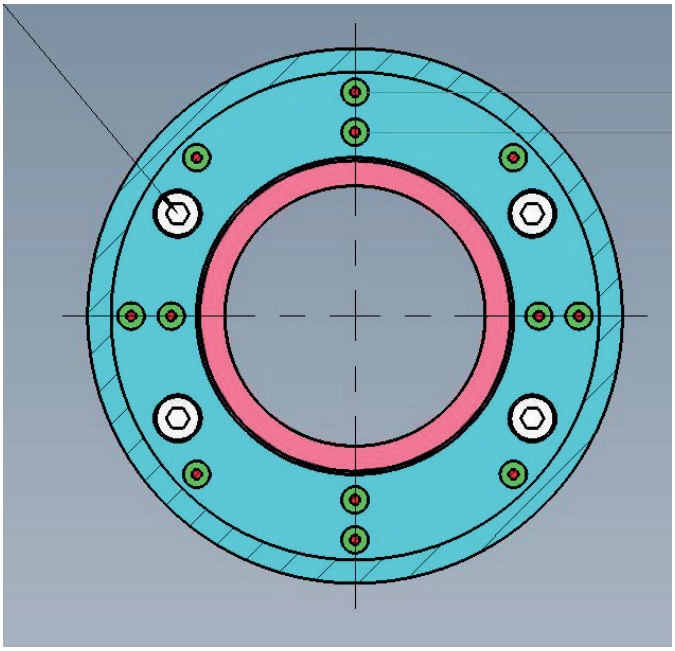

Figure 5.13: Cross section of test cylinder. The red/green circles indicate the positions of the thermocouples. The white circles show positions of bolts needed to connect the flanged part with the part without a flange, see figure 5.12. Key dimensions: cylinder diameter, $D = 160mm$, distance from centre of outer 8 thermocouples to outer surface of cylinder= $11mm$, distance from centre of inner 4 thermocouples to outer surface of cylinder= $23mm$ The reason why these dimensions are not shown on the drawings, is that they were made by Steinsvik Maskinindustri AS. Solid Edge was used, and this software has not been available for the author (sketch: Steinsvik Maskinindustri AS)

normally after $8 - 10min$. The experiments were carried out over a too short time span to get a confirmed steady state. But the shape of the Temperature-time curves indicated close to steady state conditions. Two trial runs were performed before any measurements were done, and the cylinder was cleaned after each trial and experiment. This way, the emissivity of the steel surface was kept close to constant.

5.5 CFD modeling

The experiments carried out for the temperatures and radiation were discussed with, and modeled by Kazemi [1], [2] using computational fluid dynamics, CFD. By obtaining consistency between experimental results and the CFD modeling,

one could, with a fair degree of confidence, use the model to obtain results for the flow velocities within the flame. It would not have been possible to measure this parameter with the available equipment in the experiments.

5.5.1 Kameleon FireEx in general

KFX is a simulator which consists of several parts:

- the pre-processor. It is called Lizard, and is used for defining the geometry to be simulated. In combination with a graphical user interface, the geometry can be inspected in 3D. The boundary conditions are put into the pre-processor and a number of parameters used to decide how the calculations shall be run (time steps, which equation solvers to use etc)

- the CFD code. The solver uses a finite volume technique, similar to finite element techniques used for solids, to solve the averaged basic transport equations for three dimensional cases. By using time steps, transient solutions are calculated. The model calculates velocity components in all axis directions, enthalpy, species mass fractions and soot mass fractions. It uses a k - ε model to simulate turbulent flow, and also uses the Eddy Dissipation Concept, EDC, developed by prof. Bjørn Magnussen for combustion. It can be used both for fast and slow- as well as reversible and irreversible reactions. The package also includes calculation of radiation [25]

- the post-processor. This collects the calculated data and can present the results in various ways, including the graphical user interface Kfxview [26]

5.5.2 The simulation

The simulation was run by Kazemi [1].

In order to determine where to put the instrumentation for the experiments, a number of CFD simulations were run to get an indication of the size and shape of the jet flame. Trials were then carried out using the actual rig without instrumentation. The trials showed that the simulation gave rough indications of the actual conditions.

Once the gas rig was available for experiments, an iterative simulation process was carried out. By careful adjustments of grid refinement, time steps, nozzle geometry, boundary conditions etc, Kazemi, in cooperation with Vembe at ComputIT, reached what was found to be the best obtainable simulation. A summary of input is presented below:

- geometry dimension: $13 \times 7 \times 9m$ ($L \times W \times H$)

- grid resolution: $63 \times 55 \times 60$ (207,900 grid nodes). Resolution unevenly distributed, smaller cells around discharge point, larger cells further away, see figure 5.14 for more information

- boundaries: floor at bottom, i.e isothermal solid cells mainly covered with a solid isothermal core as domain cells, shaped as a pool, as for the experimental setup. Other boundaries were defined as wind boundary cells

- nozzle position: at pt $(x, y, z) = (0, 0, 0)$, $2m$ above the floor
- time steps: $10\mu s$
- flow rate of propane, pressure, temperature, nozzle geometry, type of thermocouple: as used in experiments
- wind velocity: $0.0m/s$ (slightly different from the experiment, where moderate wind of $< 2.0m/s$ varied in speed and direction)
- calculated parameters: temperature, radiative heat flux, gas velocity. Positions of calculated points were the same as for the experiments

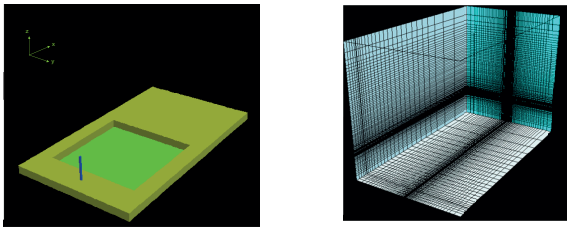

Figure 5.14: Setup of simulation model. Outlet was placed at the top of blue line in the left figure. Grid resolution, shown at right, was $63 \times 55 \times 60$*, equivalent to 207,900 grid nodes. The calculation domain size was* $13 \times 7 \times 9m(L \times W \times H)$*. Transient time step was set to* $10\mu s$ *(KFX printouts: ZK)*

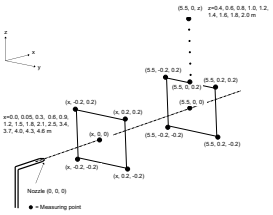

Figure 5.15: Location of gas velocity measurement points. 15 planes perpendicular to the jet axis were measured as shown in the plane nearest the outlet nozzle, and an additional plane was measured at the far end, as shown to the right in the figure (sketch: ZK/LAD)

Chapter 6

Results

6.1 Characterization of experimental jet flame

In order to compare the results from the experiments with the simulation in a best possible way, all results are put side by side at the end of this section.

6.1.1 Temperature measurements and simulations

Although the conditions were near calm when the experiments were conducted, the gas jet reacted to even the smallest flow of ambient air, and the effect increased with the distance from the nozzle. 21 experiments were conducted outdoors over a period of time. This resulted in slightly different conditions between, and even within each experiment. Adjustments for these effects have been made, in order to describe the flame as it would appear in no wind, in accordance with the following assumptions:

It was assumed that for still air, the temperature fields in the flame would have been near symmetric about the x-z-plane containing the jet axis, where the x-value denotes the horizontal distance from the nozzle, and the z-axis is vertical. Due to gravitational and buoyancy effects, it was assumed to be nonsymmetric temperature fields about the x-y-plane. Similarly, due to the expanding flow field of the gas downstream, the temperature fields also were assumed to be nonsymmetric about the z-y-plane.

Thus, a horizontal correction of the experimentally obtained temperature fields in the y-direction was performed in order to reduce the effect of wind. This was done by plotting y-values vs temperatures, see figure. 6.1 below:

It can easily be seen that it was not possible to make the temperature plots exactly symmetrical about any vertical line in the figure. But by integrating the temperature with respect to y, a corrected position for $y = 0$ (giving new $z - axis$) will be the line which cuts the area under the curve in half. The effect of this correction can be seen in figure 6.2. The new $z - axis$ was placed at the nearest column of actually measured temperatures. This means that it was possible to place the corrected $z - axis$ up to $75mm$ off from the axis defined as the correct. However, a check was run, indicating an offset of the axis in the range $1 - 28mm$. It can be argued that by using absolute temperatures rather than ^0C, the correction would be more conservative. This was checked, and it was found that it had no influence on the choice of $z - axis$.

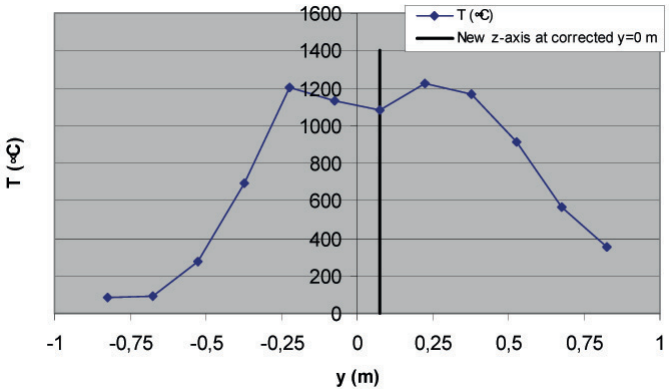

Figure 6.1: Temperatures across the flame at $x = 2.5m$, and at $z = 0.0m$. The vertical (z-) axis has been moved 100mm to the right, in order to adjust for horizontal deviation of the flame due to cross wind. The area under the curve to the left of the new z-axis is equal to the similar area to the right of the axis, in accordance with the symmetry assumption stated in this section

Note that the plot is the same, except for positioning of the vertical axis. Thus, corrections have been made for a wind from the right in the example shown in figure 6.2. Similar corrections were made for all seven sections shown in figures 6.5 - 6.11. Figures 6.12 and 6.13 show the longitudinal temperature profile for the whole range of measurement area in experiment and simulation, respectively.

As indicated in figure 6.4, the field measurements and simulations compared fairly well, except for the effect of buoyancy forces on the flame tip. The results revealed that the end of the flame (approximately 20%) was more affected by buoyancy forces in simulations compared with the experiments, see figure 6.4. In other words it seemed like the jet velocity dropped too quickly in the simulations. An attempt to overcome this effect was made by increasing the jet velocity. This was done by applying other calculation models for jet outlet conditions available in KFX [1].

The CFD simulation, but not the MatLab plots, was run by Kazemi [1].

Figures 6.4, 6.6 - 6.11, 6.12 and 6.13 combined, and the plots of the instantaneous temperatures following these figures, all show that the simulated temperatures compared well with the experimental values. No difference in maximum temperatures could be observed, but the temperature fields were slightly smaller for the simulations.

Still, a distinct difference between the experimental and the simulated results could be observed. Smooth temperature fields were produced in the apparently steady ("steady turbulent") flame present in the simulations. This was not the case for the experiments. They showed fluctuating ("unsteady turbulent") temperature fields for the real flame.

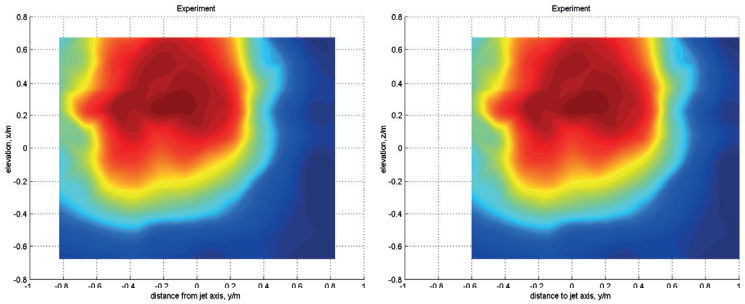

Figure 6.2: Temperatures at $x = 3.7m$ from nozzle, original observations at the left of the figure, corrections for wind effects at the right, as explained in figure 6.1

This could partly be explained by the fact that in the simulations, the wind effects were ignored (set to zero) and the effects of steel angles in the flame (used to support the thermocouples in experiments) and the surrounding objects (buildings, equipment etc.) were neglected. Figure 6.4 demonstrates this difference:

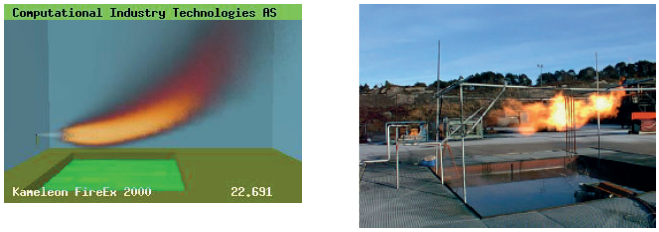

Figure 6.4: Comparison of simulation and experiment. The smooth result in the simulation was partly due to no wind, no experimental equipment placed within the flame and no surrounding objects. The buoyancy at the end of the flame was more dominant in the simulation than in the experiment. No apparent reason for this was found (KFX printout: ZK, photo: ZK/LAD)

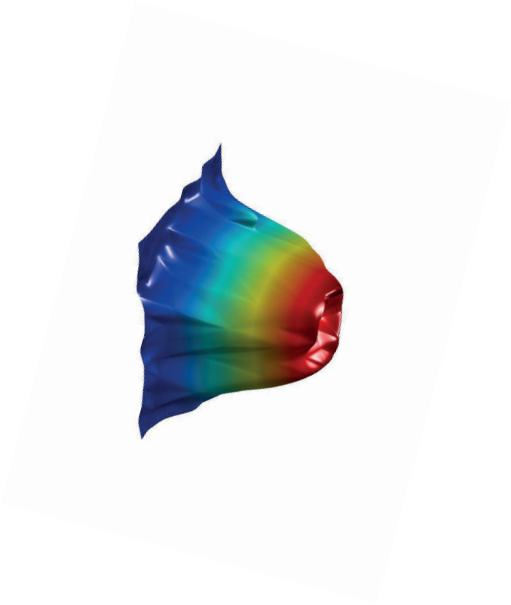

Figure 6.3: 3D impression of temperatures in the vertical plane at x=2.5m; data collected from experiment. Note that max. temperatures are found at a distance away from the trajectory of the jet centre. The same information is found in the 2D plot in fig 6.5, and the same colour code is used in the plots

Time averaged plots

Time averaged temperatures in planes perpendicular to the jet axis are shown below. The numbers at the axes denote distance (m) from the jet axis. The colours indicate temperatures in accordance with the colourbar in figure 6.5. The same colour code was used for all plots.

Experimental plots are found to the left, and plots from simulation to the right in the figures. The simulations were carried out using Kameleon FireEx [1], [2]. The plots were made using MatLab.

The plots clearly show the less symmetric temperature fields in the experimental flame compared to the simulated flame. This feature becomes even more evident in the instantaneous plots following the longitudinal plots in figure 6.13:

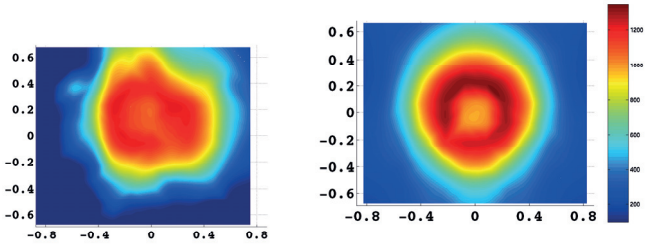

Figure 6.5: Temperatures at $x = 2.5m$ from nozzle - see comments at top

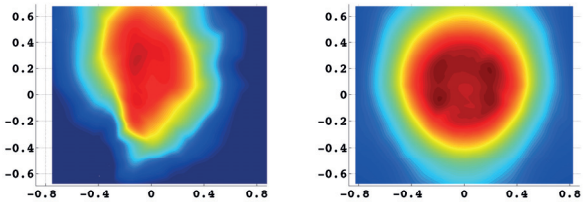

Figure 6.6: Temperatures at $x = 3.4m$ from nozzle - see comments at top

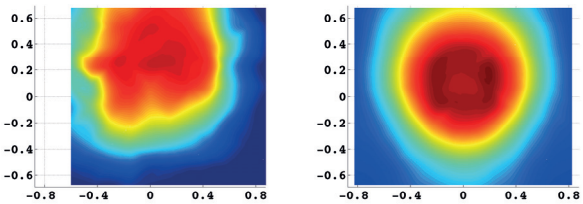

Figure 6.7: Temperatures at $x = 3.7m$ from nozzle - see comments at top

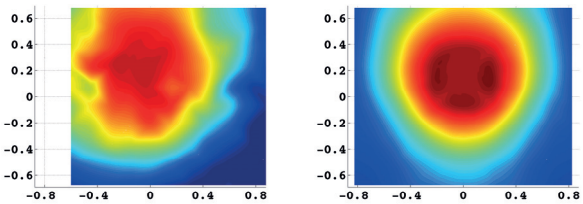

Figure 6.8: Temperatures at $x = 4.0m$ from nozzle - see comments at top

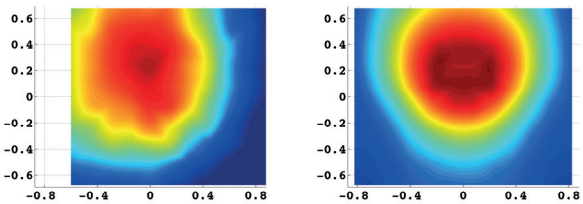

Figure 6.9: Temperatures at $x = 4.3m$ from nozzle - see comments at top

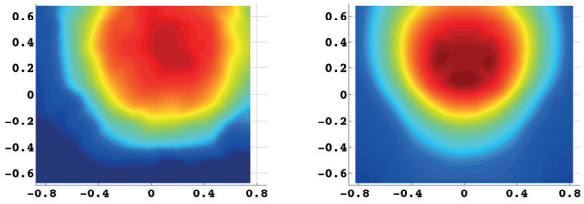

Figure 6.10: Temperatures at $x = 4.6m$ from nozzle - see comments at top

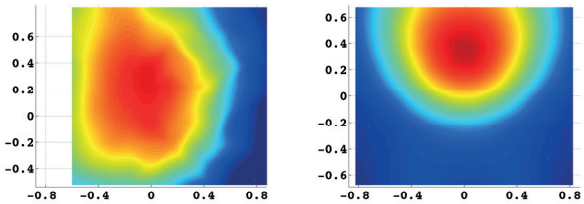

Figure 6.11: Temperatures at $x = 5.5m$ from nozzle - see comments at top

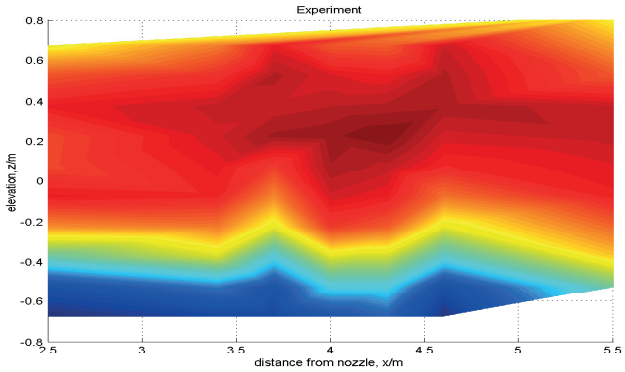

Figure 6.12: Longitudinal temperature plot along jet axis, experiment. This plot, together with the plot in figure 6.13, show the same feature as the transverse plots above, in terms of lack of symmetry for the experiment, and smooth, symmetric temperature fields for the simulated flame

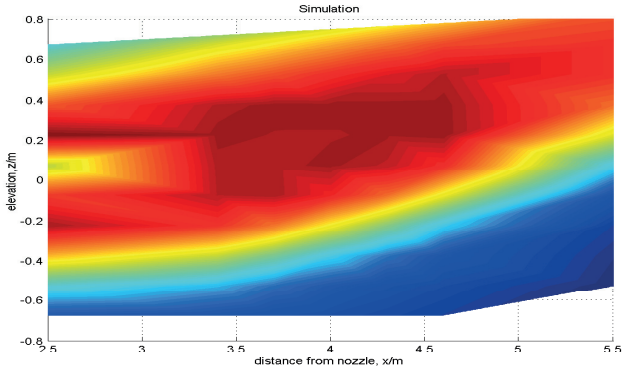

Figure 6.13: Longitudinal temperature plot along jet axis, kameleon. This plot, together with the plot in figure 6.12, show the same feature as the transverse plots above, in terms of lack of symmetry for the experiment, and smooth, symmetric temperature fields for the simulated flame

Instantaneous plots

Instantaneous temperatures across the flame are shown below. The distance from the nozzle is $x = 4.0m$. For the experiment (left column), the time range is from 32 to 60s, and for simulation (right column), from 5 to 13s. The numbers denote distance (m) from jet axis, the colours indicate temperatures in accordance with the colourbar in figure 6.5. The same colour code was used for all plots. These plots clearly show the less symmetric temperature fields in the experimental flame compared to the simulated flame:

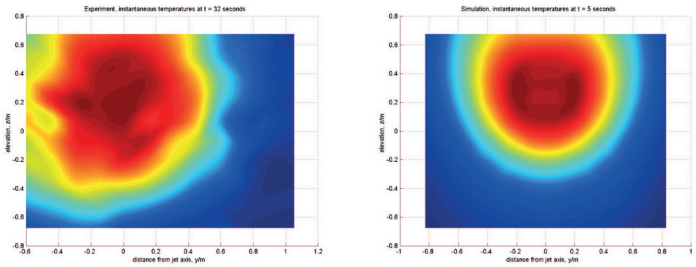

32 seconds/5 seconds - see comments at top

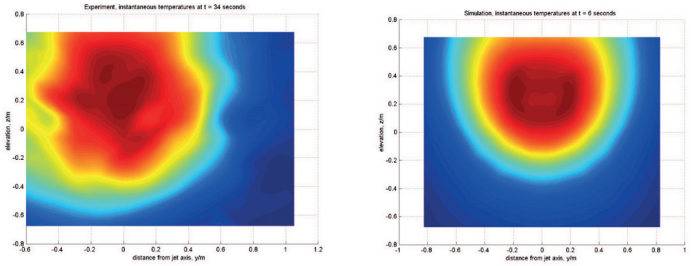

34 seconds/6 seconds - see comments at top

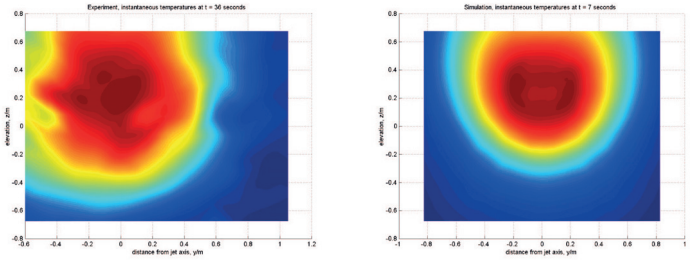

36 seconds/7 seconds - see comments at top

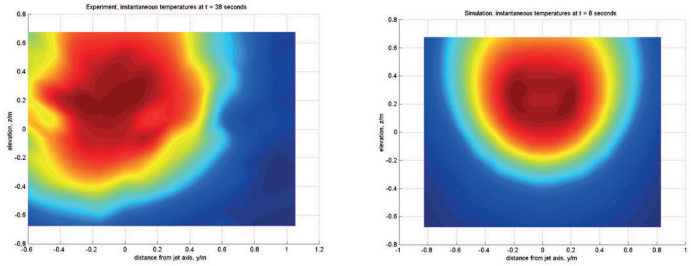

38 seconds/8 seconds - see comments at top

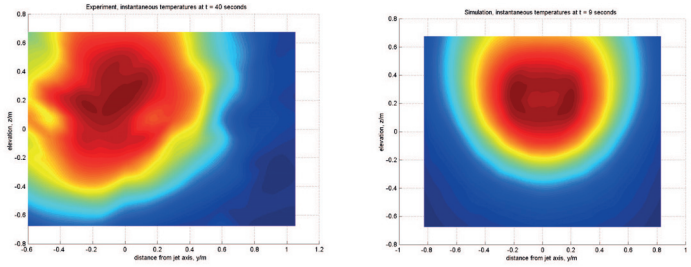

40 seconds/9 seconds - see comments at top

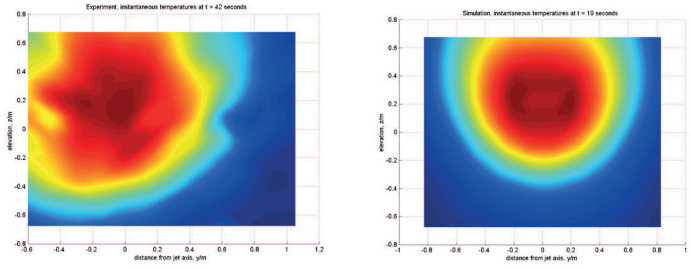

42 seconds/10 seconds - see comments at top

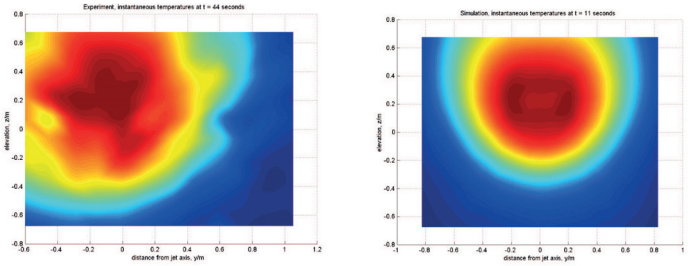

44 seconds/11 seconds - see comments at top

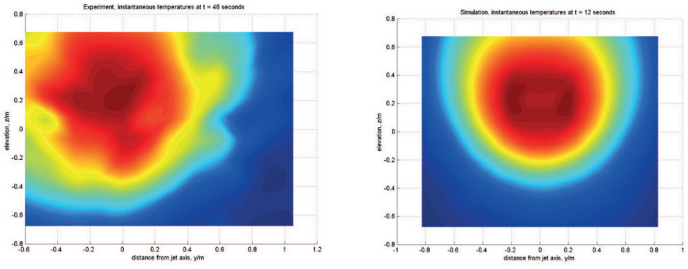

46 seconds/12 seconds - see comments at top

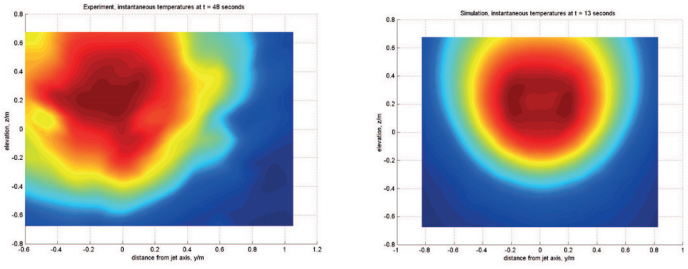

48 seconds/13 seconds - see comments at top

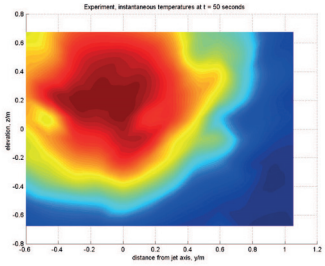

50 seconds - see comments at top

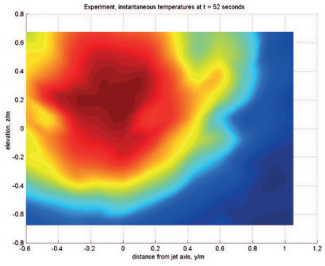

52 seconds - see comments at top

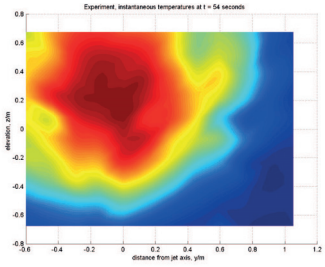

54 seconds - see comments at top

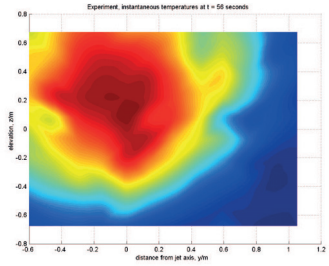

56 seconds - see comments at top

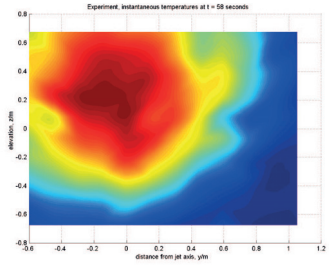

58 seconds - see comments at top

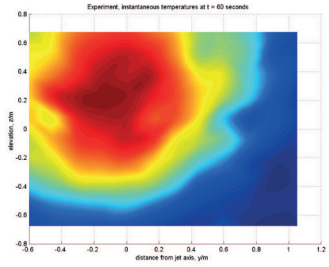

60 seconds - see comments at top

6.1.2 Radiation measurements and simulations

Heat flux plots

During the experiments, total heat flux meters and radiometers were placed at the same level as the nozzle, according to the setup described in figure 5.7. The same positions applied for the virtual instruments used in Kameleon. This means that the plots in figures 6.16 - 6.19, all represent a horizontal surface at the level of the outlet of the jet.

Measured radiant heat flux

Due to problems with soot formation at the black coated sensors on the 4 radiometers placed along the axis of the jet outlet, the plot of the measured radiant heat flux shows the readings from the accompanying 4 total heat flux meters, with a calculated convective part deducted. One pair of meters were also placed on each side of the jet trajectory, as shown in figure 5.7. Radiometer readings from the 2 meters placed outside the flame, were used for the plot. See figure 6.16 for the results. The colour code used, is the same for all plots in figures 6.16 - 6.19.

From the left plot in figure 6.15, it can be seen that, except for the meter placed $2m$ from the outlet, the measured values were $\approx 30kW/m^2$ higher than the calculated inside the flame. Some of the explanation for this, but not all, can be due to the M300 calibration setup, see section 4.1.2. Also, the total heat flux meters that were put inside the flame, changed their emissivity during the experiments. This can be seen by comparing the photographs of the sensors before and after experiment, see figure 6.14.

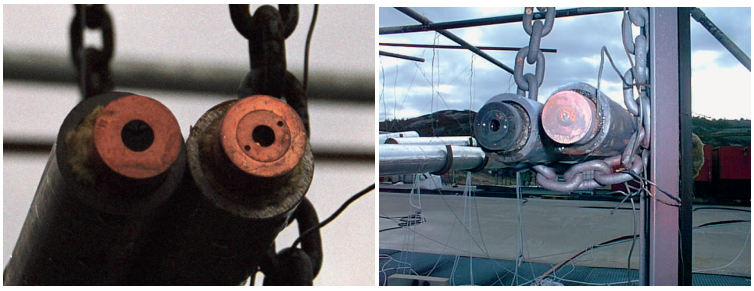

Figure 6.14: Physical condition of heat flux sensors before (left) and after (right) experiment (photos: ZK/LAD)

Simulated radiant heat flux

These plots show the simulated readings from 6 virtual radiometers, placed at the exact same positions as the meters in the experiment, as shown in figure 5.7. See figure 6.17 for the results.

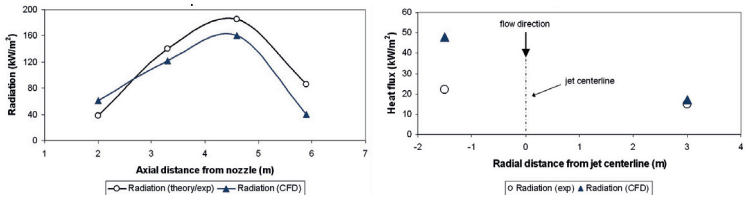

Figure 6.15: Measured and calculated heat fluxes along the jet trajectory (left figure), and at two positions on the outside of the flame (right figure). It can be seen that the CFD simulation follows the measured values (plots: ZK)

Measured total heat flux

This plot shows the actual readings from 6 total heat flux meters, placed pairwise together with the radiometers, as shown in figure 5.7. See figure 6.19 for the results.

6.1.3 Treatment of data from heat flux measurements

The readings from the 4 radiometers placed inside the flame were not used, due to soot formation at the black sensors on these meters. Therefore, the convective part of the total heat flux meters were calculated, and the value was deducted from the total heat flux reading in order to obtain the radiation at this point. The calculation is from [1]:

$$h = 0.033 \frac{\rho C_p \nu^{0.2} u^{0.8}}{d_g^{0.2}} \tag{6.1}$$

where

$$\begin{aligned} \rho &= \text{gas density (kg/m}^3\text{)} \\ C_p &= \text{specific heat capacity of gas (kJ/kgK)} \\ \nu &= \text{kinematic viscosity of gas (m}^2\text{/s)} \\ u &= \text{gas velocity (m/s)} \\ d_g &= \text{outside diameter of heat flux gage (m)} \end{aligned}$$

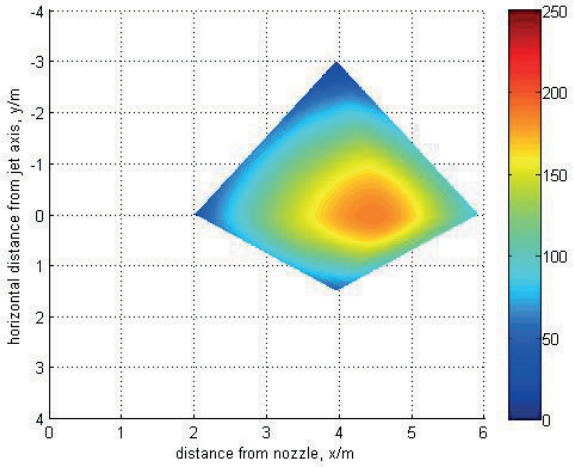

Figure 6.16: Measured radiant heat flux (kW/m^2), looking down at a surface, level with the outlet. Outlet is placed at point (0,0), i.e to the left, middle of the diagram. Note that the values were not directly measured, due to soot formation at the black coated sensor of the radiometers. Therefore, the convective heat transport to the total heat flux sensor had to be calculated, and subtracted from the total heat flux reading, in order to find the radiation at that point. Maximum measured heat flux was $185kW/m^2$

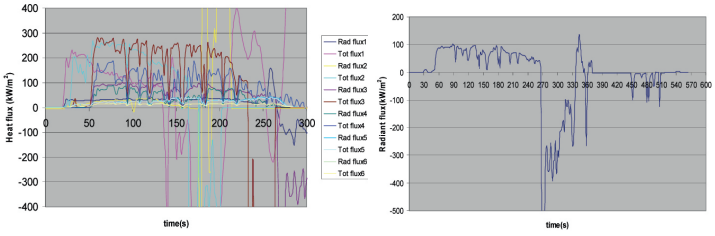

(a) (b)

Figure 6.18: Heat flux plots for (a) all flux meters, and (b) radiant heat flux observations for RF3 (meaning radiometer no.3, used as an example in this figure). The large variations in heat fluxes that can be seen in both these plots, were due to closure of valves and partly meltdown of equipment, as explained in the main text below. Note that the radiometer readings were not used, due to soot formation at the black sensors on these meters. Therefore, the convective part of the total heat flux meters were calculated, and the value was deducted from the total heat flux reading in order to obtain the radiation at this point

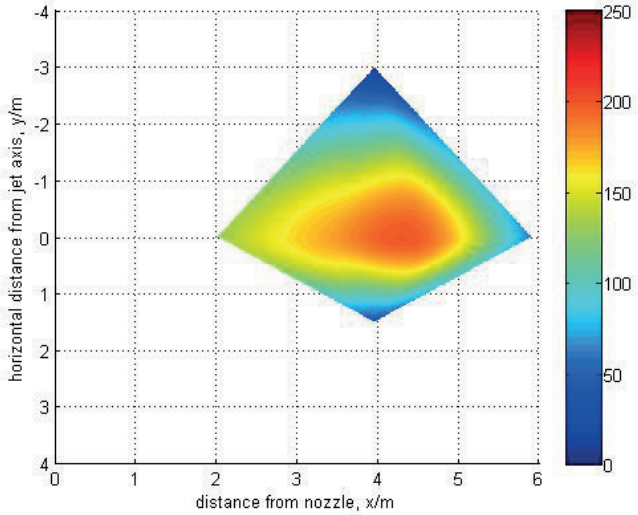

Figure 6.17: Simulated radiant heat flux (kW/m^2), looking down at a surface, level with the outlet. Outlet is placed at point (0,0), i.e to the left, middle of the diagram. Maximum simulated heat flux was $193kW/m^2$ *(simulation: ZK, plot: LAD)*

The velocity, u, in the equation was not measured, but the values for the velocities from simulations were used for these meter positions. Then, by applying Newton´s law of cooling, $\dot{Q}^{"} = h(T_2 - T_1)$, the convective cooling was assessed, and the radiation was found by deducting the convection from the total heat transfer reading. Here, T_2 is the measured gas temperature in the flame, T_1 is the temperature of the total heat flux meter casing, approximated by the ambient temperature.

The logging of measurements started before the meters were exposed to the jet flame. The recordings from $t = 0s$ to a few seconds after the meters were exposed to the flame, were therefore not used in the final plots. It was chosen to treat all readings within the same time span. Also, after 2-3 minutes, the framework that held the meters in place, and even some of the meters themselves, started to melt. The meltdown of the meters was caused by an insufficient water supply due to lack of insulation at a spot along the water supply. Therefore, none of the results outside the time span 60-120 seconds could be used to produce reliable plots, see figure 6.18.

Also, there were incidents that occurred during the time span 60-120 seconds that required the collected data to be filtered. Due to a large flow, the evaporator was not able to function fully throughout the experiment. This caused some of the propane to pass through the evaporator in liquid phase, which in turn caused a liquid switch to close a valve and stop the flow. The closure of the

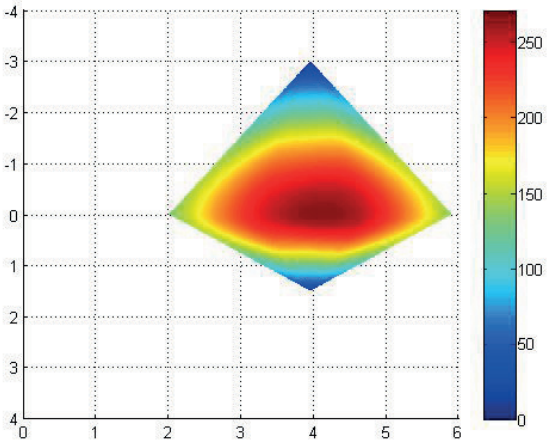

Figure 6.19: Measured total heat flux (kW/m^2), looking down at a surface, level with the outlet. Outlet is placed at point (0,0), i.e to the left, middle of the diagram. The maximum measured value was $256kW/m^2$

valve was recorded manually. The manual record was compared to the sudden changes in radiation that can easily be seen in figure 6.18(b). The two were found to appear at the same time, and a procedure was applied to avoid using the recorded radiation during the closure of the valve. The best curve fit, related to the manually recorded valve closure, was achieved by applying the following stepwise procedure:

1) all changes of radiation of more than $10kW/m^2$ in any 2 second period were erased
2) the average value of the remaining recordings were calculated for each meter
3) any value lying outside one standard deviation from the average, was erased
4) the new average value was calculated and reported

6.1.4 Calibration Results

By kind permission from Kazemi [1], the results from the calibrations are shown in figures 6.20 - 6.23. For comparison, the manufacturer´s calibrations, marked Medtherm, were also plotted. Note that figures 6.21 and 6.22 refer to two different pairs of gauges. A detailed description of the applied calibration equipment and procedures can be found in Kazemi´s dissertation [1].

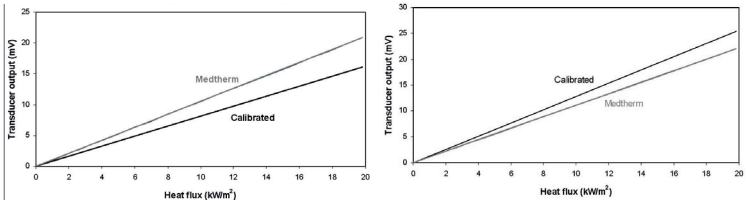

Figure 6.20: Calibrated radiant and total heat flux gauge with range $0-10kW/m^2$ *Deviations from manufacturer´s calibrations are shown. Note that the new calibration shows that the radiometer is less sensitive, and the total heat flux gauge is more sensitive, compared to the original calibration (plots: ZK)*

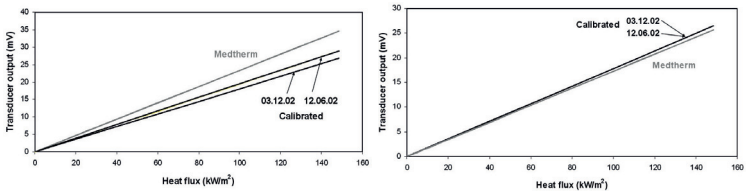

Figure 6.21: Calibrated radiant and total heat flux gauge with range $0 - 50kW/m^2$. *Here, the new calibration shows that the gauges has become less sensitive after being used in the experiments, especially the radiometer(plots: ZK)*

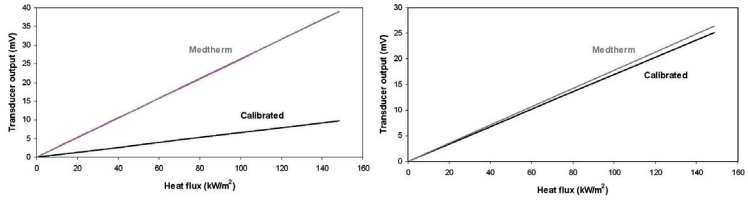

Figure 6.22: Calibrated radiant and total heat flux gauge with range $0 - 50kW/m^2$. *Here, the new calibration shows that the gauges have become less sensitive after being used in the experiments, especially the radiometer (plots: ZK)*

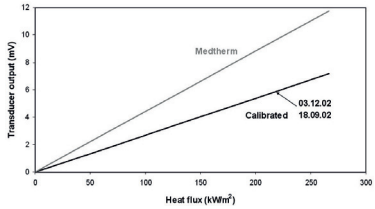

Figure 6.23: Calibrated radiant and total heat flux gauge with range $0 - 300kW/m^2$*. The new calibration shows that the radiometer has become less sensitive after being used in the experiments (plot: ZK)*

6.1.5 Gas velocity simulation

The gas velocity was calculated along the centre line of the flow, see figure 6.24 below [1]. Here, the distance from the outlet of the gas is plotted along the x-axis. The gas velocity in the centre of the flow field, can be read from the left hand y-axis. The vertical distance between the nozzle and the centre line of the flow, can be read at the right hand y-axis.

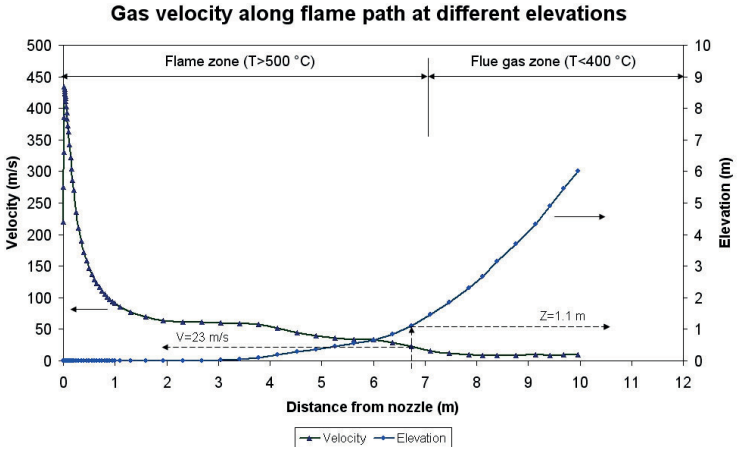

Figure 6.24: Calculated gas velocity along centre line of jet flame path. Distance from the outlet of the gas is plotted along the x-axis. The gas velocity in the centre of the flow field, can be read from the left hand y-axis. The vertical distance between the nozzle and the centre line of the flow, can be read at the right hand y-axis. In the example given in this figure, the flow velocity at a horizontal distance of $6.7m$ *in the centre of the flow, is* $23m/s$*. The vertical position of the flow centre at this distance, is* $1.1m$ *(KFX printout: ZK)*

6.2 Measurements of heat transfer

A cylinder placed inside the flame was equipped with 12 thermocouples as shown in figure 5.13. Detailed temperature readings from the 8 thermocouples in the outer circle, combined with interpolated values for each 5^0 radial line, are presented in subsections 6.2.1 - 6.2.6 for the six experiments. An overview is presented in figure 6.49, also showing the experimental setup.

For each of the six experiments, the first Temperature-time plots have been made for thermocouples 1, 3, 5 and 7, representing the top, rear, bottom and front thermocouples in the outer circle respectively, see figure 5.13. The second plots in each experiment show the three thermocouples that were placed in the area of the largest heat transfer. The same axis format and colour coding has been used in all plots, in order to ease the reading. A more graphical view is then presented, where the temperatures have been plotted radially around the cylinder. Finally, two photographs are shown from each experiment.

The experiments showed that

- the heat transfer in all cases were from the front/bottom to the top of the cylinder, i.e at the side facing the nozzle
- for experiments 2 and 5, where the position of the cylinder was at the trajectory of the jet, the maximum heat transfer was in the front section of the cylinder
- for experiments 3 and 6, where the position of the cylinder was above the trajectory of the jet, the maximum heat transfer was in the front, lower section of the cylinder
- for experiment 4, where the position of the cylinder was below the trajectory of the jet, the maximum heat transfer was in the front, upper section of the cylinder
- for experiment 1, where the position of the cylinder was below the trajectory of the jet, the maximum heat transfer was in the top section of the cylinder, i.e this experiment was the only one breaking a pattern where the thermocouple nearest the outlet nozzle had the highest temperature. However, the thermocouple nearest the nozzle, had a temperature that was 5^0 less than the maximum
- in experiments 1-3, where the cylinder was placed at a horizontal distance of $3.0m$ away from the nozzle, the heat transfer was larger than for the corresponding positions in experiments 4-6, where the cylinder was placed at a horizontal distance of $5.4m$ away from the nozzle

6.2.1 Experiment 1

The plot below gives an overview of the Temperature-time curves for thermocouples placed at top/rear/bottom/front. The cylinder was positioned at $2.95m$ horizontal distance and $-0.35m$ vertical distance from the outlet.

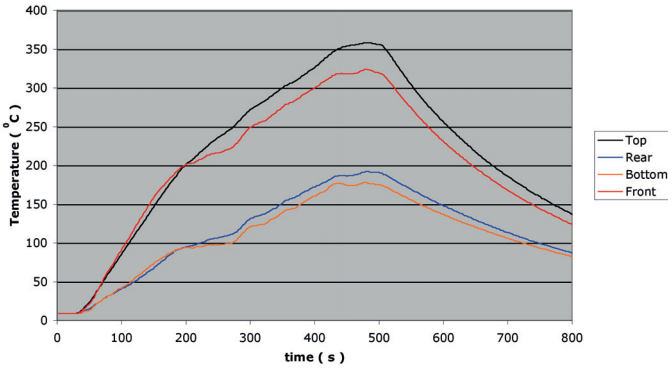

Figure 6.25: Experiment 1 - overview

In the next plot, Temperature-time curves are shown for the three thermocouples that were placed in the area of the largest heat transfer.

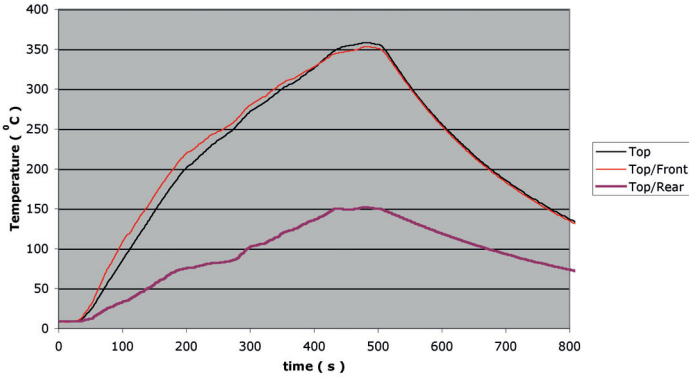

Figure 6.26: Experiment 1 - details

Due to the position of the cylinder relative to the flame, it can be seen that the stagnation point is within a 90^0 sector of the largest rate of heat transfer. This result is similar for all experiments.

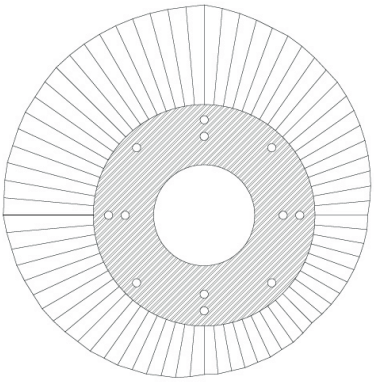

Figure 6.27: Experiment 1 - temperatures around the cylinder. The length of the radial lines are proportional to the thermocouple temperature in the cylinder, measured in ^0C. Maximum temperature in this experiment, where the cylinder was placed below the jet trajectory, was 358^0C in Th1, i.e at top

Two images from the experiment, showing the experimental setup, and indicating the flame geometry. Note that the flame fluctuations were large, and these images are not representative for the entire experiment.

Figure 6.28: Experiment 1 images. Note that photo of flame is an instantaneous image, and may not be representative for the long term thermal load inflicted on the cylinder

6.2.2 Experiment 2

The plot below gives an overview of the Temperature-time curves for thermocouples placed at top/rear/bottom/front. The cylinder was positioned at $3.03m$ horizontal distance and $-0.04m$ vertical distance from the outlet.

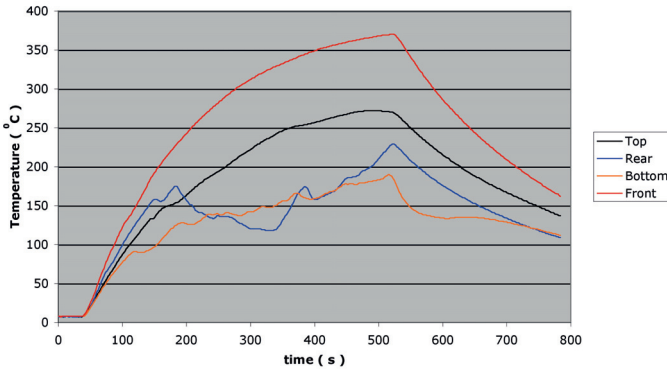

Figure 6.29: Experiment 2 - overview

In the next plot, Temperature-time curves are shown for the three thermocouples that were placed in the area of the largest heat transfer.

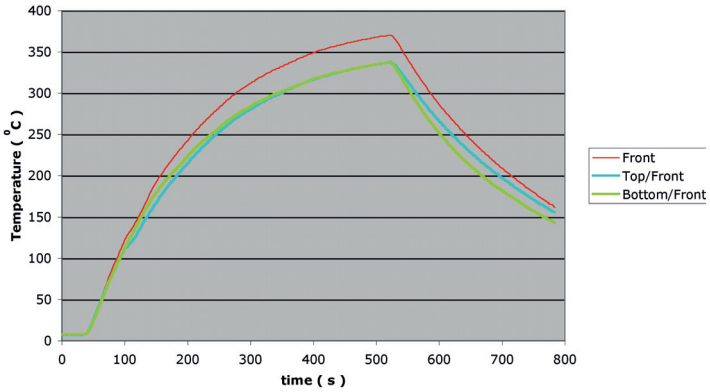

Figure 6.30: Experiment 2 - details showing the three thermocouples that were placed in the area of the largest heat transfer

Due to the position of the cylinder relative to the flame, it can be seen that the stagnation point is within a 90^0 sector of the largest rate of heat transfer. This result is similar for all experiments.

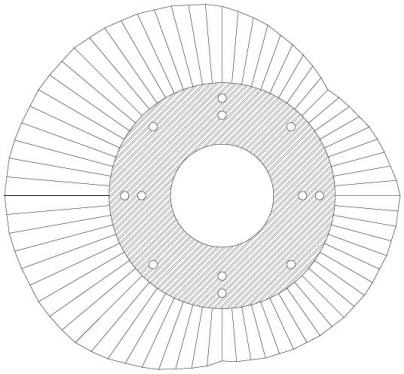

Figure 6.31: Experiment 2 - temperatures around the cylinder. The length of the radial lines are proportional to the thermocouple temperature in the cylinder, measured in ^0C. Maximum temperature in this experiment, where the cylinder was placed at level with the jet trajectory, was 370^0C in Th7, i.e at front

Two images from the experiment, showing the experimental setup, and indicating the flame geometry. Note that the flame fluctuations were large, and these images are not representative for the entire experiment.

Figure 6.32: Experiment 2 images. Note that photos of flame are instantaneous images, and may not be representative for the long term thermal load inflicted on the cylinder

6.2.3 Experiment 3

The plot below gives an overview of the Temperature-time curves for thermocouples placed at top/rear/bottom/front. The cylinder was positioned at $3.05m$ horizontal distance and $0.40m$ vertical distance from the outlet.

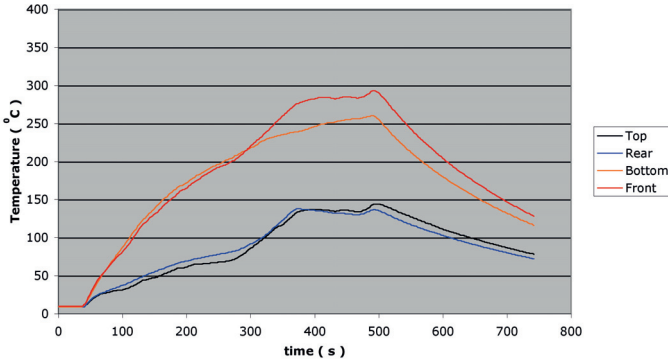

Figure 6.33: Experiment 3 - overview

In the next plot, Temperature-time curves are shown for the three thermocouples that were placed in the area of the largest heat transfer.

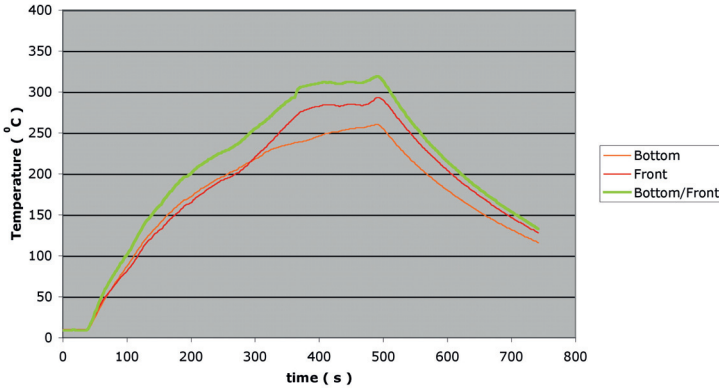

Figure 6.34: Experiment 3 - details showing the three thermocouples that were placed in the area of the largest heat transfer

Due to the position of the cylinder relative to the flame, it can be seen that the stagnation point is within a 90^0 sector of the largest rate of heat transfer. This result is similar for all experiments.

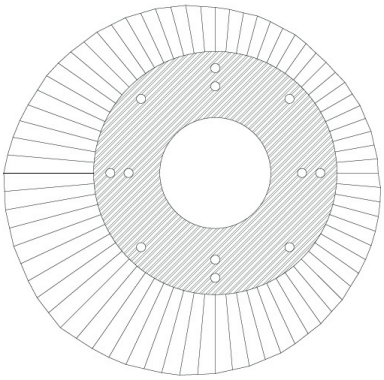

Figure 6.35: Experiment 3 - temperatures around the cylinder. The length of the radial lines are proportional to the thermocouple temperature in the cylinder, measured in ^0C. Maximum temperature in this experiment, where the cylinder was placed above the jet trajectory, was 319^0C in Th6, i.e at front/bottom

Two images from the experiment, showing the experimental setup, and indicating the flame geometry. Note that the flame fluctuations were large, and these images are not representative for the entire experiment.

Figure 6.36: Experiment 3 images. Note that photos of flame are instantaneous images, and may not be representative for the long term thermal load inflicted on the cylinder

6.2.4 Experiment 4

The plot below gives an overview of the Temperature-time curves for thermocouples placed at top/rear/bottom/front. The cylinder was positioned at $5.40m$ horizontal distance and $-0.51m$ vertical distance from the outlet.

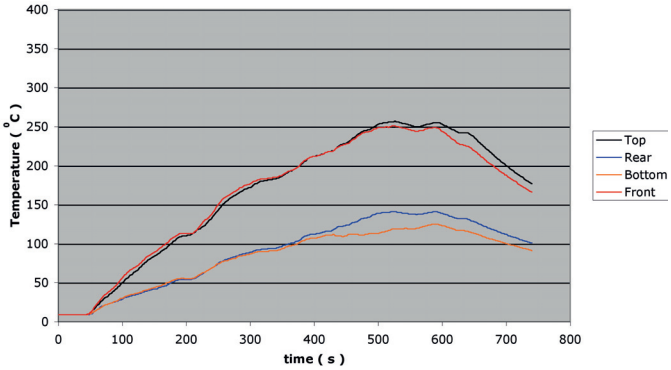

Figure 6.37: Experiment 4 - overview

In the next plot, Temperature-time curves are shown for the three thermocouples that were placed in the area of the largest heat transfer.

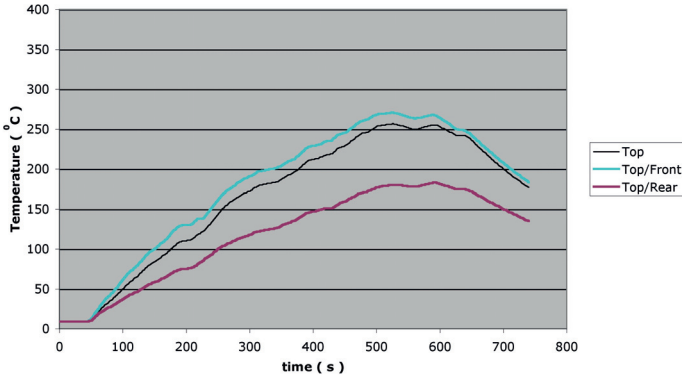

Figure 6.38: Experiment 4 - details showing the three thermocouples that were placed in the area of the largest heat transfer

Due to the position of the cylinder relative to the flame, it can be seen that the stagnation point is within a 90^0 sector of the largest rate of heat transfer. This result is similar for all experiments.

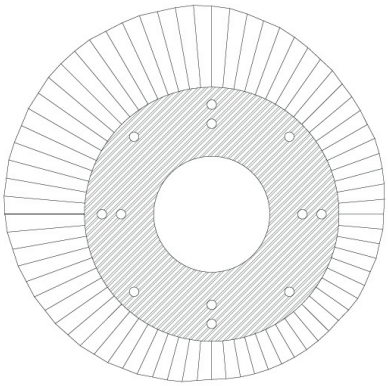

Figure 6.39: Experiment 4 - temperatures around the cylinder. The length of the radial lines are proportional to the thermocouple temperature in the cylinder, measured in ^0C. Maximum temperature in this experiment, where the cylinder was placed below the jet trajectory, was 271^0C in Th8, i.e at front/top

Two images from the experiment, showing the experimental setup, and indicating the flame geometry. Note that the flame fluctuations were large, and these images are not representative for the entire experiment.

Figure 6.40: Experiment 4 images. Note that photos of flame are instantaneous images, and may not be representative for the long term thermal load inflicted on the cylinder

6.2.5 Experiment 5

The plot below gives an overview of the Temperature-time curves for thermocouples placed at top/rear/bottom/front. The cylinder was positioned at $5.39m$ horizontal distance and $-0.10m$ vertical distance from the outlet.

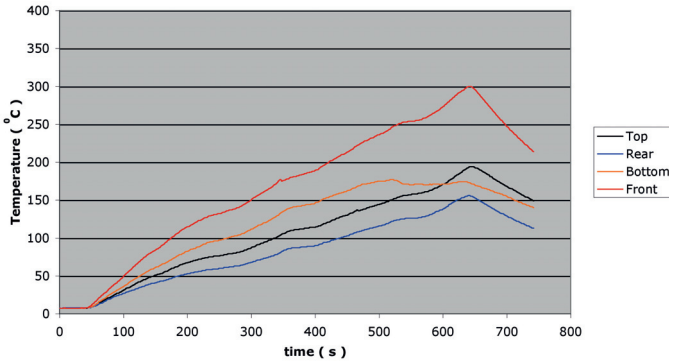

Figure 6.41: Experiment 5 - overview

In the next plot, Temperature-time curves are shown for the three thermocouples that were placed in the area of the largest heat transfer.

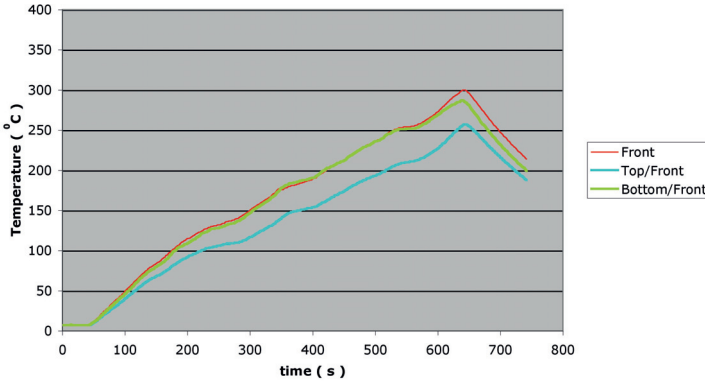

Figure 6.42: Experiment 5 - details showing the three thermocouples that were placed in the area of the largest heat transfer

Due to the position of the cylinder relative to the flame, it can be seen that the stagnation point is within a 90^0 sector of the largest rate of heat transfer. This result is similar for all experiments.

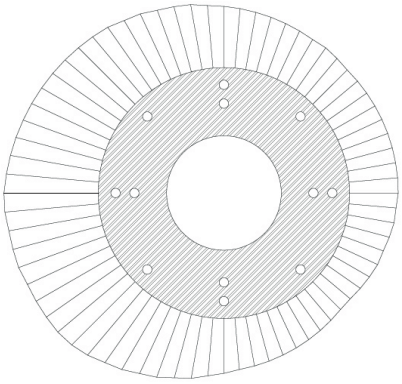

Figure 6.43: Experiment 5 - temperatures around the cylinder. The length of the radial lines are proportional to the thermocouple temperature in the cylinder, measured in ^0C. Maximum temperature in this experiment, where the cylinder was placed at level with the jet trajectory, was 300^0C in Th7, i.e at front

Two images from the experiment, showing the experimental setup, and indicating the flame geometry. Note that the flame fluctuations were large, and these images are not representative for the entire experiment.

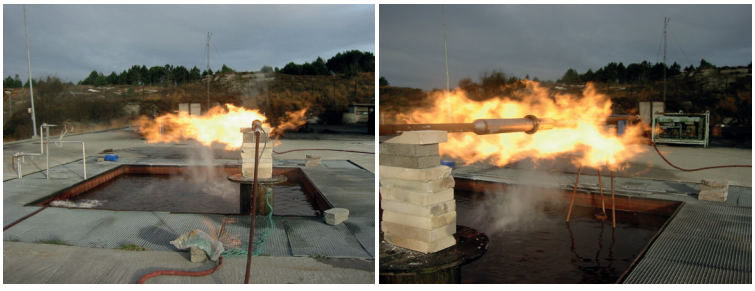

Figure 6.44: Experiment 5 images. Note that photos of flame are instantaneous images, and may not be representative for the long term thermal load inflicted on the cylinder

6.2.6 Experiment 6

The plot below gives an overview of the Temperature-time curves for thermocouples placed at top/rear/bottom/front. The cylinder was positioned at $5.40m$ horizontal distance and $0.48m$ vertical distance from the outlet.

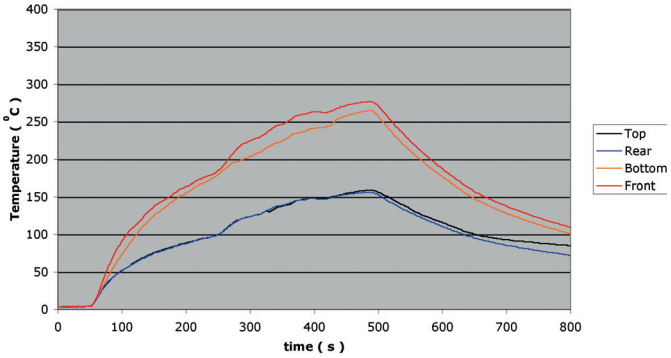

Figure 6.45: Experiment 6 - plot showing Temperature-time curves for thermocouples placed at top/rear/bottom/front. Cylinder position: $5.40m$ *horizontal distance and* $0.48m$ *vertical distance from the outlet*

In the next plot, Temperature-time curves are shown for the three thermocouples that were placed in the area of the largest heat transfer.

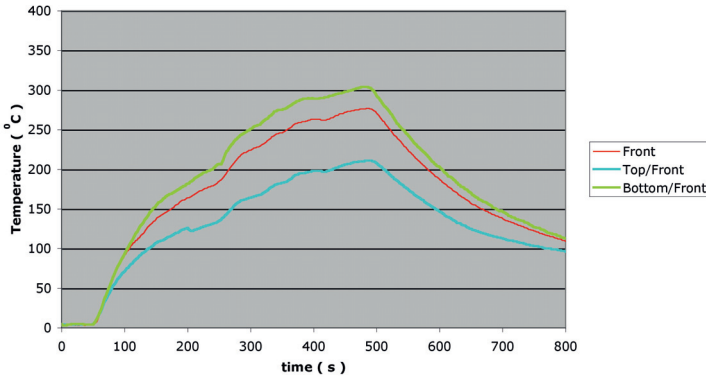

Figure 6.46: Experiment 6 - details showing the three thermocouples that were placed in the area of the largest heat transfer

Due to the position of the cylinder relative to the flame, it can be seen that the stagnation point is within a 90^0 sector of the largest rate of heat transfer. This result is similar for all experiments.

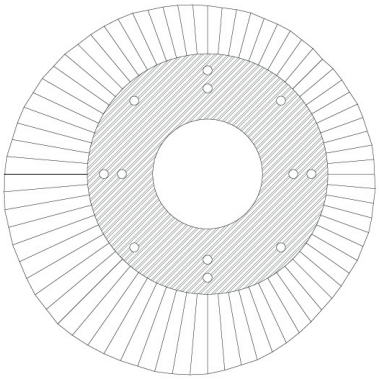

Figure 6.47: Experiment 6 - temperatures around the cylinder. The length of the radial lines are proportional to the thermocouple temperature in the cylinder, measured in ^0C. Maximum temperature in this experiment, where the cylinder was placed above the jet trajectory, was 304^0C in Th6, i.e at front/bottom

Two images from the experiment, showing the experimental setup, and indicating the flame geometry. Note that the flame fluctuations were large, and these images are not representative for the entire experiment.

Figure 6.48: Experiment 6 images. Note that photos of flame are instantaneous images, and may not be representative for the long term thermal load inflicted on the cylinder

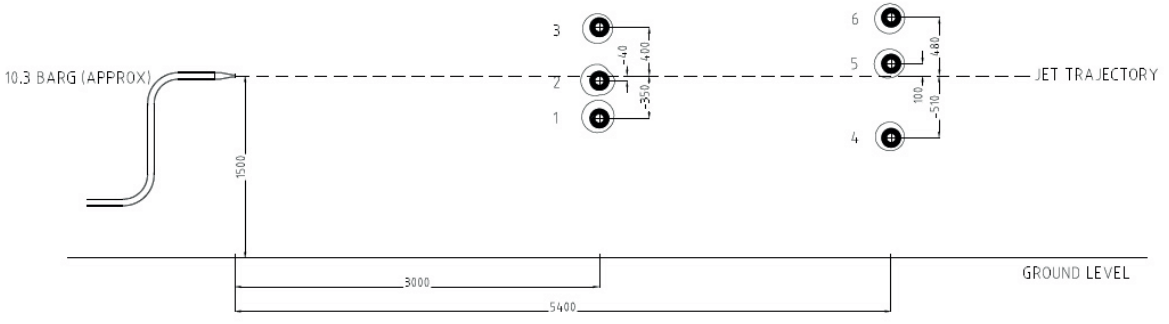

Figure 6.49: Setup and results overview of temperature distributions. The irregular shaped "balloons" surrounding the cylinder, are the temperature readings. The further away from the cylinder the balloon is, the higher the thermocouple reading. Note that for both experiments where the cylinder was placed above the jet trajectory (exp.3 and 6), the highest temperature was found at thermocouple 6, i.e the one facing front/down. For both experiments where the cylinder was placed at the jet trajectory (exp.2 and 5), the highest temperature was found at thermocouple 7, i.e the one facing front. For one of the experiments where the cylinder was placed below the jet trajectory (exp.4), the highest temperature was found at thermocouple 8, i.e the one facing front/up. The only exception from this pattern, was experiment 1. Here, the highest temperature was found at thermocouple 1, i.e at top. If the pattern had been followed, thermocouple 8 would be expected to have the highest reading in this experiment. The difference between thermocouples 1 and 8, however, was only 5^0C. The numbering of the thermocouples are shown in table 5.2 and figure 5.13

Chapter 7

Discussion

7.1 Characterization of experimental jet flame

7.1.1 General

The temperatures predicted by calculations agreed well with those of the measurements as shown in figures 6.5 to 6.11. Due to a slightly higher influence of buoyancy, one would expect the CFD flame to be lifted up accordingly at the end of the flame. This can be seen in the figures.

Another feature which distinguished these two flames was the lift-off distance. The CFD flame had a slightly shorter lift-off than the experimental flame. A closer investigation showed that the CFD model was based on the chemical properties of methane, which is a likely reason for predicting a shorter length [1].

Although the CFD flame diameter might look smaller than the experimental flame diameter, it could be justified by the fact that the transport equations are solved based on the mean values, and the ambient conditions are chosen as neutral (e.g no wind). Apart from this, the flame lengths in both cases agreed satisfactory.

7.1.2 Temperature difference treatment in Kameleon

The temperature difference between the metal junction inside the thermocouple and the actual gas temperature was calculated by Kameleon. But the model works in the opposite direction of what an experiment would do, by first calculating a gas temperature. By using heat balance equations, in principle like equation 7.1, a theoretical thermocouple reading was calculated. It was not possible to get the source code or a theory manual that could state the exact model that is used in Kameleon, and which assumptions that are made. However, there are only small deviations between experiments and simulations.

7.1.3 Errors in temperature and radiation measurements

Temperature measurements

Using thermocouples to measure high temperatures is a well established method. When two dissimilar metal wires are connected at one end, a potential voltage

difference develops across the open ends if the temperatures are different between the junction and the open ends. Thus by keeping the open ends at a known temperature, the temperature at the junction can be assessed with a great deal of accuracy by relating the measured potential voltage difference to the temperature.

The residence time of thermocouples in the flame in each of the 21 experiments was in the range $78-98s$, with $4-5$ minutes pause between experiments. The thermocouples were placed in a rough environment during the experiments. Therefore, prior to performing experiments, each individual thermocouple was tested by lifting its temperature from ambient to around 500^0C by using a hand held propane burner. One purpose of the test was to reveal any mechanical failures, like a shortcut of the wires somewhere along the thermocouple rather than at the tip. The other purpose was to discover a possible physical damage at the tip.

The type of thermocouples used, are designed for temperatures not higher than approximately 800^0C This was realized after the work was done. For high temperature applications, e.g. inside a flame, particularly for long residence times, the thermocouples of type R (PtRh-Pt 13%) shielded by ceramic material is advised to use. This type of thermocouple is commonly used in combustion chambers. When using K-type thermocouples, very short exposure times are recommended, and preferably combined with a shielding of diameter $> 3mm$.

It was only the temperature at the junction between the two metals inside the thermocouple that was measured. These are the temperatures reported in this work. However, this temperature did, to a variable extent, differ from the temperature of the gas at a given location and time. The temperature difference between the gas, undisturbed by the thermocouple, and the temperature at the junction, forms the main source of errors of measurement. The requirements for a K-type element, is a maximum error reading of the junction temperature of 0.75%, measured in ^0C, or $\pm 2.2K$, whichever is larger [27]. For the temperatures measured in these experiments, this error amounts to no more than $9K$. Thus, the main source of error was the temperature difference between the gas and the junction. The heat balance can be written

$$\begin{bmatrix} \text{Net conductive heat} \\ \text{transfer to the} \\ \text{thermocouple} \end{bmatrix} = \begin{bmatrix} \text{Net radiation} \\ \text{from the} \\ \text{thermocouple} \end{bmatrix}$$

Conductive, and radiative, heat transfer can go to or from a thermocouple. The conductive heat transfer can be split into a convective term (often referred to as a separate mode of heat transfer) from the gas to the surface of the thermocouple shield, and conduction through the shielding onto the thermocouple junction. The radiative heat transfer is the net effect of radiation from the thermocouple shielding to the ambient, from the gas to the thermocouple, and from the ambient to the thermocouple. This yields the equation

$$h(T_g - T_t) + k\frac{dT}{dx} = -\epsilon_t \sigma T_t^4 + \epsilon_g \sigma T_g^4 + \epsilon_r \sigma T_a^4 \tag{7.1}$$

where

h = the convective heat transfer coefficient
T = temperature of; gas $(_g)$, thermocouple$(_t)$, ambient$(_a)$

k = thermal conductivity of shielding
x = distance
ϵ = emissivity of; thermocouple ($_t$), gas ($_g$), resultant of gas/ambient ($_r$)
σ = Stefan-Boltzman constant ($5.67 \times 10^{-8} Wm^{-2}K^{-4}$)

In this experimental work, several of the parameters were not possible to measure. The convective heat transfer coefficient varies with several factors, like the local gas velocity, the temperature difference, the surface properties of the thermocouple, the gas properties, and the geometry of the thermocouple. All of these parameters, except the geometry, changed during the experiments. The emissivity of the thermocouple increased with time during an experiment, due to soot formation at the surface of the shield. The emissivity of the gas underwent rapid changes in time and space due to the flow- and combustion characteristics of the gas, as did the temperatures of air, propane and a large number of reaction products. The net emissivity of the gas/ambient conditions (air, sun, solids etc) varied with view point and time. Also, the surface of the thermocouple shield was expected to act as a catalyzer, giving rise to radical recombination reactions at the surface of the shield.

In an imaginary steady state condition (steady flow, combustion, turbulence etc) the thermocouple readings will still differ from the actual gas temperature. A major part of this is due to the radiative heat loss from the thermocouple. Using equation7.1, the relationship can be expressed as [28]:

$$T_g - T_t = \frac{\sigma\epsilon}{h_c}(T_t^4 - T_a^4) \tag{7.2}$$

Note that the ambient temperature in this case is the effective radiative temperature of the surroundings for the thermocouple.

By substitution of an appropriate heat transfer correlation, an approximate equation can be written [28]:

$$T_g - T_t = \frac{d^{0.55}}{U^{0.45}}(T_t^4 - T_a^4) \tag{7.3}$$

Where d is the thermocouple diameter, and U is the flow velocity over the thermocouple. From this, it can be seen that the most favorable condition is when using a small diameter thermocouple in a high gas velocity field, at low gas temperatures. In the experiments carried out here, where the diameter was kept constant, it means that the errors were dictated by the thermocouple position in the the flame, due to varying temperatures and flow velocities. However, an assessment of T_a was not obtained.

Due to the rapid changes in temperature in the turbulent gas jet, and the thermal inertia of the thermocouples, the readings tended not to show the peak values. A smoothing of the time-temperature curve for a fixed point was thus expected. The extent of the smoothing will be a function of the time constant of the thermocouple. A thermally thick thermocouple, as in this case, will tend to smoothen the curve.

The temperatures were logged at a frequency of $0.5Hz$. A single reading every 2 seconds in the gas where the temperature changed rapidly, was not able to detect what happened between the readings. However, in this case, the thermally thick thermocouple was beneficial, due to the fact that it tended

to store the heat transferred until the next temperature reading. Thus, the readings was expected to give adequate information to use for objects with larger time constants than the thermocouple's.

Due to the uncertainties of measuring the temperatures in absolute terms, care should be taken in interpreting the results. All the major error sources are assumed to be negligible by using relative temperatures instead. This means that the shape of a temperature field, i.e the shape of the isothermal lines, should be considered, rather than the absolute temperatures. By doing this, error sources such as the changing emissivity of the thermocouple surface with time, the convective heat transfer coefficient or the ability of the thermocouple to act as a catalyzer, can be neglected. Still, there will be error sources even in relative terms, such as the conductivity of the thermocouple shielding. It will vary with temperature. This will affect the distance between the isothermal lines, but not its main shape. By this, it is meant that a jagged isothermal line will be more jagged or less jagged by this effect, but it will not turn into a smooth curve. Therefore, the focus of these experiments are in terms of the shape of the temperature fields.

Radiation measurements

Before discussing the error sources of the measurements, it is important to point out that the results from these experiments can not be used to establish exact radiative fractions of the total heat release from the flame. Only distinct points at a small number of positions have been measured. Although a comparison can be made based on the measurements from each pair of radiometers and total heat flux meters, it does not mean that the radiative fraction can be calculated, even at a single point. The radiometer is calibrated for the actual, incident radiant heat flux at a small area on the probe. But the convective part of the total heat flux measurement is a function of the casing material and surface of the probe. In that sense, it might have been better to compare the radiation to the total heat release rate of the combustion. However, there would be a problem with estimating the total heat flux based on a few single points. In sum, all this means that for a good estimate of the radiative fraction for the flame to be carried out, a different, and much larger experimental setup, would have been necessary.

Inside the flame

Due to soot formation at the black coated sensors, the readings from the radiometers inside the flame were not used, see subsections 5.3.2 and 6.1.2. That made it necessary to calculate the convective part of the total heat flux meter readings and subtract it from the measured values. This extra step introduced an unwanted source of error. The manufacturer of the gauges informed that the emissivity of the gauge casing was 0.8, and this value was used in the calculations. However, the fire affected the casing. It was not possible to measure the emissivity of the casing throughout the experiment, see the photographs in figure 6.14 for a visualization of this problem.

Outside the flame

There is an uncertainty connected to the selection of readings from the radiometers placed outside the flame, see the above section. But the readings show only small deviations.

In addition, the ellipsoidal radiometers (Medtherm 64 series) used in the experiments has an accuracy of $\pm 3\%$, and a field of view of more than 160^0 (source: Medtherm corporation), see figure 7.1. The virtual radiometer used by Kameleon has a field of view of 180^0. This represents an additional source of error between the two readings. In the worst case, the radiation in the sector $80^0 \rightarrow 90^0$ from an axis perpendicular to the aperture plane of the radiometer, will not be read by the real radiometer. The view factor varies as a cosine function with this angle. Thus, the relative, geometrical error of the reading can be up to:

$$\int_{80}^{90} cos\theta d\theta = [sin\theta]_{80}^{90} \approx 0.015$$

where θ is the angle defined on figure 7.1. The interpretation of the geometrical error should be treated with care. The real radiometers used in the experiments reads the weighed average exposure of radiation onto a surface that is oriented in the same direction as the aperture of the radiometer. The weighed values arise from the orientation, i.e the view factor of the aperture.

The reading is calibrated for a 180^0 view. In the case where the radiometer is placed inside the flame, at the jet axis, there will be a thick flame along this axis in either direction. The flame, as seen from the radiometer, will be thinner than this in any direction perpendicular to the jet axis. Thus, the radiometer will not be able to read the thickest part of the flame, i.e where $\theta = 80^0 \rightarrow 90^0$. In this case, where there is a large contribution of radiation from the blind sector of the radiometer, a real, plane surface will receive more radiation than what is read by the radiometer. On the other hand, where the radiometer is placed well outside the flame, with the aperture pointing towards the flame, the real radiometer will give too large values compared to a plane surface, since it is calibrated for a 180^0 view.

In an extreme case, it can be imagined that there is no radiation in the region $\theta = 0^0 \rightarrow 80^0$, and there is some radiation in the region $\theta = 80^0 \rightarrow 90^0$. In this case, the geometrical error will $\rightarrow \infty$.

Thus, the total error resulting from the geometry of the radiometer can not be assessed accurately for the case where it is situated inside the flame.

In the opposite case, where the real radiometer is placed outside the flame, and the average radiation in the region $\theta = 0^0 \rightarrow 80^0$ is clearly larger than the radiation in the region $\theta = 80^0 \rightarrow 90^0$, the total error will amount to no more than the sum of the accuracy of the radiometer ($\pm 3\%$), and the geometrical error ($-1,5\% \rightarrow 0\%$). Thus, assuming that the filtering of the measurement data is performed properly, the total error will be in the region $-4,5\% \rightarrow +3,0\%$ for radiometers placed outside the flame.

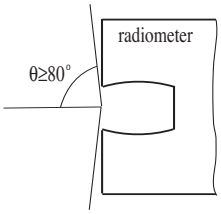

Figure 7.1: View angle of radiometer. The total view angle is $\geq 160^0$

7.2 Heat transfer to a cross-flow cylinder

Although the steel cylinder would be thermally thicker than any commercially available pipe or tube, the correct locations of the peak values for the heat transfer would be unaffected by this fact. Due to this thermal thickness, caused by a cylinder wall thickness of $43.5mm$, the time dependent fluctuations in smoke gas temperature, turbulent flow, emissivity, radiation and convection was *not* registered by the cylinder. Therefore, the measurements can be regarded as the time-averaged combined effect of these fluctuations.

By looking at Newton's law of cooling $q'' = h(T_s - T_\infty)$, one could expect the heat transfer to the cylinder to be at a maximum where the flow velocity past the cylinder is at its peak value. This is where the flame temperature, T_∞, can be regarded as the highest, since the rate of change of temperature with regard to distance, $\frac{\delta T}{\delta y}$, has got its maximum value here, i.e over the top and under the bottom of the cylinder. However, it turned out that this was not the case.

Another possible outcome of the experiment, could have been that the cylinder itself would generate additional turbulence as the gas flow passed its curved surface, causing an increased rate of reaction at the rear side. But this was not the case either. A possible explanation for this can be that with a nozzle diameter of $11mm$, positioned approximately $1m$ above the ground, and a cylinder diameter of $160mm$, the whirls of sizes similar to the Kolmogorov length scale, and up to $> 1m$, were already present. Also, a mixing induced by the cylinder may not have had any effect if it already were mixed to an optimum, but not necessarily stoichiometric, degree before reaching the cylinder.

The experiments clearly showed that the maximum heat transfer occurred at the front of the cylinder. There are at least two possible reasons for this, or the combination of the two, that can explain this result.

Firstly, at the front, the gas pressure towards the cylinder surface is higher than in any other part around the circumference. This cause an increase in the ability of the gas to transfer heat to the cylinder, i.e the convective heat transfer coefficient, h, in Newton's law of cooling has got its maximum value

here, causing a larger heat transfer by convection.

Secondly, the front has got a view to a thicker flame than the top and bottom, giving rise to a larger heat transfer by radiation. However, this does not give a major contribution to the overall heat transfer. In experiments 1-3, the major part of the flame was at the rear, but the heat transfer at the rear in these experiments were only marginally larger ($T = 140 - 230^0C$) than the rear in experiments 4-6 ($T = 140 - 160^0C$), where most of the flame was viewed from the front. This limited relative effect of radiation is supported by the works of Staggs and Phylaktou [23], see section 4.2.

Another interesting observation, was that the heat transfer was larger when the cylinder was placed at $3.0m$ away from the nozzle, than it was when the cylinder was at a distance $5.4m$. Bearing in mind that the temperature measurements of the undisturbed flame, showed a maximum at $\approx 4.5m$, one would expect the maximum heat transfer to occur during the experiments carried out at a distance of $5.4m$. An explanation to this can be that the flow velocity has decreased significantly. This cause the pressure in front of the cylinder to decrease, which in turn cause the convective heat transfer coefficient to decrease.

Chapter 8

Conclusions

8.1 Characterization of experimental jet flame

The experiments showed that

- the length of the visible flame was $\approx 5.5m$, with a lift-off distance of $0.6m$
- the highest temperature region of the jet flame was $\approx 70\%$ along the visible flame length (i.e not including lift-off). The maximum temperature in the flame was in the region $1200 - 1300^0C$
- up to $\approx 3m$, there was a fuel rich region along the centre trajectory of the flame, where the temperature was $\approx 200^0C$ less than in the stoichiometric region, $0.3m$ away from the centre line
- the radiation fraction along the jet trajectory at positions 25%, 50%, 70%, and 95% downstream of the visible flame length was 28%, 57%, 73%, and 63%, respectively
- moving outside the flame perpendicular to the jet axis, the radiation fraction gradually increased. At $3m$ distance from the centerline, it was equal to the total heat flux. This indicated that the convection fraction was close to zero
- the radiation heat flux sensors were extremely sensitive to unclean environment. Even when applying nitrogen for purging, it did not keep the soot and other particles away from the inner surface of the gauge's restrictor
- the CFD-code KFX predicted a correct flame length, but estimated a slightly shorter lift-off distance
- the end part of the KFX-flame was more influenced by buoyancy and deviated some from that of the experiment
- the measurements showed more irregular shaped temperature fields compared to the simulated
- the measurements showed larger fluctuations in the temperature fields compared to the simulated

- the maximum measured radiative heat flux inside the flame was $185 kW/m^2$. The maximum simulated radiative heat flux was $193 kW/m^2$, representing a deviation of 4.3%
- the maximum measured total heat flux was $256 kW/m^2$

8.2 Heat transfer to a cross-flow cylinder

Based on the experiments, and partly backed up by the available literature in the field, it could be concluded that

- convection is the major contributor to the total heat transfer from a turbulent jet flame to a steel cylinder impinged by the flame
- a steel cylinder impinged by a jet flame, will be exposed to the largest rate of heat transfer at the side facing the flame. This means that in these experiments, no high levels of turbulence induced thermal loading could be detected at the back
- for an object impinged by a gas flame, the heat transfer is dominated by the gas *pressure* near the surface of the object, rather than the *velocity* over the surface

Chapter 9

Recommendations for further work

9.1 Characterization of experimental jet flame

Putting instrumentation into the flame, will cause a disruption of the flow, chemical reactions, temperatures etc. Therefore, non disruptive techniques like laser doppler should be applied for the study of detailed flow characteristics and chemical reactions. In addition, it would be very useful to quantify the errors in the readings from instrumentation put into the flame. To do this, a combination of disruptive and non disruptive techniques should be applied.

The heat flux gauges are exposed to a significant thermal erosion when located within the flame. Therefore, the sensor surfaces are sensitive to being contaminated by soot. To avoid or minimize this problem, one possible alternative might be to locate the heat flux meters, in particular the radiometers, with their sensors oriented along the direction of the jet, rather than transverse to the flow. This requires the whole device, connections included, to be properly insulated.

9.2 Heat transfer to a cross-flow cylinder

During the experiments, the cylinder was exposed to an erosive flame, causing a risk of breakdown of the equipment. To be sure of being able to complete the experiments, the heat transfer in the cylinder was therefore not brought to a steady state. It was near enough to give a good indication of where the thermal loading was largest. But bringing the system to a steady state would represent one step further in gaining detailed knowledge of the heat transfer in this setup.

Also, further investigations should be done in order to quantify the relative contribution of heat transfer by convection compared to radiation.

Detailed multiscale models should be developed for describing turbulent combustion and its effect on the heat transfer. With the rapidly increasing computational power available, this should be possible. However, science is still

far away from achieving a complete description of the combustion chemistry, turbulent flow, and the gas/solid interaction at a molecular level.

Appendix A

- Published Article

This article was presented as a poster paper in the 10^{th} International Fire Science & Engineering Conference Interflam 2004, Edinburgh, Scotland, July 2004; and was published in Volume 1 of the Conference Proceedings (pp. 683-689).

CHARACTERIZATION OF A HIGH MOMENTUM TURBULENT JET FLAME, A COMPARATIVE STUDY

Leiv Anfin Drange*, Zia Kazemi, Torgrim Log
Stord/Haugesund University College, Norway

Bjørn F. Magnussen
Computational Industry Technologies AS, Norway

ABSTRACT

An experimental full scale characterization of a turbulent propane jet flame has been made in terms of temperatures and radiation. Sonic propane gas releases were achieved at steady pressure and near steady flow. The size of the fire was 13-14 MW. The pressure drop across the horizontally mounted nozzle was 10.3 barg. The experimental setup was simulated using the CFD-code Kameleon FireEx, and characterizations were made for temperature, radiation and gas velocity. The results from experiments and simulations were visualized and compared using interpolation techniques. Time-averaged values were plotted. The simulation results showed good correlations with the experiments. Some deviation was found in terms of radiation. The turbulence equations in the $k-\epsilon$-model compute the average values which then results in a more smooth flame, while the physical setup produced more jagged fields. The simulation predicted slightly higher influence of buoyancy in the back 10 % of the flame, and a shorter lift-off at nozzle. The later causes consequently the flame to move somewhat near the release point. There was a small gap between the measured and the simulated values for radiation within the flames. The deviation at comparable positions is of magnitude 14 %.

INTRODUCTION

The aim of this work has been to validate information achieved by simulation on temperature and radiation fields within and near a high momentum turbulent jet flame. Also, information of the velocities involved at different points in the flow field was needed for further studies. However, there was no available equipment or method to measure this. Therefore, the fluid dynamic effects were studied only by simulation. The characterization was done for a 13-14 MW propane gas jet flame (average burning rate 0.3 kg/s). The purpose of characterizing the flame was to understand the flame properties better, which indeed is a part of a bigger project. Radiative and convective heat transfer inside and around the flame was studied.

The pressure drop for propane in gas phase across the nozzle was increased compared to the vapor pressure at ambient temperature. It was done by increasing the pressure by preheating prior to release of propane in liquid phase, before evaporating it into gas phase. This increased the turbulent energy of the jet compared to a release at ambient temperature. The effects of these mechanisms were measured by placing a number of thermocouples, radiometers and total heat flux gages, the latter two commonly called heat flux gages, into and around the region of combustion.

EXPERIMENTS

A rig consisting of a 14 m^3 liquid propane tank, a pump and an evaporator to convert the propane from liquid to gas phase was used as a fire source. The liquid propane was led through an outlet nozzle and expanded to ambient pressure through a series of shock waves. The physical dimensions of the nozzle are shown in Fig. 1. To ensure that the propane was in gas phase at release, a liquid switch was installed between the evaporator and the nozzle, shutting down the supply of propane in case of liquid

*Drange and Kazemi have made equal contributions in the process of producing this article.

passing through the evaporator. Three pilot flames at low pressure were applied to the main jet stream approximately 400 mm downstream of the outlet. This was necessary in order to avoid blowout of the flame, due to the high velocity gradients in the gas jet.

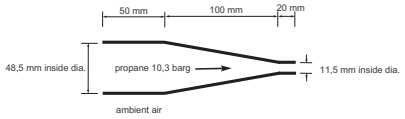

Figure 1: *Outlet nozzle*

Temperatures were recorded at 840 points distributed over seven different cross sections in the flame. The cross sections normal to jet axis were located at distances 2.5, 3.4, 3.7, 4.0, 4.3, 4.6 and 5.5 m from the outlet of the gas. Each cross section formed a grid of 120 measurement points. The sections had their center points on the jet axis and were positioned in y-z-directions as shown in Fig. 2. The available 40 thermocouples were arranged in a grid of 10 rows (150 mm apart) and 4 columns (150 mm apart), and the arrangement could easily be moved across and along the jet axis. This demanded three sets of experiments to be performed at each section, which consisted of 120 single temperature measurements. Thus, a total number of 21 experiments were performed, in order to cover a total of 840 measurement points.

The thermocouples used were of K-type, single-shield of 1.6 mm outside diameter with 0.23 mm conductors isolated by magnesium oxide. The thermocouples in each column were supported on an angle iron 20×20 mm. The four iron angles in each arrangement were located with their angle-sides facing the jet nozzle in order to minimize disturbances of the gas flow. In order to eliminate or minimize the effect of radiation on thermocouple readings originated from glowing metal, their tips were placed approximately 100 mm upstream from the angle irons and parallel to the jet axis. A photograph from one of the experiments is shown in Fig. 2.

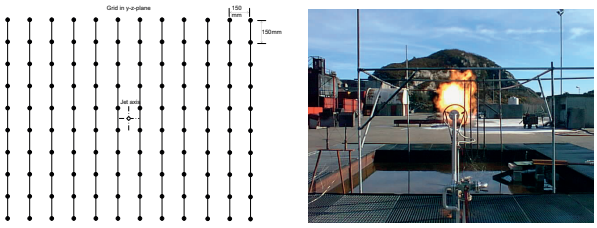

Figure 2: *Setup for temperature measurements*

The experiments were conducted outdoors under calm wind conditions. The wind speed varied from $0.0 - 2.0$ m/s at angles from $45° - 270°$ measured anticlockwise from a direction pointing upstream of the jet. It was mostly in the range of $0.5 - 1.5$ m/s at approximately 150°.

Heat flux measurements were carried out using Medtherm heat flux meters (Schmidt-Boelter sensor type). Six pairs of total heat and radiation flux meters were mounted within and around the flame region. A total flux meter measures sum of the radiation and convection heat. All flux meters were placed at the jet axis level, i.e. at $z = 0.0$ m. Four pairs were directly located in the flame zone, along the jet axis, at $x = 2.0, 3.3, 4.6$ and 5.9 m, while the other two pairs were placed outside the flame at the locations $x = 4.0$ m, $y = -1.5$ m, and $x = 4.0$ m, $y = 3.0$ m. All flux meters were pointing horizontally, with their centerlines normal to the nozzle centerline so that the surfaces of the flux meters were parallel to the jet axis or gas flow. They were supported in the same manner as the thermocouples. In order to minimize, or avoid, the effect of adjacent glowing angle iron, acting as a support for the gages, the support was located

100 mm behind the gage surface. Each pair of the flux meters were water cooled, except for those placed in the low radiation field outside the jet flame. In addition, the open casing (the view restrictor) around the black body of the radiation flux meters located inside the combustion zone were nitrogen purged in order to keep the sensor surfaces clean from soot and other particles.

CFD MODELLING

The CFD program Kameleon FireEx 2000 (denoted KFX) was used for the modelling. The simulator uses a Cartesian finite volume technique to solve the averaged basic transport equations from fluid dynamics. Sub-models include among others the $k - \epsilon$ turbulence model [1, 2]. Prior to the experimental work, number of CFD-simulations was carried out using KFX in order to point out the proper positions for instrumentation (thermocouples and heat flux meters). After the experimental part of the work was completed, similar scenarios were modeled in KFX and simulated. The gas velocity profile along the flame path was simulated, but not measured experimentally.

The geometry used had dimensions $13 \times 7 \times 9$ m ($LxWxH$) with a grid resolution $63 \times 55 \times 60$ equivalent to 207 900 grid nodes. The volume consisted of a floor boundary with isothermal solid cells mostly covered with solid isothermal core as domain cells. These cells formed a pool which was located under the jet flame area. This water pool protected the concrete floor from the radiative heat in the experiments. The walls and roof were defined as wind boundary cells. The nozzle was placed 2.0 m above the floor at the point $(x, y, z) = (0, 0, 0)$ with jet release in the positive x-direction. The mesh resolution was distributed fairly fine around the nozzle, gradually increasing with decreasing flow speed. The view is provided in Fig. 3. The figure on the left side reflects the concept used for measuring the heat flux in the experiments.

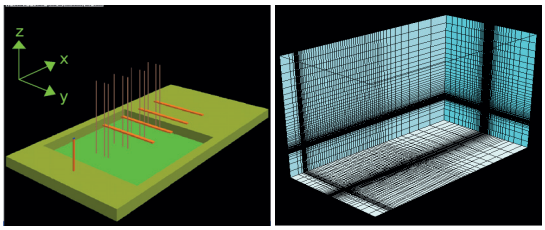

Figure 3: *Setup of simulation model*

The specification of scenarios simulated was similar to the experimental work, i.e. mass flow rate of propane, system pressure, temperature, nozzle geometry, type of thermocouple, etc. as described earlier. As previously mentioned the wind velocity in the experiments was very low (i.e. $0.5 - 1.5$ m/s), but quite varying in direction. Due to this matter its value in simulation was assumed to be zero. As discussed later in RESULTS AND DISCUSSION, similar adjustments were made in plotting the temperature values from the experiment so that the center of temperature field lied on $y = 0.0$ m. The transient time step was set to 1.0e-05 s and a Courant number to 100. Criterion for convergence was based on carbon and hydrogen balance in calculation domain. To verify this, the difference between the carbon and/or hydrogen entering and leaving the calculation domain should not exceed approximately 3 % according to ComputIT [3]. For this study the values lied under 0.3 %.

The calculated parameters were temperature, radiative heat flux, and gas velocity. The location of computed points for temperature and heat flux is as described under EXPERIMENTS. While the velocity of the gas was calculated at 65 different positions along the flame path.

The temperature difference between the metal junction inside the thermocouple and the actual gas temperature was calculated by KFX. The model works in the opposite direction of what an experiment would do, by first calculating a gas temperature. Based on heat balances, a theoretical thermocouple reading was calculated.

RESULTS AND DISCUSSION

As stated in the previous section the wind velocity was set to zero. In order to match this in treating the results, similar adjustments were made in plotting the temperature values from the experiment so that the center of temperature field lied on $y = 0.0\ m$ without having any consequences for their numerical values.

The results of field measurements and CFD simulations compared quite well for the temperatures, see Fig. 4. Only a minor difference was observed concerning buoyancy forces on the end part of the flame (approximately 10 %) in simulations compared with the experiments which indeed is insignificant as it can be seen in Fig. 4 & 5.

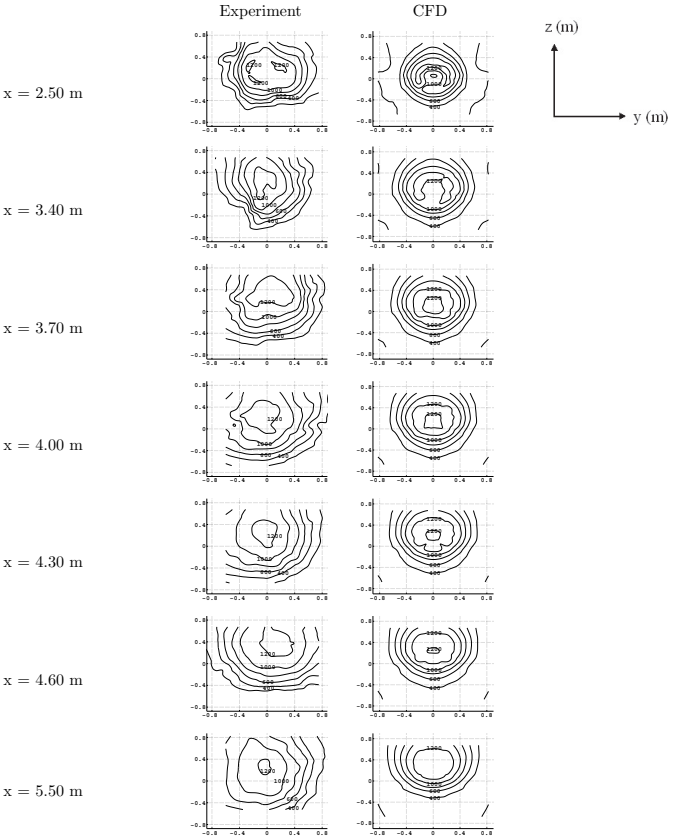

Figure 4: *Temperatures (°C) at various distances, x (m), from nozzle*

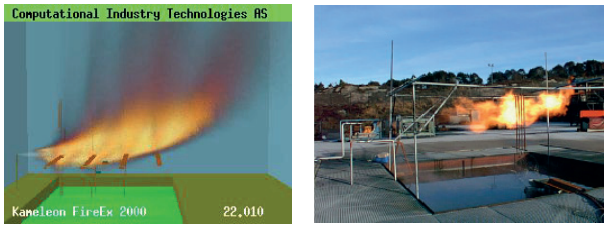

Figure 5: *Visual comparison of simulation and experiment*

Another matter which visually distinguished these two flames was the smooth temperature fields in the simulations contra the unsteady temperature fields from the experiments. Because the turbulence equations in the $k-\epsilon$-model calculate the average values which then result in a more smooth flame, while the experimental setup produced more turbulent and jagged fields. This might be overcome by increasing the number of grid nodes considerably. But this in turn demands powerful computer capacity which indeed is limited. Even though having access to such computers, it would never give a 100 % realistic picture of a turbulent flame [3]. The other possible reasons might be that in case of the simulation the wind effects were ignored (set to zero) and the effects of angle irons in the flame (used to support the thermocouples and flux meters in experiments) and the surrounding objects (buildings, equipment etc.) were neglected.

Due to closure of the liquid switch several times during the heat flux experiments, the data recorded during closure had to be ignored. Ignoring the data was decided in accordance with manual time registration for closure. These data compared well with the changes in heat flux recorded by computer.

In order to eliminate the convective heat transfer when measuring radiation, the heat flux sensor surface is covered with a window attachment. Internal surface of the window which is formed as an ellipsoidal cavity is gold plated and is highly polished.

Although nitrogen purging was applied to keep the sensor surface clean during the experiments, the gas flow inevitably entered the window and covered the polished area by soot. This resulted in emissivity reduction of the reflecting plate, causing unreliable and very low radiation values except the one located farthest outside the flame at $y = 3.0\ m$

The plotted radiation results from experiment are then calculated values based on the measured temperatures and simulated gas velocities. Equation (1) was used to calculate the convective heat transfer coefficient of the gas [4].

$$h = 0.033 \frac{\rho c_p \nu^{0.2} V^{0.8}}{d^{0.2}} \quad (kW/m^2\ K) \tag{1}$$

where:

$$\begin{aligned} \rho &= density\ (kg/m^3) \\ C_p &= specific\ heat\ capacity\ (kJ/kg\ K) \\ \nu &= kinematic\ viscosity\ (m^2/s) \\ V &= velocity\ (m/s) \\ d &= flux\ outside\ diameter\ (m) \end{aligned}$$

By using the equation $Q_{convection} = h(T_2 - T_1)$ the amount of heat convection transferred to the heat flux transducers was calculated. T_1 and T_2 are the heat flux body and the flue gas temperature, respectively. By subtracting this value from the total heat flux measured, a theoretical radiation corresponding to the experimental value was then found and the results are plotted in the diagrams shown in Fig. 6. Heat flux

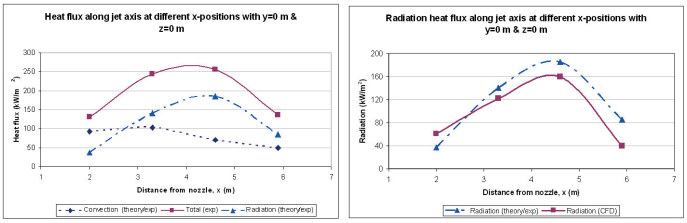

Figure 6: *Measured and calculated heat flux along jet centerline*

measured and simulated outside the flame, and gas velocity calculated along the flame path are shown in Fig. 7. The flame had approximately a diameter of 1.0 m and a length equivalent to 7.0 m.

The results of radiation show also fairly correlation for two methods at comparable positions. But some deviation was anyhow found. The simulation predicted slightly a shorter lift-off at the outlet. The later is due to the fact that the CFD-code uses the default value for methane [3]. This causes consequently the flame to move somewhat near the release point. As a result the first position of the measurement, i.e. 2.0 m from the nozzle will lie in a more active combustion zone in case of simulation. This will be reflected in terms of higher radiation value as it can be seen in Fig. 6. For the same reason the situation is reverse on the other end of the flame, i.e. combustion accomplishes earlier and in addition due to higher buoyancy effects the flame bends off earlier and resulting the last position (5.9 m from the outlet) to lie almost outside the flame region. This will cause lower value for radiation in simulation. While the position 2 (3.3 m) and 3 (4.6 m) in both cases are well situated in flame zone. The deviation for these comparable positions is at most of magnitude 14 %

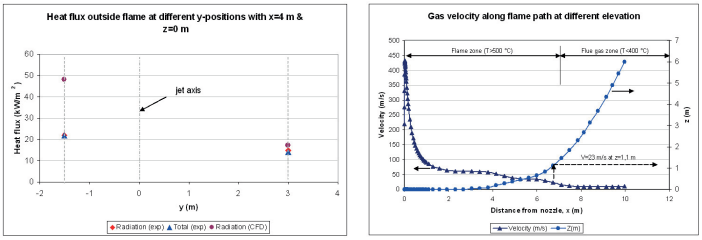

(a) Measured and calculated heat flux outside flame

(b) Calculated gas velocity along flame path

Figure 7: *Heat flux and gas velocity*

CONCLUSION

The simulated results for the temperatures compared well with the measured values. The two methods show anyhow some minor deviation on the heat flux radiation. Using the transport equations in a $k-\epsilon$-model tends to return smooth temperature fields, while a physical setup produces more jagged fields.

The simulation predicted slightly higher influence of buoyancy on the back 10 % of the flame. This effect combined with a shorter lift-off stand for the major part of the radiation deviation. Indeed a physical correction for later will further bring these two flames closer to each other.

However in order to draw a trustworthy conclusion concerning radiation differences and rely on the radiation results from the field tests, we believe a more experimental investigation is necessary. Because the

radiation heat flux meters are pretty sensitive and a far better measurement method is required in order to keep their surfaces clean despite an unclean environment.

Altogether the CFD-code KFX seems to estimate fairly the measured parameters and could well be used to minimize the costly experimental works.

ACKNOWLEDGEMENT

The authors would like to thank the employees at ComputIT AS for their valuable support in the process of simulation in this work, in particular Mr. Nils Lilleheie and Mr. Bjørn Erling Vembe.

REFERENCES

[1] Vembe, B.E.; Rian, K.E.; Holen, J.K.; Lilleheie, N.I.; Grimsmo, B.; Magnussen, B.F. *Kameleon FireEx 2000 User Manual*, ComputIT report no. R0122.

[2] Vembe, B.E.; Rian, K.E.; Holen, J.K.; Lilleheie, N.I.; Grimsmo, B.; Myhrvold, T. *Kameleon FireEx 2000 Theory Manual*, ComputIT report no. R0123.

[3] ComputIT (Computational Industry Technologies AS) *Kameleon FireEx 2000*, Bassengbakken 1, N-7042 Trondheim, Norway.

[4] Kreith, F; Black, W.Z. *Basic Heat Transfer*, Harper & Row, ISBN 0-711-22518-8.

Bibliography

[1] Kazemi, Z.
Droplet Impaction on Solid Surfaces Exposed to Impinging Jet Fires,
ISBN 82-471-8108-8, Doctoral dissertation NTNU, 2006:169

[2] Kazemi, Z.
Private communications

[3] Warnats, J.; Maas, U.; Dibble, R.W.
Combustion. Physical and Chemical Fundamentals, Modeling and Simulation, Experiments, Pollutant Formation,
Springer-Verlag, 2000

[4] Cowley, L.T.; Johnson, A.D.
Blast and Fire Engineering Project for Topside Structures, Fire Loading series,
Shell International Research Mij. BV, Feb, 1991

[5] Ertesvåg, I.
Turbulent Strøyming og Forbrenning - Frå turbulensteori til ingeniørverkty (in Norwegian),
Tapir akademisk forlag, Trondheim, Norway, 2000. ISBN 82-519-1568-6

[6] Launder, B.E.; Sharma, B.I.
Application of the energy-dissipation model of turbulence to the calculation of flow near a spinning disc,
Letters in heat and mass transfer 1, 1974

[7] Jones, W.P.; Launder, B.E.
The Prediction of Laminarization with a Two-equation Model of Turbulence,
Int. J. of Heat and Mass Transfer 15, pp. 301-314, 1972

[8] Launder, B.E.; Spalding, D.B.
The Numerical Computation of Turbulent Flows,

Computer methods in appl. Mech. and Eng. 3, pp 269-289, 1974

[9] Zhang,F.
A PDF Module for Turbulent Deflagration Structure Computation
Defense Research Establishment Suffield, Alberta, Canada, November, 1999

[10] Borghi, R.; Destriau, M.
Combustion and flames; Chemical and physical principles,
ISBN 2-7108-0740-8, 1998

[11] Incropera, Frank P.; DeWitt, David P.
Introduction to Heat transfer,
John Wiley & Sons, Inc. 1996

[12] Cumber,, P.S.; Spearpoint, M.
A computational flame length methodology for propane jet fires,
Fire Safety Journal, Vol. 41, Issue 3 , pp 215-228, 2006

[13] Heskestad,G.
Luminous heights of turbulent diffusion flames,
Fire Safety Journal, Vol. 5, Issue 2 , pp 103-108, 1983

[14] Becker,H.A.; Liang,D.
Visible length of vertical free turbulent diffusion flames,
Combustion and Flame, Vol. 32, Issue 11, pp 115-137, 1978

[15] Hawthorne,W.R.; Wedell,D.S.; Hottel,H.C.
Mixing and combustion in turbulent gas jets,
Third Int. symposium on combustion, Baltimore: Williams and Wilkins, pp 266-288, 1949

[16] Kalghatgi,G.T.
Lift-off heights and visible lengths of vertical turbulent diffusion flames in still air,
Combust. Sci. Technology, vol. 41, pp 17-29, 1984

[17] Sugawa,O.; Sakai,K.
Flame length and width produced by ejected propane gas fuel from a pipe,
13^{th} meeting of the UNJR panel on research and safety, NISTIR 6030, pp 401-411, 1997

[18] Pitts, W.M.; Murthy, A.V.; Ris, J.L.; Filtz, J.-R.; Nygård, K.; Smith, D.; Wetterlund, I.
Round robin study of total heat flux gauge calibration at fire laboratories,
Fire Safety Journal, Vol. 41, Issue 6 , pp 459-475, 2006

[19] Enquist,W.E.B.

Commun.Math.Sci 1, pp 87-132, 2003

[20] Peters, N.
Multiscale combustion and turbulence,
Proceedings of the Combustion Institute, Vol. 32, Issue 1 , pp 1-25, 2009

[21] Mowrer, F.W.
An analysis of effective thermal properties of thermally thick materials,
Fire Safety Journal, Vol. 40, Issue 5 , pp 395-410, 2005

[22] Gardner, L.; Ng, K.T.
Temperature development in structural stainless steel sections exposed to fire,
Fire Safety Journal, Vol. 41, Issue 3 , pp 185-203, 2005

[23] Staggs, J.E.J.; Phylaktou, H.N.
The effect of emissivity on the performance of steel in furnace tests,
Fire Safety Journal, Vol. 43, Issue 1 , pp 1-10, 2008

[24] Hoffie, F.
Convection Calibration of Schmidt-Boelter Heat Flux Gages in Shear and Stagnation Air Flow,
MSc thesis, Virginia Tech., U.S , 2006

[25] Vembe, B.E.; Lilleheie, N.I.; Holen, J.K.; Magnussen, B.F.
Kameleon FireEx - A Simulator for Gas Dispersion and Fires,
Paper presented for "1998 International Gas Research Conference", 1998

[26] Vembe, B.E.; Rian, K.E.; Holen, J.K.; Lilleheie, N.I.; Grimsmo, B.; Magnussen, B.F.
Kameleon FireEx 99 user manual,
ISBN 82-594-1724-3, 2000

[27] Jones, J. C.,
Suggestions Towards Improved Reliability of Thermocouple Temperature Measurement in Combustion Tests,
Thermal Measurements: The Foundation of Fire Standards, ASTM STP

1427, L.A. Gritzo and N.J. Alvares, Eds., ASTM International, West Conshohocken, PA, 2002

[28] Pitts, W.M.; Braun, E.; Peacock, R.D; Mitler, H.E.; Johnsson, E.L.; Reneke, P.A.; Blevins, L.G.
Temperature Uncertainties for Bare-Bead and Aspirated Thermocouple Measurements in Fire Environments,
Joint meeting: Combustion Institute. Proceedings March 1999, and NIST annual conference on Fire Research, Book of abstracts, 1998

PART II - PROPANE JET STABILITY: BLOWOUT LIMITS

Contents

List of Figures

List of Tables

Chapter 1

Introduction

The release of gas e.g in terms of leakages from transport pipes or processing equipment at industrial sites, can cause severe human or material losses. Such releases result in gas clouds and a potential gas explosion if ignited. On the other hand, an ignited gas release will cause a fire, normally a turbulent jet fire.

Ignition of discharges of fluid in open surroundings do not necessarily produce stable jet flames. The discharge conditions can be such that flames cannot burn back to form a steady flame, or, even if the ignition is pilotet, the resulting flames blow off downstream and are extinguished. Whilst a flame might be unstable under open conditions, stabilization can occur on nearby surfaces and walls. This is due to the loss in momentum resulting in a mixing of fuel and air at low velocity fluctuations, giving rise to conditions where the chemical reaction rates are faster than the physical dissipation rates [1].

The effect of a fire will often be less devastating than that of an explosion, thus a fire might be preferred where there is a gas release. The fire will be extinguished by a shutdown of the release. It is important that the combustion process is running through the shutdown process. Thus it is necessary to be able to predict the stability of a turbulent gas jet flame.

For circular release apertures greater than a certain critical diameter, all discharges produce stable jet flames. Below the critical diameter, low flow velocity and also much higher flow velocities give rise to conditions where stable jet fires are possible. There is, however, an intermediate velocity region where flames are not stable. The upper and lower critical velocity bounds for stability depend on the aperture diameter, and they merge at the critical diameter. The critical diameter is fuel composition dependent [2].

The phenomenon was observed experimentally for hydrogen jets by Annushkin and Sverdlov [3] and application of their work to methane flows indicated a critical diameter for methane of 20 mm.

Kalghatgi studied low pressure methane flame stability directly in still air [4] and cross flows [5] and obtained accurate data on the lower critical pressure for flame stability for releases from apertures smaller than the critical diameter. The results were extended by McCaffrey and D.D. Evans [6]. The results of all these workers suggested a critical aperture diameter for methane jets of 42-47 mm.

Measurements of the critical aperture and the upper critical pressures for vertical methane releases were obtained in a series of full-scale experiments

conducted by Birch et.al of British Gas [7]. They examined apertures between 5 and 50 mm diameter with drive pressures up to 80 bara. The low pressure results of Kalghatgi and McCaffrey were confirmed and a directly determined critical aperture diameter of 30 mm was obtained. The literature recommends use of these experimental data in flame stability correlations for methane.

It must be noted that the stability of a jet flame will depend on the release geometry. Wakes et.al concludes that a high aspect ratio jet behaves in a very different way to that of an axisymmetric jet, even far downstream [8]. Geometry dependant effects like saddleback velocity distribution and jet flapping were observed.

A non premixed gas jet will, at low flow rate in still air, form a flame at the burner. When the flow rate is increased beyond a value called the lift-off stability limit, the flame will stabilize at a distance from the burner tip. A further increase in flow rate will cause the flame to extinguish at a value called the blow-out stability limit. Kalghatgi [4] performed a series of experiments for various gases and gas mixtures. By using a set of non-dimensional groupings of the flow and gas parameters that affect blow-out stability, an empirical formula was found for all the different gases used.

Chapter 2

Objects of work

Annushkin/Sverdlov and Kalghatgi made models firmly documented through experiments. However, the models are based on variables that require some amount of effort to assess, in order to find out if a jet flame will blow out or not. Therefore, it was of interest to find a more easily available model that could be used, either as an independent assessment of a situation, or as a quick reference before a more detailed analysis could be carried out.

Accidental situations causing ignited propane gas jets that can occur in the process industry were of special interest for this project. Therefore, the two situations most likely to occur, were found to be broken pipes due to mechanical overload of some kind, such as falling objects, collision between vehicles and pipes etc. This situation has been simulated by means of axisymmetric jets, i.e cylindrical nozzles with circular cross sections. The second situation that was likely to occur, was leakage from bad flange connections in the pipe systems, a situation where the flow has a high aspect ratio, i.e a wide but short gap between the flanges. This situation has not been simulated.

There were three objects of this work:

- to establish a simplified, empirical model of jet releases from circular cross section outlets of propane in gas phase, describing the flow at the upper blowout limit, $Q_u = f(d)$, and the flow at the lower blowout limit, $Q_l = f(d)$
- to establish a critical diameter, d_{cr}, for propane, beyond which, an ignited jet would not blow out, regardless of flow
- to examine the effect of tilted outlets on the blowout stability

The flows in this work represented simulations of pipes with inside diameters equal to the inside diameters of the nozzles.

Chapter 3

Basic theory on blowout properties

The phenomenon of a flame extinction can be caused by several mechanisms. The most common are the cases where the fraction of fuel(s) drop(s) below the Lower Flammability Limit (LFL), or the concentration of oxidant drops in a confined space, so that the mixture is above the Upper Flammability Limit (UFL). The low concentrations of one of the substances cause a too low number of reactant molecules to interact, and the processes stop. Reasons for this situation to occur, can be that there is too slow, or no, supply of fuel or oxidant.

However, in this section, a different extinguishing mechanism is treated. The case where the turbulent flow within a flame causes a blowout, is relevant for situations where there are e.g releases of gases from pressurized tanks or pipes. Even if the concentration of the reactants is between the LFL and the UFL in relatively large zones of the volume, the conditions may still be insufficient to sustain combustion.

An explanation can be found in the chemical kinetics of the reactants: A main reaction is the sum of thousands of elementary reactions. The specter of chemical time scales for the different elementary reactions can stretch wide, often more than 10 decades. The slowest reactions, e.g the formation of NO, can have a time scale of several seconds. The fastest have a time scale of 10^{-10} [1]. However, the time and length scales for the turbulence is only spread over a few decades, rarely more than 4-5 [9]. Molecular transport time scales can be shorter, so that the specter can be prolonged with a few decades. The time scales that dominate the transport, i.e large turbulent time scales, is often found within 2-3 decades. This means that chemical time scales often will be spread over a much wider specter than the turbulence transport.

A short reaction time scale, and a long transport scale, will cause a short lasting combustion, since reactants do not reach the reaction zone in time to sustain combustion. The opposite case, where a short transport scale is combined with a long reaction scale, a different mechanism is present. This is the mechanism present in figure 6.11. The conservation equation for each species will have to imply a chemical source term $M_i\omega_i$ [1]:

$$\frac{\partial(\rho w_i)}{\partial t} + div(\rho \overrightarrow{v} w_i) + div(\rho D \cdot grad\, w_i) = M_i \omega_i \tag{3.1}$$

where the source term is the sum of all chemical kinetic reactions that involve species i. The kinetic rates depend on other species, and have a nonlinear dependence on both species and temperature. Therefore it is unclear how to form the time average of equation 3.1. In principle, if the probability density functions for the mass fractions w_i are known, these equations can be averaged and solved. However, the computational limits are rapidly exceeded as the number of species increase [1].

As the mixing rate increases, one chemical process will emerge at first to depart from chemical equilibrium. Increasing the mixing rate further will result in another process departing from equilibrium. One by one, processes will depart from equilibrium until the main energy releasing reactions are competing with the mixing rate. As the mixing rate increases further, the temperature begins to depart from the equilibrium solution.

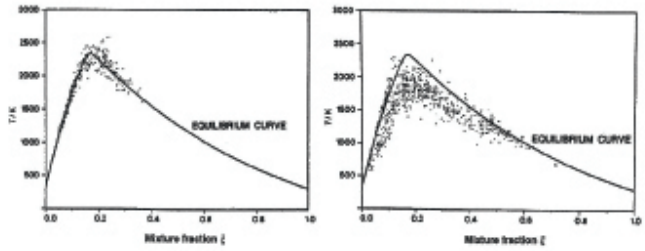

Figure 3.1: Laser Raman-scatter plots of simultaneous measurement of mixture fraction and temperature in a hydrogen turbulent non premixed jet flame where the jet velocity is increased by a factor of three going from the left drawing to the right; from [1]

An example is shown in figure 3.1 above. Moderate departure of temperature from chemical equilibrium is demonstrated. Left and right scatter plots are from the same flame except for a factor of three increase in hydrogen jet velocity on the right.

Both mixture fraction and temperature is measured by the Raman-scattering device. Each microsecond laser-pulse leads to a dot on the figure. As can be seen, the measurements group around the equilibrium line in the left figure. On the right, the fall in temperature shows that the mixing rate, which is movement from right to left on the x-axis, is competing with the heat-releasing chemical rates, which is vertical movements on these figures. The measurements are clearly below the equilibrium line. A further increase in jet velocity leads to a sudden global flame extinction [1].

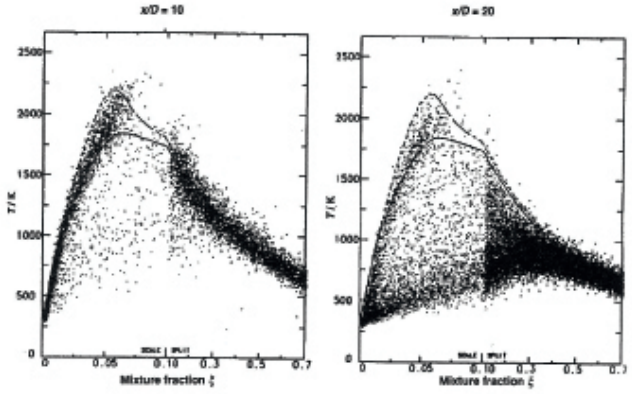

Figure 3.2: Laser Raman-scatter plots of simultaneous measurement of mixture fraction and temperature in a methane turbulent non premixed jet flame at different heights over the burner; from [1]; note the scale change on the ξ-axis

A different behavior is shown in figure 3.2. These scatter plots of mixture fraction and temperature show evidence of local flame extinction, internal to the flame. On the left, a methane flame at low mixing rates is shown. On the right is the same flame, but at a different location where air is rapidly mixing with the fuel. Local flame extinction is manifested by numerous data points being far from the equilibrium line. A further increase in jet velocity results in flame extinction.

Accordingly, a first-level improvement to the equilibrium model is to compute the rate of the first non equilibrium process of interest only, and to assume that the remaining (faster) processes are in equilibrium. This process will depart further from equilibrium as the mixing rate is increased. A parameter is needed that characterizes this departure.

Laminar opposed flows have solutions that increasingly depart from equilibrium as the mixing rate is increased, see [1], ch. 9 and fig. 3.4. The mixing rate is characterized by the scalar dissipation rate $\chi = 2D(grad\xi)^2$, which is related to the strain rate, a, by the equation ([10], [11]):

$$a = 2\pi D \left(\frac{grad\xi \cdot grad\xi}{(\xi^+ - \xi^-)^2} \right) \cdot exp2 \left\{ erf^{-1} \left(\frac{\xi - \frac{1}{2}(\xi^+ + \xi^-)}{\frac{1}{2}(\xi^+ - \xi^-)} \right) \right\}^2 \qquad (3.2)$$

This is an improvement of the strain rate approximation $a = 2V/R$, and it shows that, at any strain rate, the scalar dissipation can be large or small, if the difference between maximum ξ^+ and minimum ξ^- is large or small.

From this, a critical dissipation rate ξ_q, corresponding to a critical flow velocity, V, of the air, has been found by Tsuji and Yamaoka [1], for a laminar counterflow non premixed flame, as shown in figure, 3.3. f_w is a dimensionless outflow parameter, which can be calculated from the velocity V of the air, the

outflow velocity of the fuel v_w, the Reynolds number R_e, and the cylinder radius R.

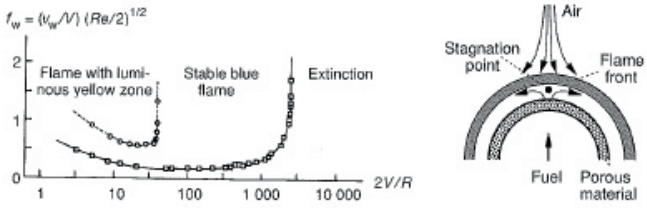

Figure 3.3: Stability diagram of a laminar counterflow diffusion flame measured by Tsuji and Yamaoka 1967, and burner configuration used; from [1]

Figure 3.4 shows calculated temperature profiles for some scalar dissipation rates χ in a counterflow premixed flame. The maximum flame temperature decreases with increasing scalar dissipation rate. For scalar dissipation rates larger than a critical χ_q (here $\chi_q = 20.6s^{-1}$; q stands for "quenching"), extinction is observed [1].

The temperature is dropping because the convective-diffusive heat removal rate is increasing, while, at the same time, the rate of heat generation is decreasing due to the reduced reaction rate and to the reduced residence time in the flame zone, causing an abrupt extinction.

The lift-off of turbulent flames which is shown in figure 3.5 can be explained by extinction due to scalar dissipation. The scalar dissipation is highest near the nozzle, where the scalar ξ takes on its maximum value ξ^+ and minimum value ξ^- and the strain rate is largest. Thus, extinction occurs at this location. The mean luminescent flame contour shows a lift-off, increasing with increasing jet velocity.

When modeling turbulent non premixed flames, extinction processes can be accounted for, if the integration over the scalar dissipation rates for the determination of the means of density, temperature, and mass fraction is only performed over the interval, where no extinction occurs [1], e.g:

$$\widetilde{T}(\overrightarrow{r}) = \int_0^1 \int_0^{\chi_q} T^{(F)}(\chi,\xi)\widetilde{P}(\chi,\xi;\overrightarrow{r})d\chi d\xi + \int_0^1 \int_{\chi_q}^{\infty} T_u(\chi,\xi)\widetilde{P}(\chi,\xi;\overrightarrow{r})d\chi d\xi \quad (3.3)$$

Extinction in non premixed flames is followed by local premixing of reactants. This leads to the very complex case of a partially premixed turbulent flame, where a further variable in the probability density function is needed to describe the degree of premixedness [1].

In the experimens carried out in this work, the combined effect of all these mechanisms has been recorded.

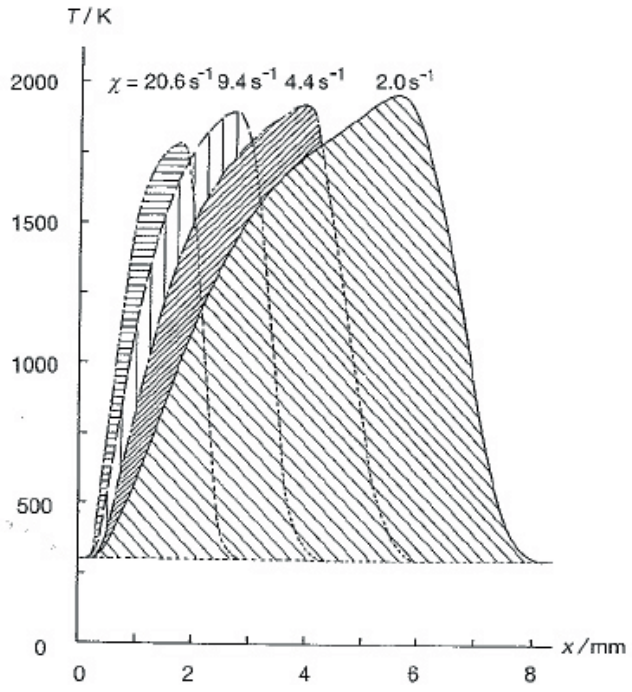

Figure 3.4: Calculated temperature profiles in a methane-air counterflow non premixed flame for different scalar dissipation rates χ; extinction occurs at $\chi > 20.6s^{-1}$; unburnt gas temperatures are $T = 298K$ on fuel and oxidizer side; $p = 1bar$; from [1]

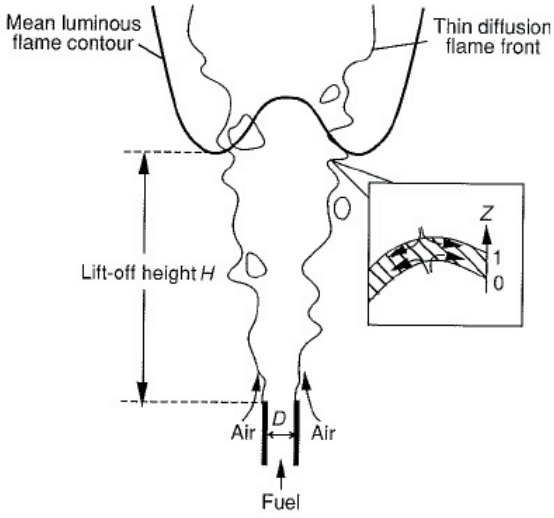

Figure 3.5: Schematic illustration of the lift-off behaviour of a turbulent jet non premixed flame; the inset box depicts how the laminar opposed-jet flame front is mapped into the turbulent flow field; from [1]

Chapter 4

Review of previous work

4.1 The Annushkin/Sverdlov Model

Annushkin and Sverdlov examined earlier studies of flame stability. These indicated limiting discharge velocities, denoted w_T^0, for which a fuel jet flame can undergo a stable combustion [3]. The limiting value grows nonlinearly with the nozzle diameter, d_c.

A thermochemical model showed that the standoff distance h from the nozzle to the the base of the lifted flame was determined by the homochronicity criterion $H_0 = \frac{w_T \tau_b}{d_c}$, where $\frac{d_c}{w_T}$ is proportional to the residence time of the mixture in the high-temperature boundary layer, and τ_b is a characteristic burning time of the mixture. It is assumed that for a constant value of τ_b, which is determined by the composition and temperature T_T of the fuel and the ambient temperature T_0 and pressure p_0, a limiting value H_0^0 of the homochronicity criterion exists, corresponding to blow-out of the flame. Here, $w_T^0 \propto d_c$.

Annushkin and Sverdlov showed that the assumption of a velocity $w_T > w_T^0$ resulted in a blow-out, is only correct up to a certain limit. They found that in the supersonic range (Mach no > 1) flame stability would be restored. Thus, for a given gas and d_c, at constant T_T, T_0 and p_0, there are two critical velocity limits, or relative pressure differences $\Delta\bar{p}_c$, defined as $\Delta\bar{p}_{c_1}$ and $\Delta\bar{p}_{c_2}$ (the bar sign denotes a relative dimensionless "measure"). In the interval between these ($\Delta\bar{p}_c = \Delta\bar{p}_{c_1} \rightarrow \Delta\bar{p}_{c_2}$) blow-out will occur. These intervals span from near zero up to several orders of magnitude, depending of the absolute nozzle diameter for a given fuel. In addition, it was found that if d_c was larger than a critical value, d_c^* for a given fuel, there will be a stable flame independent of $\Delta\bar{p}_c$.

Annushkin and Sverdlov devoted considerable attention to the restoration of flame stability in the supersonic domain of pressure differences. Convergent nozzles were used in order to obtain such flow rates. Here, the fuel is underexpanded after discharge. The expansion of the fuel up to a pressure equilibrium with the ambient will form a new diameter of isobaric cross section, d_T, and reduced discharge velocity λ_T. Note that Annushkin and Sverdlov do not differ between the terms discharge rate and discharge velocity. In the present work, only subsonic gas releases have been considered. However, the results from both sonic and subsonic gas releases are presented in figure 4.1, [3].

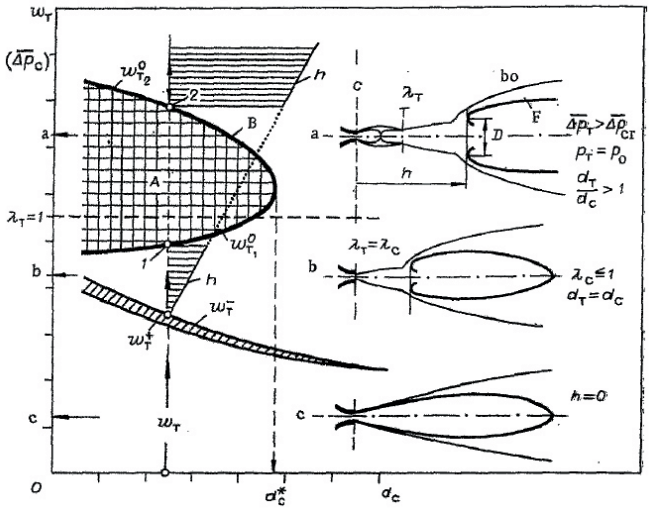

Figure 4.1: Qualitative configurations of flame instability domain (blowout in domain A) and flame bases for $\lambda_T > 1$ and $\lambda_T < 1$; T_0, p_0, T^*_T, L_0 are constant: 1) discharge rate at flame blowout with increase in w_T; 2) rate at restoration of flame stability in supersonic domain of $\overline{\Delta p}_c$ ($\lambda_T > 1$; $d_c > d^*_c$ domain of absolute flame stability for any λ_T ($\lambda_T \gtrless 1$); B) curve enveloping instability domain [3]

The work of Annushkin and Sverdlov gave the following conclusions, cited word by word [3]:

- The standoff distance of the stabilization ring of the base of a lifted flame increases along the surface of maximum velocity fluctuations, causing it to stand off from the surface of stoichiometric composition in the direction of lean fuel mixtures and finally resulting in extinction

- There is a limiting value of the injection nozzle diameter (determined by the fuel composition, ambient pressure, fuel temperature and ambient temperature), above which absolute stability of the lifted flame is ensured for any velocities

- A stability model has been proposed, along with analytical relations, making it possible to determine the domain of flame instability for subsonic and supersonic fuel streams discharging into a stationary surrounding air space

4.2 The Kalghatgi Model

Qualitatively, the Kalghatgi model describes the blow-out phenomenon similarly to the Annushkin/Sverdlov model. However, the Kalghatgi model is generalized for all gases, and the quantitative description differs considerably from the Annushkin/Sverdlov model, especially for propane. Kalghatgi provided a more thorough experimental verification for his predictions [4].

In a turbulent non premixed flame, the local turbulent burning velocity, S_t, will be equal to the local flow velocity, U. An increase in U will cause S_t to increase up to a point where lift-off occurs. A stable flame will occur where the local flow velocity has decreased, such that it is in balance with S_t. A further increase in U will cause the flame to blow out. This is the point where the change in S_t can not keep up with the change in U everywhere in the jet as one moves downstream from the base of the flame [4]. S_t varies with properties such as the kinematic viscosity and density of the fuel and the oxidizer, and the laminar burning velocity of the fuel.

Let H be the distance along the burner axis between the burner tip and the area where the fuel concentration drops to the stoichiometric level. It is very unlikely that the base of a stable lifted flame will be downstream of this point. H is independent of the burner exit velocity and is given by [12]:

$$H = \left[4 \frac{\bar{\theta}_e}{\bar{\theta}_s} (\frac{\rho_e}{\rho_\infty})^{1/2} - 5.8 \right] d_e \tag{4.1}$$

where d_e is the effective burner diameter, $\bar{\theta}_e$ is the fuel mass fraction at burner exit, $\bar{\theta}_s$ is the fuel mass fraction in the stoichiometric mixture of the fuel and the ambient gas, ρ_e is the the density of the burner gas at the burner exit, and ρ_∞ is the density of the ambient gas.

All other things being equal, the larger the value of H, the larger the scope will be for the base of the flame to establish a new stable position as the flow rate is increased, i.e the flame blow-out stability increases. Similarly, as the laminar burning velocity, S_u, increases for a gas or a compound of gases, the turbulent burning velocity, S_t, will increase and thus the blow-out stability will increase. In addition, S_t will depend on the local turbulence parameters and the fuel concentration [4]. These will in turn depend upon the kinematic viscosity, ν_e, of the fuel, and the ratio of densities, $(\frac{\rho_e}{\rho_\infty})$ at the exit plane. Therefore, it can be expected that U_e, the burner exit velocity at blow-out, to depend on H, S_u, ν_e, and $(\frac{\rho_e}{\rho_\infty})$. Dimensional analysis thus shows that [13]:

$$\frac{U_e}{S_u} = f\left(R_H, \frac{\rho_e}{\rho_\infty} \right) \tag{4.2}$$

where $R_H = (H \cdot \frac{S_u}{\nu_e})$ is the Reynolds number based on H.

Kalghatgi [4] determined this functional relationship by experiments carried out on a variety of pure fuels and mixtures of gases. A non-dimensional velocity,

$$\bar{U}_e = \frac{U_e}{S_u} \left(\frac{\rho_e}{\rho_\infty} \right)^{1.5} \tag{4.3}$$

was plotted against R_H, and the data collapsed onto a single curve given by:

$$\bar{U}_e = 0.017 R_H (1 - 3.5 \times 10^{-6} R_H) \tag{4.4}$$

This is Kalghatgi's 'universal' formula to describe the blow-out limit of non premixed jet flames.

The results are plotted in figure 4.2. The plot applies to $R_H < 75000$, and for nozzles of diameters in the range $0.2 - 12mm$.

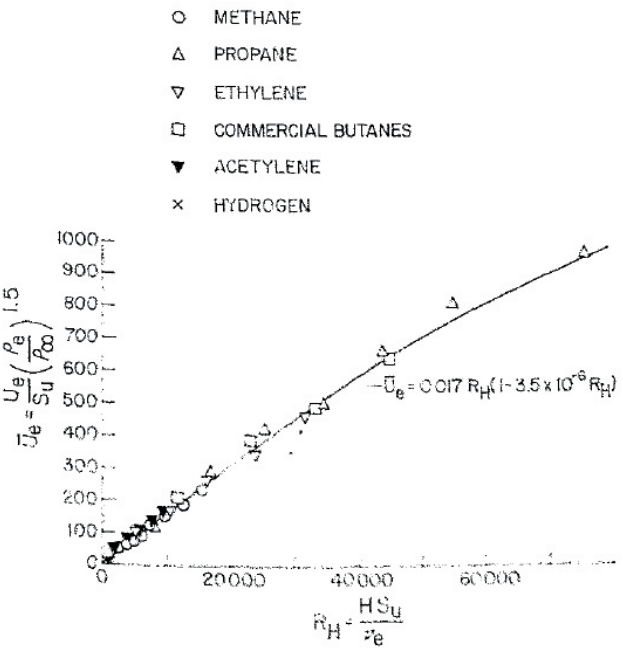

Figure 4.2: Kalghatgi´s universal blowout stability curve

Kalghatgi [4] conducted the experiments at subsonic releases, i.e for Mach numbers < 1. For supersonic releases, the results of Annushkin and Sverdlov [3] were used to extrapolate the results, by assuming an expanded diameter as shown by Annushkin and Sverdlov in figure 4.1.

The expanded diameter now indicated restoration of a stable flame above a certain limit, varying for the different outlet diameters, and even a critical diameter above which, a stable combustion will take place for any discharge rate, see figure 4.3.

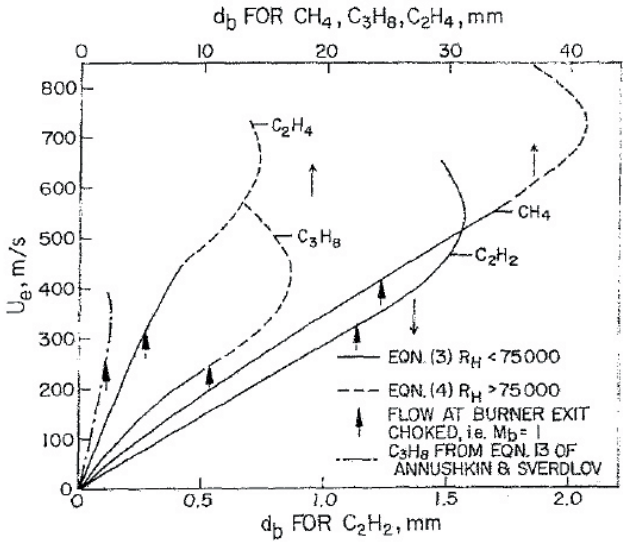

Figure 4.3: Kalghatgi´s extrapolation of the universal blowout stability curve. Note the critical outlet diameter for propane

Following up his findings, Kalghatgi also studied the effect of cross wind in a separate article [5]. This work resulted in non-dimensional stability curves for different gases, and for different outlet diameters. His main findings were:

- For a given burner and a given gas, if the cross-wind speed is greater than a limiting value, a stable flame is not possible

- For cross-wind speeds < the limiting value above, there are normally an upper and a lower blowout limit

- In the lower limit, the flame will be extinguished at a flow rate through the burner that is much less than that in the absence of cross-wind. However, in the wake of the burner, the flame in some cases gets stabilized, and cannot be blown out, even if the discharge rate approaches zero

- A stable, lifted bent-over flame can be sustained over the burner if the flow rate is between the lower and the upper blowout limit. The upper blowout limit is higher when a cross-wind is present than for still air. This is indicated by Kalghatgi as being a function of the larger turbulence intensity in a cross-wind situation. Hence, the turbulent burning velocity can be expected to be larger in the jet in a moderate cross-wind, and the flame can be expected to be more stable [5]

4.3 Recent research

The main part of the experiments reported in this thesis, were carried out in the period 2001-2003. After this work was done, a series of articles have been presented by Lyons et.al (2005) [14], Kronenburg (2005) [15], Su et.al (2006) [16], Chih-Yung et.al (2006) [17], Wang et.al (2007) [18], Hermanns et.al (2007) [19], Leung (2009) [20] and Kaiser (2009) [21].

A common aim for these scientists has been to describe and quantify the blowout mechanisms at a more fundamental level than their predecessors. A few examples are presented below, to show the direction this research is currently taking.

Lyons et.al [14] discussed the generation of flame holes and local extinction in a methane/air diffusion flame. This was done by means of sequential CH-PLIF method. This means that sequences of planar laser-induced fluorescence images were recorded for the CH radical. Examples are shown in figure 4.4. Local extinction can result from large strain imposed on the reaction zone by the flow field which inhibits the fuel burning rate, thereby causing the Damköhler number to drop below a critical extinction value. There are several Damköhler numbers, and in this case it is defined as:

$$Da = \frac{\text{reaction rate}}{\text{convective mass transport rate}}$$

This means that if the strain rate for the flow, related to the convective mass transport rate in the definition above, becomes too large compared to the reaction rate for the CH radical, the Damköhler number drops, and local extinction may occur. For very high strain rates, global extinction can occur.

As can be seen in figure 4.4, the local extinction occurs at the farthest radial location along the flame contour, and often coincides with the apex of a radial bulge. A more detailed description is presented in the two dimensional PIV velocity (Particle Image Velocimetry) field in figure 4.5. Based on the sequential imaging, it is possible to generate velocity vectors for the flow. Strain rates calculated from these velocity vectors are presented in figure 4.6.

Lyons et.al [14] registered that, once a flame hole has been established, no occasions were witnessed of a flame hole mending, only flame hole growth. It is pointed out that higher dissipation rates are required for quenching than those necessary to contribute to flame hole growth. While scalar dissipation measurements are extremely difficult in the presence of PIV particles, the result of their study implied that hole inception may be represented by the the critical dissipation rate, while hole growth results from maintenance of the smaller (relatively) dissipation rate. Finally, bulges in the CH profile move both radially outward and downstream. While actual extinction is not witnessed in the figures presented, it can be envisioned that these bulges are precursors to local flame extinction [14].

Using this method, it should be possible to move towards blowout models based on the Damköhler numbers. But it will still be a long way to go in order to make a truly fundamental model, considering the vast number of different radicals present in a combustion in addition to the complex flow and thermochemical characteristics.

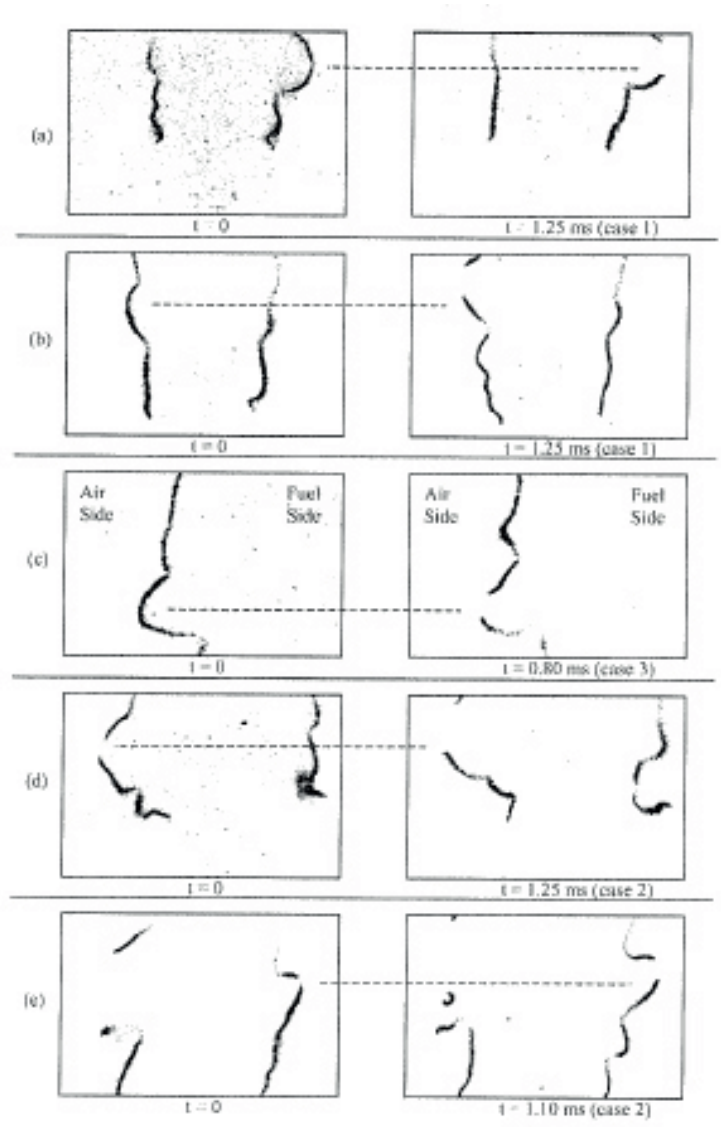

Figure 4.4: Sequential CH-PLIF images showing the development of local flame extinction. The case number listed for each image pair (1, 2 or 3) corresponds to $Re_d = 4800, 6500, or 8300$. *The images represent a* $37.4mm$ *wide* $\times$ $24.9mm$ *high region of the flow, from Lyons et.al [14]*

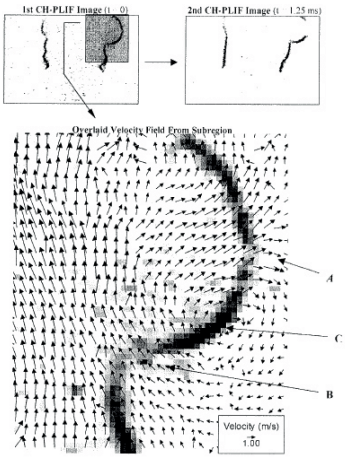

Figure 4.5: Two dimensional PIV velocity field from the indicated subregion of the first sequential CH-PLIF image shown above. Note that the two PIV pulses are centered about the first CH-PLIF pulse. This is from the $Re_d = 4800$ flow condition. The subregion showing the velocity field represents a $9.9mm$ wide $\times$ $11.9mm$ high region of the flow, from Lyons et.al [14]

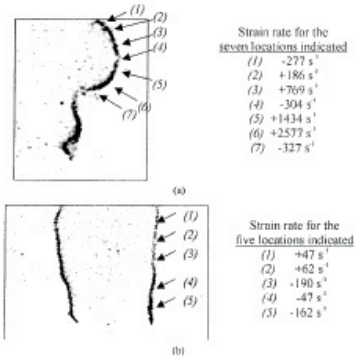

Figure 4.6: Values of the strain rate calculated from the velocity fields are shown for (a) a case with a bulge leading to local extinction, see figure 4.5, and (b) an intact, stream-wise linear reaction zone. They are calculated along the CH contour at positions indicated by the arrows. Values on the strain rate on points along the CH contour reach values much higher in (a) than (b), from Lyons et.al [14]

Su et.al focus on the upstream end of the flame in their work [16]. They found that the flame stabilization process may preferentially seek points further from the centerline because flow velocities are likely to be lower there. The mean leading points, see figure 4.7, were found to be inside the $u = S_L$ contours. The leading points are defined to be the most upstream points at the instantaneous high-temperature interface. Here, u is the mean axial flow velocity, and S_L is the stoichiometric laminar flame speed. At the leading points, the actual u was found to be $\approx 1.8S_L$. This compares with centerline mean velocities in excess of $15S_L$. Figure 4.8 shows the proposed simple model for the dynamics of the flame base motion, based on the large scale organization of the mixing field, and the tendency of the flame to stabilize in regions of relatively low axial velocities.

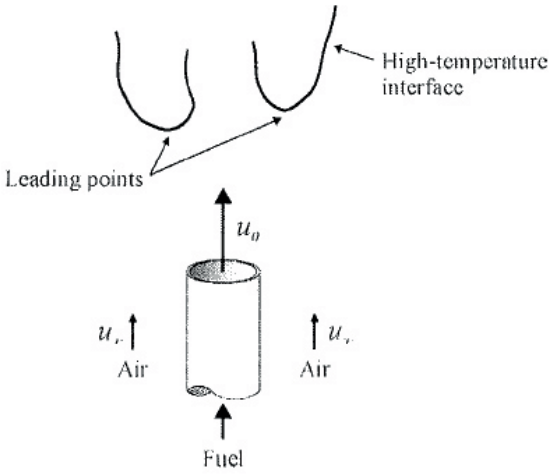

Figure 4.7: A schematic of the lifted, co-flowing jet diffusion flame. The high-temperature interface (the figure depicts a two-dimensional section of the interface) is marked by large temperature gradients between the unburned gases and the hot combustion products. This interface may, but does not necessarily, mark the actual flame location. The leading points are defined as the most upstream positions on the high-temperature interface, on each side of the jet centerline, from Su et.al [16]

With reference to figure 4.8, the dynamics is explained by Su et.al [16]:

Suppose that the stabilization point is initially relatively far from the the centre line (figure 4.8a). The axial velocity at this extreme radial location is likely to be lower than the mean flame speed, so that the stabilization point advances upstream. This requires the stabilization point to move radially inward in order to maintain a flammable fuel mole fraction, because the scalar profile is narrower upstream. Moving upstream and toward the centre line also causes

the axial flow velocity to increase; eventually, the stabilization point begins to recede downstream (figure 4.8b). A new coherent structure then overtakes the flame. This structure brings a stepwise increase in the fuel mole fraction, and the stabilization point moves radially outward, toward flammable mixtures (figure 4.8c). Together, the downstream and outward motions result in a decreasing axial flow velocity, eventually causing the stabilization point to advance upstream (figure 4.8d), until the initial situation recurs (figure 4.8e). This description emphasizes the primary role of the large-scale flow organization; small scale fluctuations and turbulence are higher-order effects.

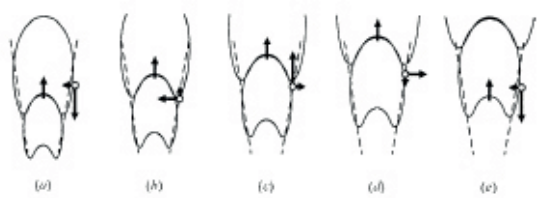

Figure 4.8: Schematic depiction of the flame base motion, in terms of the axisymmetric mode of large scale organization of the mixing field. Time advances from left to right. The instantaneous stabilization point for each time is represented by a gray circle. In (a), the stabilization point is relatively far from the centre line, and the flame advances upstream against the low axial flow velocity. This simultaneously requires that the flame move radially inward, to maintain a flammable mixture. Eventually, the local axial flow velocity becomes sufficiently high that the flame begins to recede downstream (b). When the trailing coherent structure, which brings higher fuel mole fractions, overtakes the flame, the stabilization point moves radially outward (c). As the flame moves downstream and outward, the flow axial velocity decreases, until the flame once again propagates upstream (d) and the initial situation recurs (e), from Su et.al [16]

Chapter 5

Experimental apparatus and procedure

5.1 Experimental apparatus

A rig consisting of a $14m^3$ gas tank, a pump and a gas evaporator to convert propane from liquid to gas phase was used as a fire source. The propane was led through a system of stainless steel pipes. This was the same setup as for the flame characterization experiments explained in Part I. But in the case considered here, there were no thermocouples, radiometers, steel cylinder or other obstructions in the flow field. Two sets of pilot burners were used. They are shown in figure 5.1. The flame in the background is from the primary pilot of the system. This was used in the start of each experiment, for a rough stabilization of the flow before the actual experiment was carried out. A three way valve was fitted, in order to lead the gas flow over to the test nozzle. The secondary pilot burners were used for establishing a new stabilization after redirecting the flow, but before the actual testing of the blowout stability. During the experiments, a meter was used for recording wind speed, temperature and humidity. The wind direction was recorded by means of a narrow strip of cloth hanging on the test rig. At the rig, a flow meter and two manometers were mounted, in order to assess the flow and the pressure losses through the nozzles.

7 different cylindrical nozzles with circular cross sections of diameters $4, 6, 8, 10, 12, 14$ and $16mm$ were used for experiments on varying gas flow conditions. Each nozzle had a length, $L \geq 10\times$nozzle dia. to ensure a fully developed flow at the outlet.

In order to establish flows at different inclinations, a hinged system was built, see figure 6.4(b) for details.

Figure 5.1: Main parts of the test system. Note the flame in the primary burner used for a rough stabilization of the flow. The valve being operated was for leading the flow over to the test nozzle in the centre of the picture. The pilot burners at the right was for establishing a new, stable flow after the redirection, but before the actual test of the blowout stability was carried out

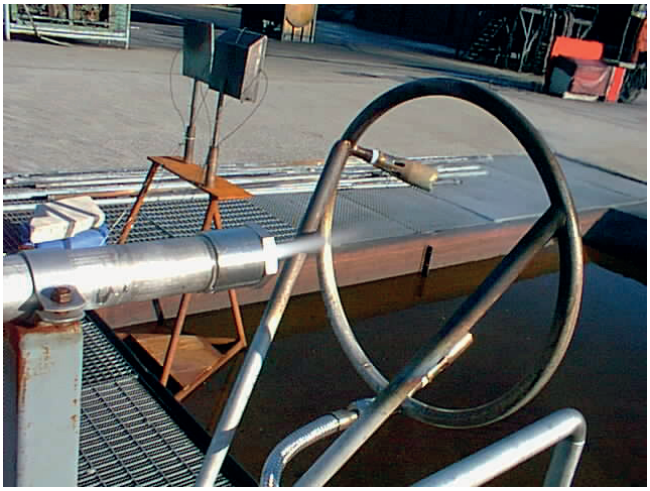

Figure 5.2: Example of flow through the nozzle, without gas ignition. Note the visible vortices that were formed close to the tip of the nozzle

Figure 5.3: The gas flow after ignition. The combustion was sustained by the help of pilot burners. Note the blue ring by the tip of the pilot burners. The gas was released by opening a valve between the tank and the nozzles, without any form of pressure increasing devices. Therefore, the driving pressure for the pilot burners was normally in the range $7 - 8barg$*, depending on the propane temperature in the tank*

5.2 Experimental procedure

The complex design, the parts, and the assembly of the test setup were subject to a thorough validation of the functionality of the complete system before starting any experimental activities. In one sense, the safety measures taken, were slightly overkill. This was in the form of a water cooler connected to the ethanol circuit for the evaporator. This turned out to be unnecessary, and the water supply was shut. On the other hand, the nozzles on the secondary pilot burners were subject to high thermal loads, and were easily damaged. Therefore, visual inspections were frequently carried out, and new nozzles were mounted when the existing were in unsatisfactory condition.

Each experiment started by placing a multi meter near the test area, before opening and ignition of the flow for the primary pilot burner. Then, in turn, the burner for the evaporator was ignited, the secondary pilot burner was ignited, and the valve for the experimental gas flow was opened. The pump for the propane in liquid phase was started. The pump was placed between the tank and the evaporator, and caused an increased flow and pressure of propane into the evaporator. When the flow had responded to the increased pressure and stabilized, it was led from the primary pilot burners over to the test nozzle and secondary pilot burners. Due to the change in pipe length and number of bends, a few more seconds was needed for the flow to stabilize again.

Following the final stabilization, the secondary pilot burners were shut, and a stop watch was started. The experimental gas flow was stopped when a blowout

occurred, or when a continuous combustion had lasted for 30 seconds, whichever came first. The tests were carried out on outlets forming an angle to the vertical of $0^0, 45^0$ and 90^0.

A total of 195 separate experiments were carried out. For each experiment, the following information was collected:

- nozzle diameter
- outlet direction
- gas flow rate
- gas pressure upstream of nozzle (P1)
- gas temperature upstream of nozzle
- gas pressure downstream of evaporator (P2)
- wind speed
- wind direction
- relative humidity
- air temperature
- date
- time
- comments on execution of experiment
- comments on weather conditions
- blowout/no blowout

See Appendix A for detailed records.

For approximately the first 100 experiments, a complete shutdown of the system was carried out after logging blowout/no blowout. The procedure was very close to a reversed startup procedure, as explained above. For safety, detailed written procedures were followed, both for starting and stopping the experiments.

After gaining more experience, an SJA (Safe Job Analysis) was carried out, and a revised procedure was followed. The startup was the same for each series of experiments, but instead of closing down completely, the gas flow was led to the primary pilot burners at the end of the experiment without being shut. Then, the flow was altered, and it was led back through the experimental nozzle. A new experiment was carried out, and the procedure repeated. However, for each change of nozzle or change of outlet direction, a complete shutdown was carried out.

Chapter 6

Results

6.1 Direction of outlet - the influence on blowout

The first study consisted of finding out if the direction of the outlet would influence the blowout characteristics of the gas jet flame. In the following subsections, the results for vertical, 45^0 inclination and horizontal outlets, are presented. All experiments were carried out in calm wind conditions, and therefore it was expected that any differences in blowout characteristics would be caused by gravity, or light wind in the low momentum region of the gas flow. The light wind conditions were, in other words, not expected to have a significant influence near the outlet.

A large number of experiments were carried out for each outlet direction, which gave a high confidence in the results. For the vertical release, 54 experiments were performed. For the 45^0 inclination and the horizontal outlets, 67 and 74 experiments were carried out respectively.

In general, the distance from the outlet to the far end of the flame, differed very little for the different flows for a given nozzle. However the liftoff, i.e the distance from the outlet to the near end of the flame, increased with increasing flow. This was discovered too far into the experimental program, and therefore, this effect was not measured.

One feature was very clear for all situations near a blowout: The flame got optically thinner and thinner before blowout occurred. In some cases, the flame was hardly visible for the human eye. The accurate confirmation of a blowout, was in the form of an abrupt change in the sound from the jet, taking place in less than $0.5s$.

6.1.1 Vertical release

The plot shows indications of lower blowout limits for circular outlets in the range $4 - 10mm$, both upper and lower blowout limits for a $12mm$ outlet, and no blowout limits for outlets in the range $14 - 16mm$.

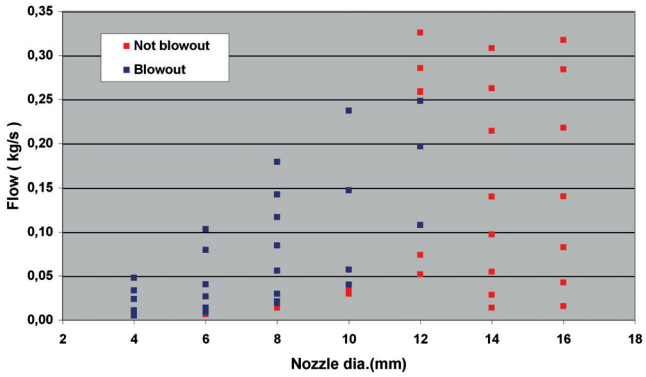

Figure 6.1: Registrations of each of the 54 individual experiments for vertical releases. The plot shows indications of lower blowout limits for circular outlets in the range $4 - 10mm$*, both upper and lower blowout limits for a* $12mm$ *outlet, and no blowout limits for outlets in the range* $14 - 16mm$

(a) (b)

Figure 6.2: (a) experimental setup for release of vertical propane jet. Note that the pilot burner at the top of the image was not used in the blowout experiments. (b) flame very close to blow-out, note the large lift-off and the optically very thin flames

6.1.2 45^0 release

The plot shows indications of always blowout for circular outlets of size $4mm$, a lower blowout limit for $6mm$ outlets, possible upper and lower blowout limits for $8-14mm$ outlets, and no blowout limits for outlets of $16mm$ diameter.

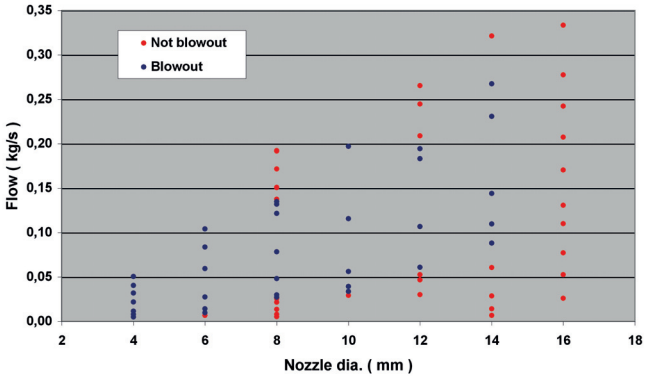

Figure 6.3: Registrations of each each of the 67 individual experiments for 45^0 releases. The plot shows indications of always blowout for circular outlets of size $4mm$, a lower blowout limit for $6mm$ outlets, possible upper and lower blowout limits for $8-14mm$ outlets, and no blowout limits for outlets of $16mm$ diameter

(a) (b)

Figure 6.4: Two experiments with 45^0 inclination, showing (a) an optically thin flame, small lift-off, and (b) an optically thicker flame with a larger lift-off. The optical thickness increase with increasing nozzle diameter and decreasing pressure loss over the nozzle. The lift-off distance increases with a decreasing nozzle diameter and an increasing pressure

6.1.3 Horizontal release

The plot shows indications of always blowout for circular outlets of size $4mm$, a lower blowout limit for $6mm$ outlets, possible upper and lower blowout limits for $8-12mm$ outlets, and no blowout limits for outlets of $14-16mm$ diameter.

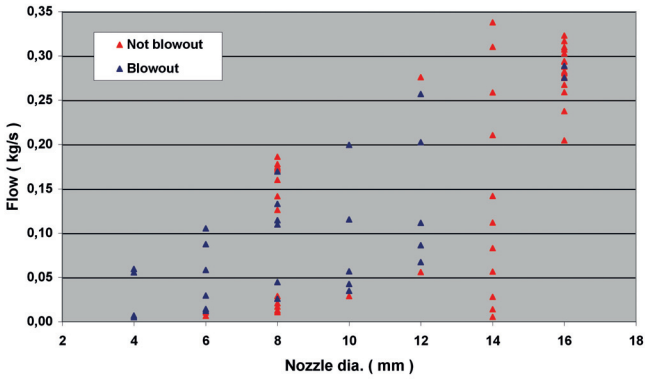

Figure 6.5: Registrations of each each of the 74 individual experiments for horizontal releases. The plot shows indications of always blowout for circular outlets of size 4mm, a lower blowout limit for 6mm outlets, possible upper and lower blowout limits for $8-12mm$ outlets, and no blowout limits for outlets of $14-16mm$ diameter

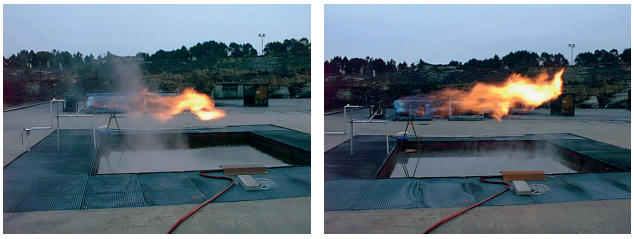

(a) (b)

Figure 6.6: (a) experiment 4, flow 1, 6mm nozzle, and (b) experiment 3, flow 1, 16mm nozzle

6.1.4 All experiments combined

Although the results for the different inclinations differ slightly, there seems to be no systematic difference between them. Compared to the variation in results *within* each inclination, the variation *between* the inclinations are similar. Therefore, the results for all inclinations are treated as one single set of experiments from here on. The plot shows indications of always blowout for circular outlets of size $4mm$, a lower blowout limit for $6mm$ outlets, possible upper and lower blowout limits for $8-14mm$ outlets, and no blowout limits for outlets of $16mm$ diameter.

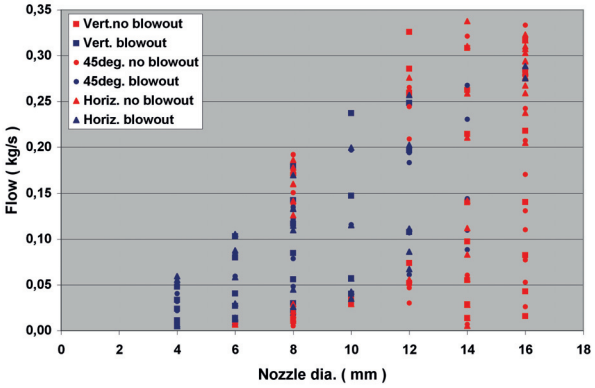

Figure 6.7: Registrations of each individual experiment for all 195 releases. The plot shows indications of always blowout for circular outlets of size $4mm$*, a lower blowout limit for* $6mm$ *outlets, possible upper and lower blowout limits for* $8-14mm$ *outlets, and no blowout limits for outlets of* $16mm$ *diameter*

Figure 6.7 forms the basis for the blowout model presented in section 6.3. The choice of nozzles has hit a range of diameters for propane jet flows that span from outlets where there will *always* be blowout ($4mm$) to the case where a blowout *never* will occur ($16mm$) within the flow rates. These results have been extrapolated outside the ranges of the experimental outlet diameters and flows in the blowout model. The reason why this has been done, is discussed in chapter 7.

6.2 Connection between the different variables

The gas flow rates varied in the range $0.005 - 0.338 kg/s$, corresponding to heat release rates of the fires in the range $0.2 - 16.3 MW$, assuming an average heat of combustion of $48.35 MJ/kg$. The pressure drop across the nozzles were $0 - 16.5 barg$ $(0 - 1650 kPa)$.

For the 195 separate experiments, the measured pressure upstream of the nozzle versus the flow were plotted into a diagram. The results are shown in figure 6.8. Note that in the plots, the results for all inclinations of a nozzle have been plotted into the same curve. Different inclinations of the flow outlet was examined in order to find out if the blowout mechanism would vary with this inclination. No results indicated a functional relationship between outlet inclination and blowout, see subsection 6.1.4 for more information. This result is best illustrated in figures 6.1, 6.3, 6.5 and 6.7. Also, for a given nozzle, the single points in the diagram in figure 6.8 show no significant variations in deviations for the different inclinations.

The results for the $10mm$ nozzle showed larger deviations than the other nozzles for all inclinations at the high pressure end. There were both larger and smaller diameter nozzles showing less deviations than the $10mm$ nozzle. No explanation was found for this.

Since no functional relationship between inclination and blowout was evident, the results were treated accordingly, i.e no distinctions were made in figure 6.8 or in the final empirical blowout model presented in section 6.3. This blowout model is shown as upper and lower blowout limits as function of flow through a nozzle of a given diameter, see section 6.3.

In order to make the model more available for designers, engineers, risk management personnel etc, a table of results have been presented in subsection 6.3.3. It is assumed that this table is easier for practical applications, because it predicts blowout limits for a given nozzle for varying, easily measured *pressures* rather than flows. The reason for not converting this into a second model, is that it would not be possible to make a perfect curve fit with the original model. Thus, this could cause opposite blowout predictions for pressures in narrow bands close to the blowout limits.

Regardless of blowout or no blowout of an ignited gas flow, there was a linear relationship between pressure immediately upstream of, and flow through, the nozzle. Due to small fluctuations in the flow meter readings, and uncertainties in the flow meter and the manometer readings, the single points only emerged into near straight lines for the seven nozzles. Therefore, straight lines, based on least squares of deviations, were plotted, and the equations for these lines are shown below.

The equations for the straight lines in the diagram were found by making a routine in MatLab for finding the least squares linear curve fit as shown below. One set of equations was made for each nozzle diameter. The matrix P_i represent the pressures in each experiment, and similarly, Q_i is the flow. Vector x represents the inclination of the straight line, and the intersection with the y-axis respectively:

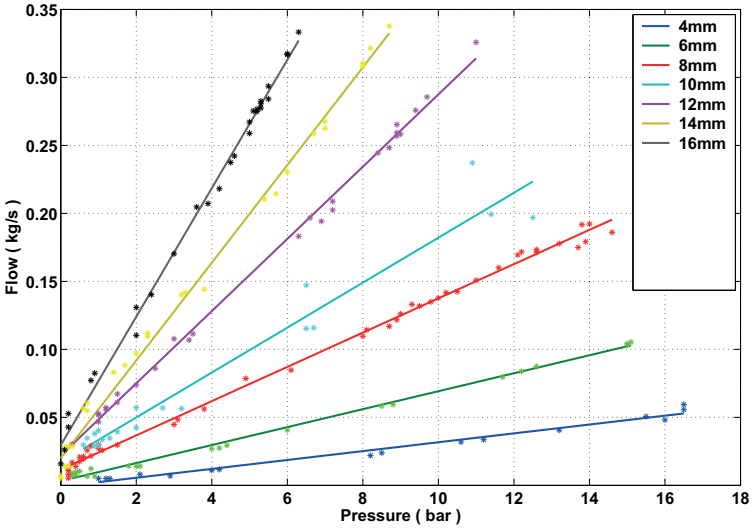

Figure 6.8: Curves showing the logged flow vs pressure for the seven different nozzles. The coloured legends denote the nozzle diameter. Each of the 195 experiments are represented by a point in the figure. The method of least squares has been applied for producing the straight lines representing each nozzle. Note that no separation between the different inclinations for each nozzle has been made. See section 6.2 and subsection 6.1.4 for more information. The pressure is in barg

$$P_i = \begin{bmatrix} P_1 & 1 \\ P_2 & 1 \\ \dots & \dots \\ \dots & \dots \\ P_n & 1 \end{bmatrix}, \qquad Q_i = \begin{bmatrix} Q_1 \\ Q_2 \\ \dots \\ \dots \\ Q_n \end{bmatrix} \quad \text{and} \quad x = \begin{bmatrix} m \\ c \end{bmatrix}$$

The MatLab routine was written for minimizing the squares of the deviation from a straight line, i.e this solution was sought:

$$\|Px - Q\|^2_{min}$$

where

$$\|Px - Q\|^2 = \sum_{i=1}^{n} [(mP_i + c) - Q_i]^2$$

Flow, Q is measured in kg/s. The subscript denotes the nozzle diameter. Pressure, p, is measured in $barg$:

$$Q_4 = 3.26 \times 10^{-3} p - 9.26 \times 10^{-4} \quad (6.1)$$
$$Q_6 = 6.61 \times 10^{-3} p + 3.18 \times 10^{-3} \quad (6.2)$$
$$Q_8 = 1.26 \times 10^{-2} p + 1.16 \times 10^{-2} \quad (6.3)$$
$$Q_{10} = 1.65 \times 10^{-2} p + 1.69 \times 10^{-2} \quad (6.4)$$
$$Q_{12} = 2.66 \times 10^{-2} p + 2.19 \times 10^{-2} \quad (6.5)$$
$$Q_{14} = 3.59 \times 10^{-2} p + 2.00 \times 10^{-2} \quad (6.6)$$
$$Q_{16} = 4.72 \times 10^{-2} p + 2.96 \times 10^{-2} \quad (6.7)$$

One can see from the equations that for the $4mm$ nozzle, there is a small negative flow when $p = 0$. The largest flow for $p = 0$ is found for the $16mm$ nozzle. This value is $Q = 0.0296kg/s$. All points fit fairly well into a line, except for the $10mm$ nozzle, where the experiments show more scattered results.

6.3 The blowout model

Based on the results for all experiments, as presented in figure 6.7, points were chosen to represent upper and/or lower blowout limits for each nozzle diameter. Care was taken, in order to choose limits that returned the largest number of correct predictions compared to the experiment. Following the choice of points lying on the two limits, a set of trial and error was carried out in order to get a suitable curve fit. The results are presented in equations 6.8.

No model consisting of one cohesive line representing the *lower* blowout limit, and another cohesive line representing the *upper* blowout limit, will give a larger number of correct predictions than the one presented here. See subsection 6.3.4 for a more detailed documentation. The actual prediction accuracy is also presented in the same subsection.

6.3.1 Generation of the model

The model was generated by applying a best curve fit to a set of points decided by the experiments. Step by step, this was obtained by:

Experiments: 195 experiments were carried out for varying gas flows and nozzle diameters. This resulted in the diagram, figure 6.7.

Choice of points at the curve: For each nozzle type, an investigation was carried out in the diagram. First, a check for possible upper and lower blowout limits was carried out. For nozzle diameter $4mm$, blowout occurred for all experiments. Thus, no blowout limits were found for this nozzle. The same procedure was applied to all nozzles, and e.g for the $8mm$ dia. nozzle, the lower blowout limit was found by checking point for point for an increasing flow. For the smallest flow, no blowout occurred. Moving upwards for this nozzle, a zone with a mixture of blowout/no blowout occur for an increasing flow. For the point where an increased flow would add more "blowouts" than "no blowouts",

the lower blowout limit was assumed to be reached. By doing this for the upper and lower limits for all nozzles, a set of points on the two curves were obtained.

Curve intervals: At this stage a set of points on the curves $Q_u = f_u(d)$ and $Q_l = f_l(d)$ (u and l denoting the upper and lower limits) had been established. However, single functions describing these relationships over the whole range of diameters were not found, and suitable intervals were chosen. An example of a suitable interval, is the second, for nozzle diameters 5 to $10mm$, see figure 6.11. In this range, the upper blowout limit was shaped like a simple polynomial, making the task of curve fitting easier. Care was taken, so that the upper and lower blowout limits could be made for the same intervals, making the presentation of the model short and concise.

Curve fit: No more than three nozzle diameters were involved in each interval. This made the task of curve fitting easy. Using the lower blowout limit for nozzles of diameters $10 \leq d < 14$ as an example:

In this case, the flow for the lower blowout limits for nozzle diameters 10 - $14mm$ was already established from the "choice of points", see above. The curve has got the shape of a polynomial of the general form $y = ax^n$. It applies for diameters of $10, 12$ and $14mm$, and the expression for the limit, is:

$$Q_l = 0.039\left(\frac{d}{10}\right)^{(1.508d-15.827)}$$

By choosing $x = d/10$, it follows that for $d = 10$, it does not matter what the value for n is. Therefore, for this diameter, $a =$ the flow. At this stage, only two diameters remained, the 12 and the $14mm$ nozzles. The general equation to solve for these two equations, were $y_1 = ax_1^n$ and $y_2 = ax_2^n$, where all variables were known, except n. Trial and error produced the solution $n = 1.508d-15.827$.

Similar processes were carried out for all intervals, where d was the only allowed independent variable, upper and lower limits were made for the same intervals, and the end of one curve was attempted to be shaped so that it would run smoothly into the start of the next.

Result: The result of this process is presented in the boxed set of equations 6.8.

6.3.2 Blowout flow as a function of outlet diameter

In order to get the best possible prediction, stepwise functional relationships between flow at blowout, and outlet diameters were found to be the most practical approach. The model predicts that for outlets of diameter less than $5mm$, it is not possible to sustain a stable, continuous combustion without the help from e.g pilot burners. At the other end of the scale, once ignited, a combustion will not extinguish by itself if the diameter of the outlet exceeds $14mm$. In the intermediate range, i.e diameters between 5 and $14mm$, both upper and lower blowout limits exist. In this case, the magnitude of the flow will determine whether an ignited gas will undergo a sustainable combustion, or extinguish.

For each experiment, both the flow and the pressure was recorded. The reason for choosing flow in the model, was due to the instrumentation. The manometers only acted as rough indicators, whereas the flow meter was more accurate:

Blowout flow model for circular outlets of propane in gas phase. Q is measured in kg/s and d is measured in mm. The model predicts a critical diameter of 14mm:

$$\begin{aligned} & & & \textit{for } d < 5 \textit{ , always blowout} & \\ 0.0083(d-5) & \leq Q & < 0.05|d-8|^{1.200} + 0.036 & \textit{for } 5 \leq d < 10 & \\ 0.039\left(\frac{d}{10}\right)^{(1.508d-15.827)} & \leq Q & < 1.25 - \left(\frac{d}{10}\right)^{(0.050d-0.644)} & \textit{for } 10 \leq d < 14 & \\ & & & \textit{for } d > 14 \textit{ , never blowout} & (6.8) \end{aligned}$$

For visualization, and quick reference, a plot of the model has been made in figure 6.9. This clearly shows the tendency for an ignited propane jet flame arising from a small diameter circular outlet, to blow out. However, in a field around $8mm$ diameter, the band where blowout will occur is narrow. On both sides of this diameter, a wider band shows the presence of a more unstable flame. A discussion of this is presented in section 7.3. It was not possible to obtain large flows for the small diameter nozzles. Therefore, the upper blowout limits for the small diameter nozzles are not as well backed up experimentally as for the rest of the experiments.

With very few exceptions, blowout did not occur for nozzle diameters $14mm$ and above:

6.3.3 Blowout pressure as a function of outlet diameter

For practical reasons, a presentation of the blowout pressure limits based on the easily measured, or estimated, pressure and outlet diameter has been made in table 6.1.

The pressures at the blowout limit have been calculated using the pressure-flow relationship in figure 6.8, rather than the actual measured pressure from the experiment. For nozzle diameters different from the ones used in the experiments, interpolations have been made. A tabular presentation has been made, rather than a functional relationship. The reasons for these choices are thoroughly discussed in chapter 7. A plot of the numbers in this table is presented in figure 6.10.

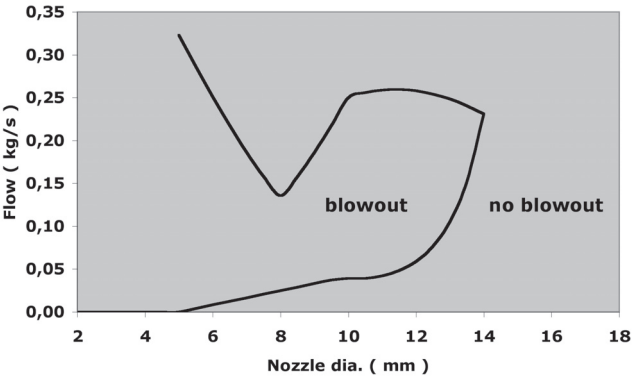

Figure 6.9: A plot of the blowout model presented in equations 6.8. The empirical model is made as a best fit compared to all the 195 separate experiments carried out. Note the narrow blowout band around the 8mm nozzle. Also note that the model predicts blowout for all flows when the outlet diameter is less than 5mm, and that blowout will not occur for outlet diameters larger than 14mm

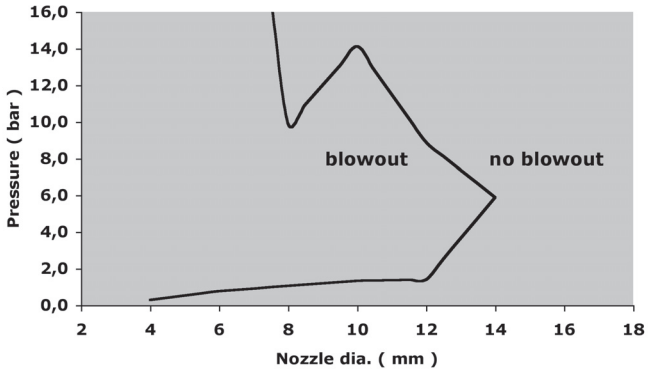

Figure 6.10: Plot of blowout pressure limits using outlet diameter as input. The values in table 6.1 have been used in the plot. Note the similarity to figure 6.9 in the shape of the plot

Table 6.1: Table of blowout pressure limits as function of outlet diameter. The values in the table were derived from the blowout model, equation 6.8. The flow values from the model have been used as input in equations 6.1-6.7, to find the pressures corresponding to these flow values. Interpolations have been made for intermediate cases between each nozzle diameter

Nozzle dimension (dia. in mm)	Blowout region (pressure in barg)
4.0	> 0.3
4.5	> 0.4
5.0	> 0.5
5.5	> 0.7
6.0	0.8 - 37.4
6.5	0.8 - 30.5
7.0	0.9 - 23.6
7.5	1.0 - 16.8
8.0	1.1 - 9.9
8.5	1.1 - 10.9
9.0	1.2 - 12.0
9.5	1.3 - 13.1
10.0	1.3 - 14.1
10.5	1.4 - 12.8
11.0	1.4 - 11.5
11.5	1.4 - 10.2
12.0	1.4 - 8.9
12.5	2.5 - 8.1
13.0	3.6 - 7.4
13.5	4.8 - 6.6
14.0	5.9
> 14.0	no blowout

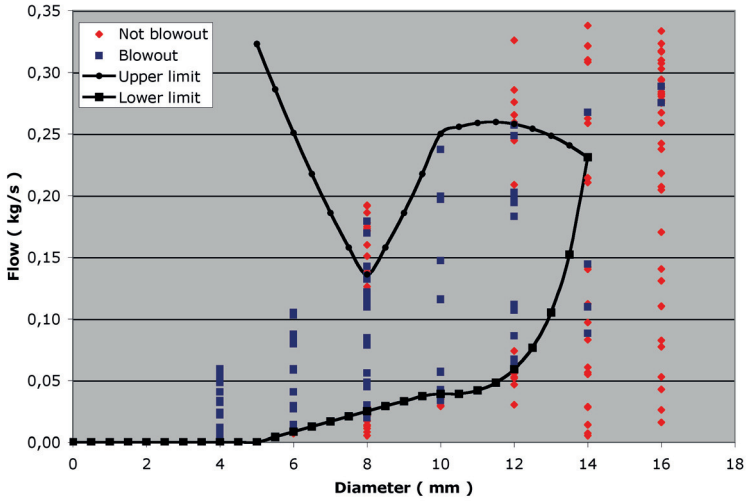

Figure 6.11: A combined plot of the experimental data, shown as single points, and the blowout model, shown as coherent lines, one for upper, and one for lower blowout limits. This presentation gives a visual idea of the accuracy of the blowout model. See table 6.2 for a detailed description. It is not possible to produce a more accurate model for the set of experimental data collected here, if it shall be based on an upper and lower blowout limit

6.3.4 The reliability of the model

The experimental results summarized in figure 6.7 did not allow an exact model to be made. For each nozzle, an investigation has been carried out in order to find the limit that would produce the best result. However, based on an upper and a lower blowout limit, as in this case, it is not possible to produce a model with a higher accuracy than the one that has been presented here. By this is meant that no combination of a single, coherent line representing the upper blowout limit, and a similar line representing the lower blowout limit, will yield a larger total number of correct predictions, compared to the experimental results, as the ones presented in the model in equations 6.8.

As can be seen from table 6.2, the fraction of the model prediction, compared to the experiments, is 0.89. The major source of errors are the results for the $8mm$ nozzle, representing 10 of altogether 22 wrong predictions. No mechanism has been found to explain why there are unstable flames for different flows through an $8mm$ nozzle, but the effect is discussed in chapter 7.

Table 6.2: Model prediction compared to the results for the 195 separate experiments. According to the model, diameters less than 4mm will always yield a blowout, while diameters larger than 16mm will never cause blowout, once the gas is ignited. In the intermediate range 4mm - 16mm dia., there is an upper and a lower blowout limit

Dia.(mm)	Blowout limit (kg/s)		Model prediction	
	lower	upper	right	wrong
4	(always	blowout)	16	0
6	0.008	0.251	22	1
8	0.025	0.136	36	10
10	0.039	0.250	17	2
12	0.059	0.258	23	3
14	0.231	0.231	25	4
16	(no	blowout)	34	2
		Sum	173	22
	Prediction	accuracy	89%	

Chapter 7

Discussion

7.1 What is a "stable flame"?

Figure 7.1: An example of a stable flame? This flame is close to the limit of what has been characterized as a "stable flame" (one can see the flame by carefully observing an area along the trajectory of the jet). In this case, the flame extinguished after approximately 22s (exp 31, flow 5). The criterion for calling it a stable flame, was that it should maintain combustion for at least 30s. Therefore, it was in this case registered as a blowout. However, if a different definition had been applied, or an obstacle had been present in the flow field, the flame might have become a "stable flame" instead

In order to make a choice of what could be categorized as a "stable flame", the experience used from previous work on flame characterization was combined with test runs for different nozzles to see how the jet flame behaved. The tests indicated that a flame that did not extinguish within the first $30s$ after shutdown of the pilot burners, had a strong tendency *not* to extinguish for the next $30s$ either.

In a case where e.g process equipment next to a flame had a critical impingement period of $< 30s$, a different definition could have been more suitable. But in this case, a "stable flame" is defined as an ignited gas release that most likely would undergo a continuous combustion for an unaltered flow. *Therefore, a continuous combustion of 30s or longer was chosen to be the criterion for defining it as a stable flame.*

7.2 Blowout of flames

The presence of objects impinged by a flame, would alter the flow, and consequently contribute to a possible stabilization of the flame. This is discussed by Lees [22]. In the experiments, different releases, always from circular outlets of propane in gas phase, of flows unaltered by any obstacles, were consequently studied.

Lees also discusses the mechanism of liftoff. At low velocities the flame is generally attached to the point of release, but at higher velocities it becomes detached, the distance between the orifice and the flame increasing with velocity so that it may become unstable and lift off, thus being extinguished. This was observed in the experiments. The liftoff increased with increasing flow for a given outlet diameter. However, the distance from the outlet to the far end of the flame seemed to be near constant. Unfortunately, this effect was not measured, because it was discovered too late in the experimental program.

7.3 Treatment of observations

The experiments were carried out on a limited range of flows and diameters. This is seemingly in contradiction to the range at which it is presented for. An example of this is the statement that for outlets larger than $14mm$, blowout will not occur for any ignited gas flows. Although the largest nozzle size in the experiments were $16mm$, one can, by the help of literature, assume that there will not be a new set of upper and lower blowout limits for larger diameter outlets. Both Annushkin and Sverdlov, Khalghatgi, McCaffrey and Evans, and Birch et.al worked with measurements of critical apertures related to various gas releases [2]. The work carried out by these researchers show that for circular release apertures greater than a certain critical diameter, *all* discharges produce stable jet flames. Below the critical diameter, low discharge pressure and also much higher pressures give rise to conditions where stable jet fires are possible. But there is an intermediate pressure region where flames are unstable. As discussed by Cowley and Johnson [2], the upper and lower critical pressure bounds for stability, depend on the outlet diameter and they merge at the critical diameter. The critical diameter is fuel composition dependent, which explains why a critical diameter in this work for propane, is different from e.g

the release of methane. Based on this, the extrapolations made in the model, are assumed to be valid.

Due to the limited accuracy of the pressure gauges used (too rough scale), the flow meter was considered to produce the most reliable readings in the setup. Therefore, the curves relating flow, pressure and outlet diameters shown in figure 6.8, was used to determine the pressure tied to a certain flow. When producing table 6.1, blowout limits for the different diameters were linked to the flows in figure 6.8. In the cases where diameters do not correspond with the actual nozzle diameters, interpolations have been carried out. Ideally, all lines in figure 6.8 should cross the y-axis at $p = 0bar$, and $Q =$ a small positive value, corresponding to the diffusion of the propane in air across the nozzle, increasing with increasing diameter, when there is no differential pressure across the nozzle.

The blowout model show flow limits for different nozzle diameters. In subsection 6.3.3 the same model has been presented as a table showing pressure limits for the different outlet diameters. The reason for using a table, rather than rewriting the original "flow"-equations over to "pressure"-equations, is that there are different equations tying the variables together, depending on the nozzle diameter, as shown in figure 6.8 (one equation per diameter). This made it impossible to execute a direct transfer from flow to pressure.

For the $8mm$ outlet, the experiments showed very different results from the other nozzles. In a region from 0.11 to $0.19kg/s$ there is a seemingly arbitrary mixture of blowouts and stable flames. This region is also the cause of 10 out of 22 wrong predictions done by the model. No reason has been found to explain this. The measured flows deviated very little from the $8mm$ least squares line in figure 6.8, indicating that stable blowout registrations should be registered. A possible explanation might be random variations in vortex formation, but it was never checked for this during the experiments.

Another feature that needs to be commented, is that no upper blowout limit was detected for the $10mm$ outlet. Large fluctuations in flow might explain such a behaviour. These fluctuations were unique for this nozzle, as one can clearly see in figure 6.8. The mechanism being that for a given average flow, fluctuations around this average might exceed the blowout limit at some stage. One peak value can cause the flame to blow out, although the average flow should indicate a stable flame. Although this is most relevant for the $10mm$ nozzle, the *principle* applies to the whole range of outlet diameters. This implies that the reported blowout limits will have a tendency to *overestimate* the regions of blowout, and correspondingly *underestimate* the regions of a stable flame. Although it has been an aim to seek the correct limits, this effect is not considered to be a practical problem. It will be harder to obtain stable conditions during an unforeseen discharge of gas than in a controlled environment as in this case.

The model predicts an upper blowout limit in the range $5mm < d < 8mm$ that is not as well documented through the experiments as the rest of the model. In the range up to, but not including, the $8mm$ nozzle, blowout occur for all experiments in the upper range of the flow cases. It was not possible to achieve larger flows than the ones reported for these small diameters. The reason was that although the evaporator had proven sufficient capacity for flows through the experiments with the larger diameter outlets, the pump was not able to deliver high enough driving pressures.

7.4 Potential applications of the model

Below is a list of potential applications of the model, that comes as an addition to satisfying ones curiosity for the field. The model can be used for:

- risk assessment in the process industry, as well as distribution systems carrying propane both for industrial and domestic purposes. It is mostly relevant for land based activities. Offshore, one will generally find a mixture of many different hydrocarbons, typically large fractions of the smaller molecule methane and ethane gases. The blowout limits and critical diameters for these materials differ significantly from the values for propane.
- relief valve design in propane process systems. Keeping in mind that the model applies to propane in *gas* phase, care has to be taken as to which part of a system this information is applied to.
- further research concerning blowout limits for other gases and mixtures of gases, as well as a guide for a more fundamental understanding of the involved mechanisms
- making, and validating output from, computer models

Chapter 8

Conclusions

A lot of smaller and larger observations have been made through the work on the blowout limits. Only the major findings are listed here:

- A model has been presented that predicts the upper and lower blowout limits for propane in gas phase, as well as a critical outlet diameter of $14mm$
- No observations have been made indicating that the outlet inclination has any effect on the blowout limits
- The accuracy of the model, compared to the experimental results, is a "correct prediction"-rate of 0.89
- For three different reasons, the upper blowout limit for outlets in the range $0 - 10mm$ are weakly documented: 1. For the 4 and $6mm$ nozzles, the pump was not able to deliver a high enough pressure to reach the upper blowout limit. 2. For the $8mm$ nozzle, the results scattered for an unknown reason 3. For the $10mm$ nozzle, the flow fluctuated to such an extent that it caused blowout for all experiments in the upper region

Chapter 9

Recommendations for further work

A lot more work can be done in this field, and below is a list of only a few activities that should be given more attention:

- One first step further, would be to test the least documented area in the model, i.e the upper blowout limit for outlets $\leq 10mm$.
- Perhaps the most interesting work, would be to find the blowout limits for different geometries, typically a high aspect ratio outlet, like a leak from a flange in a piping system. The flow pattern would be very different, and therefore it would be interesting to observe what will happen with the blowout limits.
- A similar work on the row of hydrocarbons from methane upwards, past butane, would tell if the blowout limits could be linked to the molecular sizes of the gases. Further tests would reveal if this knowledge could be applied to mixtures of gases, so that general equations, applying to all hydrocarbons, for upper and lower blowout limits could be made.

Appendix A

- Experimental results - Blowout

The results from the 195 blowout experiments are summarized in the following three pages. Gas pressures, flow, weather conditions etc are listed here. Conditions like e.g the humidity of the air has not been incorporated into the model presented in chapter 6. Values are listed here, for reference.

Experiment no.	Nozzle dia. 4	6	8	10	12	14	16	Angle rel. to vert. 0	45	90	Flow no.	Flow (kg/h)	P1 (barg)	P2 (barg)	Temp. gas (°C)	Not blew-out	Blow-out	Date	Time	Wind speed (m/s)	Wind dir. (degrees)	Humidity (% rel.)	Ambient temp. (°C)	Weather conditions/comments
1							x			x	1	1163			50	x		21.02.2003	1310	5 (1,0-10,3)	45	62,0	3,0	Partly cloudy, no precip., unstable wind
											2	1118			44	x								
											3	1039			44		x							
2							x			x	1	1106			52	x		21.02.2003	1400	4-8 (1-8)	50	69,0	3,5	partly cloudy, no precip., unstable wind
											2	1090			-	x								
											3	1059			-	x								
											4	1036			48	x								
											5	1015			50	x								
											6	991	7,1	5,1	56		x							
3							x			x	1	1140	8,0	6,0	48	x		24.02.2003	1050-1115	0,5	180	65,0	8,0	cloudy, no precip., calm, start: 28670 kg
											2	1057	7,5	5,5	48	x								
											3	1017	7,3	5,3	56	x								
											4	1010	7,3	5,3	62	x								
											5	996	7,1	5,2	64	x								
											6	990	7,1	5,2	64	x								
											7	962	7,0	5,0	70	x								
											8	932	6,9	5,0	72	x								
											9	885	6,2	4,5	74	x								
											10	737	5,1	3,6	74	x								
4			x							x	1	630	14,2	13,7	60	x		24.02.2003	1315-1340	2	180	64,0	3,5	cloudy, a few raindrops
											2	624	13,0	12,6	69	x								
											3	395	8,0	8,0	64		x							
5			x							x	1	670	14,8	14,6	58	x		24.02.2003	1400-1410	1,1	180	84,0	4,0	cloudy, slight rain
											2	576	11,9	11,6	70	x								
											3	510	10,6	10,3	70	x								
											4	454	9,2	9,0	67	x								
											5	412	8,3	8,1	67		x							
6			x							x	1	479	9,5	9,3	65		x	25.02.2003	1340-1355	0-2	180	82,8	6,0	cloudy, no precip., calm
7			x							x	1	640	13,7	13,2	54	x		25.02.2003	1400-1415	0-2	180	82,8	6,0	cloudy, no precip., calm, good experiment
											2	618	13,0	12,3	69	x								
											3	610	12,4	12,1	73		x							
8			x							x	1	104	0,8	0,8	44	x		25.02.2003	1420-1425	0-1	-	71,8	8,1	cloudy, no precip., calm, useless exp.
9			x							x	1	161	2,7	3,0	44		x	26.02.2003	950	1,0-2,0	150	64,0	8,8	no clouds, calm
10			x							x	1	39	0,2	0,2	41	x		26.02.2003	1010	0-1	-	49,1	8,4	no clouds, calm, good experiment
											2	48	0,2	0,2	40	x								
											3	61	0,3	0,3	40	x								
											4	75	0,5	0,5	41	x								
											5	93	0,8	0,7	43		x							
11	x									x	1	214	16,9	16,5	48		x	26.02.2003	1040	0-2	30	69,0	8,5	no clouds, almost calm
12	x									x	1	280	16,0	16,5	52		x	26.02.2003	1110-1115	0-2	30	69,0	5,5	no clouds, almost calm
13	x									x	1	25	2,4	2,9	40		x	26.02.2003	1120-1130	0-2	45	68,7	5,7	no clouds, almost calm
14	x									x	1	18	1,0	1,0	37		x	26.02.2003	1135-1145	0-2	45	69,0	5,5	no clouds, almost calm
15							x		x		1	1200	8,6	6,3	48	x		26.02.2003	1310-1325	2-4 (1-8)	150	33,0	10,9	no clouds, draft, nozzle near melted start: 27943 kg
											2	999	7,3	5,3	58	x								
											3	872	6,4	4,6	64	x								
											4	746	5,3	3,9	70	x								
											5	613	4,2	3,0	70	x								
											6	471	3,0	2,0	70	x								
16							x		x		1	397	2,4	2,0	63	x		26.02.2003	1345-1355	2,0-4,0	150	35,2	10,6	no clouds, almost calm, stable flame for all flows
											2	278	1,3	0,8	64	x								
											3	180	0,6	0,2	64	x								
											4	94	0,1	0,1	64	x								
17			x						x		1	617	13,1	12,6	62	x		26.02.2003	1405-1500	2,0-5,0	150	33,5	10,7	no clouds, slight draft, good experiment first exp. where it was continued after blow-out
											2	690	14,6	13,8	66	x								
											3	682	14,8	14,0	70	x								
											4	543	11,2	11,0	73	x								
											5	439	9,0	8,9	73		x							
											6	475	9,8	9,5	72		x							
											7	495	10,2	10,0	74	x								
											8	486	10,0	9,8	74		x							
											9	19	0,2	0,2	60	x								
											10	29	0,2	0,2	50	x								
											11	48	0,2	0,2	48	x								
											12	106	1,2	1,0	52		x							
											13	283	5,1	4,9	56		x							
											14	174	3,2	3,1	61		x							
											15	78	0,9	0,8	58	x								
											16	96	1,0	1,0	54		x							
											17	93	1,1	1,1	51	x								

Experiment no.	Nozzle dia							Angle rel. to vert.			Flow no.	Flow (kg/h)	P1 (barg)	P2 (barg)	Temp.gas (°C)	Not blow-out	Blow-out	Date	Time	Wind speed (m/s)	Wind dir. (degrees)	Humidity (% rel.)	Ambient temp. (°C)	Weather conditions/comments
	4	6	9	10	12	14	16	0	45	90														
18	x								x		1	182	15,3	15,5	44		x	27.02.2003	1515	0-2	200	42,0	7,8	no clouds, calm, end: 28590 kg
											2	149	13,2	13,2	62		x							
											3	116	10,8	10,8	61		x							
											4	79	8,2	8,2	60		x							
											5	43	4,2	4,2	56		x							
											6	29	2,1	2,1	48		x							
											7	18	1,3	1,3	42		x							
19		x							x		1	845	14,6	13,9	62		x	27.02.2003	1120-1156	0 (0-2)	-	33,8	6,8	no clouds, calm, start: 28598 kg
											2	513	10,7	10,5	66		x							
											3	421	8,8	8,7	66		x							
											4	305	6,2	6,1	67		x							
											5	202	3,9	3,8	68		x							
											6	107	1,5	1,5	67		x							
											7	58	0,4	0,4	62	x								
											8	76	0,6	0,6	56		x							
											9	63	0,5	0,5	53	x								
											10	70	0,6	0,6	51		x							
20				x				x			1	1143	8,2	6,0	42	x		27.02.2003	1425-1445	0-2	-	29,4	9,2	no clouds, calm, start: 28787 kg
											2	1023	7,5	5,5	46	x								
											3	785	4,9	4,2	56	x								
											4	595	3,5	2,4	68	x								
											5	297	1,5	0,9	69	x								
											6	154	0,4	0,2	67	x								
											7	57	0,0	0,0	64	x								
21	x								x		1	175	15,0	15,0	64		x	27.02.2003	1450-1520	0-2	-	ca 30	9,8	no clouds, calm, end: 29010 kg
											2	121	11,3	11,2	59		x							
											3	66	8,4	8,5	63		x							
											4	40	4,0	4,0	66		x							
											5	18	1,1	1,2	51		x							
22			x						x		1	1028	10,5	9,7	46	x		28.02.2003	0910-0936	0-2	-	84,0	1,8	cloudy, calm, no precip., safety valve released, shut down the rig
											2	1173	12,8	11,8	54	x								
23			x						x		1	709	7,4	6,6	60		x	28.02.2003	0935-0955	0-2	150	ca 84	ca 1,0	cloudy, calm, no precip., unstable flame start: 29152 kg
											2	894	9,2	8,7	70		x							
											3	890	9,7	9,0		x								
34			x						x		1	834	9,7	8,9	62	x		28.02.2003	1305-1335	2,0-5,0	90	76,0	3,3	partly cloudy, slight draft, no precip. start: 29664 kg
											2	388	3,5	3,0	65		x							
											3	187	1,1	1,0	66	x								
											4	286	2,3	2,0	66	x								
25			x						x		1	854	11,3	10,9	66		x	28.02.2003	1345-1405	0-2	90	46,6	5,4	no clouds, slight draft
											2	530	6,8	6,5	68		x							
											3	306	2,0	2,0	64		x							
											4	197	0,6	0,6	50	x								
											5	145	1,1	1,0	47		x							
											6	125	0,8	0,7	45	x								
											7	137	0,9	0,9	41	x								
26			x						x		1	895	9,8	8,9	43	x		28.02.2003	1440-1510	0-2	150	46,9	6,1	no clouds, calm
											2	880	9,2	8,4	56	x								
											3	669	7,0	6,3	68		x							
											4	752	8,0	7,2	70	x								
											5	699	7,4	6,9	72		x							
											6	385	3,7	3,4	73		x							
											7	230	1,7	1,5	70		x							
											8	199	0,3	0,3	69	x								
											9	188	1,1	1,0	65	x								
											10	190	1,2	1,0	63	x								
											11	266	1,4	1,2	63	???????								
27		x							x		1	769	12,5	12,5	59		x	28.02.2003	1515	0-2	45	ca 50	ca 6	no clouds, calm, start: 30180 kg
											2	417	6,9	6,7	71		x							
											3	283	3,2	3,2	66		x							
											4	189	1,0	1,0	63	x								
											5	142	1,8	1,5	62		x							
											6	121	1,2	1,1	61		x							
28		x								x	1	883	10,2	9,4	45	x		28.02.2003	1550-1610	0-1	30	64,7	7,7	no clouds, calm, start: 30230 kg
											2	825	9,7	8,9	54		x							
											3	729	7,7	7,2	60		x							
											4	481	3,5	3,5	58		x							
											5	281	1,4	1,2	50	x								
											6	310	2,7	2,5	42		x							
											7	242	1,8	1,5	40		x							

Experiment no.	Nozzle dia.							Angle rel. to vert.			Flow no.	Flow	P1	P2	Temp.gas	Not blow-out	Blow-out	Date	Time	Wind speed	Wind dir.	Humidity	Ambient temp.	Weather conditions/comments
	4	6	8	10	12	14	16	0	45	90		(kg/h)	(barg)	(barg)	(°C)					(m/s)	(degrees)	(% rel.)	(°C)	
29				x						x	1	718	11,8	11,4	42		x	28.02.2003	1630-1650	0-1	30	ca 56	ca 7	no clouds, calm, start: 30420 kg
											2	415	6,7	6,5	60		x							
											3	206	2,8	2,7	62		x							
											4	104	0,9	0,9	61	x								
											5	153	2,0	2,0	60		x							
											6	125	1,3	1,3	60		x							
30						x				x	1	1117	9,5	8,8	54	x		13.03.2003	0830-0910	0-1	-	60,2	11,2	no clouds, calm
											2	831	8,0	6,7	59	x								
											3	758	6,4	5,4	70	x								
											4	511	4,0	3,3	71	x								
											5	403	2,9	2,3	72	x								
											6	299	1,8	1,4	70	x								
											7	203	0,9	0,8	70	x								
											8	101	0,2	0,2	66	x								
											9	50	0,1	0,1	62	x								
											10	19	0,0	0,0	58	x								
											11	1216	10,2	8,7	50	x								
31		x								x	1	379	15,5	15,1	60		x	13.03.2003	0935-1000	0-1	-	53,3	10,6	no clouds, calm
											2	315	13,6	12,8	64		x							
											3	210	8,6	8,5	66		x							
											4	106	4,7	4,4	65		x							
											5	51	1,7	1,8	63		x							
											6	24	0,7	0,7	57	x								
											7	37	0,5	0,5	52	x								
											8	44	0,8	0,8	51		x							
32						x			x		1	1157	9,8	8,2	54	x		13.03.2003	1110-1135	1,0-3,0	0	65,6	6,6	no clouds, calm
											2	830	7,2	6,0	58		x							
											3	963	8,3	7,0	70		x							
											4	519	4,5	3,8	66		x							
											5	386	2,8	2,3	67		x							
											6	218	1,0	0,7	67	x								
											7	318	2,0	1,7	68		x							
											8	103	0,3	0,3	69	x								
											9	51	0,2	0,2	65	x								
											10	25	0,0	0,0	61	x								
33		x							x		1	375	15,4	15,0	64		x	13.03.2003	1145-	1-3,5	315	64,3	7	no clouds, some draft
											2	302	12,2	12,2	62		x							
											3	214	8,8	8,8	66		x							
											4	99	4,2	4,2	65		x							
											5	51	2,1	2,1	63		x							
											6	24	0,3	0,3	58	x								
											7	35	0,4	0,4	53		x							
34						x		x			1	1110	9,4	8,8	50	x		13.03.2003	1240-1305	0-3	300	56,6	8,3	no clouds, some draft
											2	945	8,2	7,0	64	x								
											3	772	6,7	5,7	66	x								
											4	504	3,9	3,2	67	x								
											5	360	2,4	2,0	67	x								
											6	198	0,9	0,7	66	x								
											7	103	0,3	0,3	65	x								
											8	50	0,2	0,2	63	x								
35		x						x			1	371	15,4	15,0	61		x	13.03.2003	1310-1345	0-2	0	56,3	8,6	no clouds, some draft
											2	287	11,8	11,7	66		x							
											3	148	6,0	6,0	66		x							
											4	97	4,0	4,0	64		x							
											5	50	2,0	2,0	62		x							
											6	24	0,9	0,9	58	x								
											7	32	0,3	0,3	52		x							
											8	27	0,4	0,4	50	x								

Bibliography

[1] Warnats, J.; Maas, U.; Dibble, R.W.
Combustion. Physical and Chemical Fundamentals, Modelling and Simulation, Experiments, Pollutant Formation,
Springer-Verlag, 2000

[2] Cowley, L.T.; Johnson, A.D.
Blast and Fire Engineering Project for Topside Structures, Fire Loading series,
Shell International Research Mij. BV, Feb, 1991

[3] Annushkin, Yu.M.; Sverdlov, E.D.
Stability of Submerged Diffusion Flames in Subsonic and Underexpanded Supersonic Gas-Fuel Streams,
Combustion, explosion and shock waves, 1978

[4] Kalghatgi, G.T.
Blow-out Stability of Gaseous Jet Diffusion Flames. Part I: In Still Air,
Combustion Science and Technology, 1981

[5] Kalghatgi, G.T.
Blow-out Stability of Gaseous Jet Diffusion Flames. Part II: Effect of Cross Wind,
Combustion Science and Technology, 1981

[6] McCaffrey, B.J.; Evans, D.D.
Very Large Jet Diffusion Flames,
21^{st} Int.Symp.on Comb., 1986

[7] Birch, A.D.
Flame Stability in Under Expanded Natural Gas Jets,
Combustion Science and Technology, 1988

[8] Wakes, S.J.; Hold, A.E.; Meares, A.J.
Experimental investigation of the effect orifice shape and fluid pressure has

on high aspect ratio cross-sectional jet behaviour,
Journal of Hazardous Materials, 2002

[9] Ertesvåg, I.
Turbulent Strøyming og Forbrenning - Frå turbulensteori til ingeniørverkty,
Tapir akademisk forlag, Trondheim, Norway, 2000. ISBN 82-519-1568-6

[10] Bish, E.S.; Dahm, W.J.A.
Strained dissipation and reaction layer analysis of nonequilibrium chemistry in turbulent reacting flows,
Combustion and Flame, 100:456, 1995

[11] Dahm, W.J.A.; Bish, E.S.
High resolution measurements of molecular transport and reaction processes in turbulent combustion, in:,
Turbulence and molecular processes in combustion (Takeno, T. ed), p. 287, Elsevier, New York, 1993

[12] Birch, A.D.; Brown, D.R.; Dodson, M.G.; Thomas, J.R.
The Turbulent Concentration Field of a Methane Jet,
J.Fluid Mech., 88 (3), 431

[13] Lydersen, A.L.
Fluid Flow and Heat Transfer,
John Wiley & Sons pp 37-54, 1979

[14] Lyons, K.M.; Watson, K.A.; Carter, C.D.; Donbar, J.M.
On flame holes and local extinction in lifted-jet diffusion flames,
Combustion and Flame, Vol. 142, Issue 3 , pp 308-313, 2005

[15] Kronenburg, A.; Kostka, M.
Modelling extinction and reignition in turbulent flames,
Combustion and Flame, Vol. 143, Issue 4 , pp 308-313, 2005

[16] Su, L.K.; Sun, O.S.; Mungal, M.G.
Experimental investigation of stabilization mechanisms in turbulent, lifted jet diffusion flames,
Combustion and Flame, Vol. 144, Issue 3 , pp 494-512, 2006

[17] Wu, C.-Y.; Chao, Y.-C.; Cheng, T.S.; Li, Y.-H.; Lee, K.-Y.; Yuan, T.
The blowout mechanism of turbulent jet diffusion flames,
Combustion and Flame, Vol. 145, Issue 3 , pp 481-494, 2006

[18] Wang, H.Y.; Chen, W.H.; Law, C.K.
Extinction of counterflow diffusion flames with radiative heat loss and non-unity Lewis numbers,
Combustion and Flame, Vol. 148, Issue 3 , pp 100-116, 2007

[19] Hermanns, M.; Vera, M.; Linan, A.
On the dynamics of flame edges in diffusion flame/vortex interactions,
Combustion and Flame, Vol. 149, Issue 1-2 , pp 32-48, 2007

[20] Leung, T.; Wierzba, I.
The effect of co-flow stream velocity on turbulent non-premixed jet flame stability,
Proceedings of the Combustion Institute, Vol. 32, Issue 2 , pp 1671-1678, 2009

[21] Kaiser, S.A.; Frank, J.H.
Spatial scales of extinction and dissipation in the near field of non-premixed turbulent jet flames,
Proceedings of the Combustion Institute, Vol. 32, Issue 2 , pp 1639-1646, 2009

[22] Lees, F.P
Loss Prevention in the Process Industries; Hazard Identification, Assessment and Control; Volume 2,
Butterworth Heinemann 2^{nd} edition, ISBN 0-7506-1547-8, 1996

PART III - HEAT ATTENUATION IN WATER SPRAY IN A FULL SCALE OFFSHORE FLARE SITUATION

Contents

List of Figures

List of Tables

Chapter 1

Introduction

In 2008, the total worldwide energy consumption was 474 exajoules ($474 \times 10^{18} J$) with 80-90% derived from the combustion of fossil fuels (oil, gas and coal). Keeping coal out of the equation, gas and oil represented approximately 60% of the world´s total energy consumption. The estimates of remaining non-renewable worldwide energy resources vary, with the remaining fossil fuels totaling an estimated 0.4 YJ ($1YJ = 10^{24} J$) [1]. This means that the remaining fossil fuel resources represent $\approx$ 840 years´consumption at the 2008 level. However, the limiting sustainability for the environment represent a massive challenge long before these resources are consumed.

Even though the world society focus on the problems related to global warm up, and therefore seeks reduction in the release of CO_2 and other gases with even higher global warming potential (GWP), oil and gas will still be our most important energy sources for years to come. Massive systems are still being built for extraction, refinement, storage and distribution of hydrocarbons. Limits are pushed geographically, and the tendency now is to move north to (sub)arctic regions. All these activities represent risks in different ways, both for personnel, equipment and the environment.

There is a considerable risk involved in the handling of these hydrocarbons, that has to be addressed as long as the activity continues. This problem historically became more evident when the production moved from land based sites to offshore drilling units, with their limited spaces to carry out all activities. In order to meet the safety challenges, rules and regulations have been introduced by national authorities and class companies, rig owners have added their own regulations in order to *act*, rather than *react*, on the safety hazards, and to win the competition for personnel with the right attitude to meet the risks involved.

Due to the geometry of an offshore drilling rig, it has got limited possibilities of keeping sufficient distances between equipment, processes, people etc, unless barriers are introduced. This means that, while test flaring, the flame will be in a position near to the rig itself. In the absence of proper cooling, radiation from the flare will in most cases be too intense for the structure and the people working in the well test areas. Sea water is normally used for this purpose. It is environmental friendly, easily accessible and an effective coolant. However, it can not be applied directly into the combustion zone, because that will cause incomplete combustion and release of oil and gas to the environment. Also, applying water as a direct coolant on the surfaces of the rig and its equipment,

will cause a difficult working environment for the crew. Therefore, a shield, in the form of a water curtain, between the rig and the flare, can be of good help. However, this solution will in most cases be insufficient as a full protection, and therefore it will normally be used in combination with direct cooling of the surfaces on the rig and its equipment.

Chapter 2

Objects of work

Scarabeo5, a semi submersible drilling rig owned by Saipem S.p.A, and operated by Statoil at the time, had to upgrade its capability in order to handle increased oil and gas flow rates from 10K BOPD (i.e a hydrocarbon flow with energy equivalent of 10,000 barrels of oil per day) to 15K BOPD for operations in the Kristin field in the Norwegian Ocean. This included a heat radiation attenuation system, i.e a *water curtain*, between the burner booms and the rig sides. The aim was to produce a water curtain that absorbed the heat sufficiently to meet the requirements of the API and the DoE standards. API RP521 require a maximum radiation of $500 Btu/hr/ft^2$, corresponding to $1,58 kW m^{-2}$, at any location where personnel are continuously exposed. Examples of this, are the well test areas close to the burner boom. Also, the wetting of exposed surfaces by means of a rig side/equipment in well test area cooling system, had caused a wet and cold working environment for the crew.

Thus, the object for the customer, was to acquire a system that provided a water curtain with the capacity to reduce the radiation in the well test area to a value less than $1,58 kW m^{-2}$, without the use of the rig side cooling system.

The author´s employer, West Contractors AS was handed the contract for engineering, procurement, construction and commissioning of this job. In addition, it was in the interest of both the author, the rig owner and the operator to collect and compare data regarding the calculated and actual heat attenuation in the water curtain. Very little data exist in this field, which lead to a parallel object for *this* project.

The object of this project has been to:

- use a known heat attenuation model to calculate the incoming radiation at Scarabeo5 for the relevant water curtain flow and flare radiation conditions
- measure the *actual* incoming radiation
- make a comparison between the results and, if necessary, propose improvements of the applied model, in order to present a verified model for engineering use

Chapter 3

Situation

In order to get an overview, this chapter provides information of the situation that formed the basis for this project, and the special challenges associated with collecting data from a full scale situation on a drilling unit in operation. The opportunity to control factors like weather, operational decisions, time to run and *how* to run experiments etc, was therefore limited.

Most of the activities carried out in this project, are of no direct interest to the heat attenuation part, and these are only briefly mentioned.

Different water curtain solutions had already been applied for heat attenuation of the radiation from the flare. But the increased flow rate of oil and gas, and experience with the existing water curtain including small (fog) droplets had proven to be less efficient than expected in the windy conditions offshore. The water fog had a tendency to blow sideways to such an extent that it did not provide a sufficiently large water curtain. Thus, the benefit of a large heat attenuation per kg of water was not available in this case. Large drop sizes with a significant momentum was required. This implied that the new system was designed with an enhanced capability of water flow.

3.1 The flare

A rough sketch of the flare is shown in figure 3.1. The oil was released at an angle of $\approx 45^0$ upwards, and the gas was released horizontally. There were altogether 4 nozzles discharging oil. The directions are most easily seen as white bands in the photographs in figure 6.5. Although the sketch shows a clear distinction between the gas and the oil, the reality was that these two flame types tended to merge into each other, as can be seen in figures 6.1 - 6.5. However, the contribution from the gas flare was limited; in general, there is larger radiation from an oil than a gas flare. Also, the centre of the flame was closer to the rig side for the oil compared to the gas flare.

From photographs during the actual flaring, the following estimates were made: The flame height during flaring was $22m$. The centre of the flame was $38m$ out from the rig side, and $11m$ above deck level.

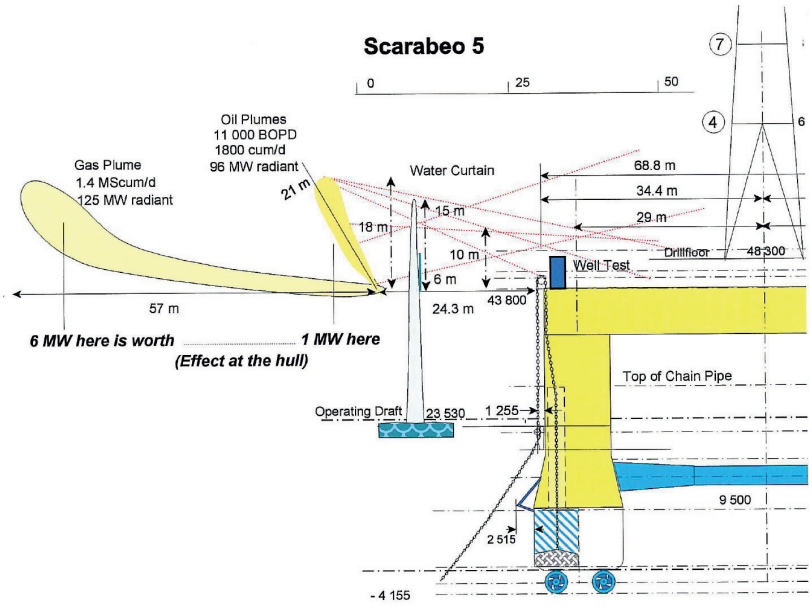

Figure 3.1: Sketch of rig, burner boom and flare. There were altogether 4 nozzles discharging oil. The directions are most easily seen as white bands in the photographs in figure 6.5

3.2 Hydrocarbon flow rates

Several different oil and gas flow rates were involved in the design process of this project; examples are design flow rates in the Statoil´s tender documents, Flaresim rates used in the radiation simulations, or the measured, actual rates. Only two were of interest:

- the rates used in the radiation *simulations*. The reason for these rates to be relevant, was that due to safety reasons, it was not allowed to flare without the water curtain in operation. Therefore, no measured data of the radiation without the water curtain was obtained, and the efficiency of the water curtain is thus only partly based on measured values. The relevant simulated rates were: $1,282 m^3/d$ oil and $1,000,000 STD\ m^3/d$ gas

- the measured rates during flaring. The average rates, used in the calculations, were $1,380 m^3/d$ for oil, and $1,290,000 STD\ m^3/d$ for gas. The flow rates could be characterized as "stable" in the sense that the deviations

were 1.2% and 0.4% of the flow rates for oil and gas, respectively. This is shown in table 6.1, and a complete overview is given in subsection 6.2.1.

3.3 Estimation of radiation levels - Flaresim

Once the estimated flow rates had been established, corresponding radiation levels at different positions onboard the rig, without any heat attenuation system, needed to be assessed. The chosen tool for this, was the Flaresim simulation software.

3.3.1 General

Flaresim is a software which has been developed for flame shape, radiation and noise predictions. It uses the heat release rates, HRR, and the fraction of the combustive energy which is radiated, F-factor, for the relevant hydrocarbon and flow conditions, in order to calculate the relevant surface emissive power, SEP, of the flame. The program then calculates, and plots, iso-radiance spheres, indicating the radiation at any distance away from the flame. The F-factor used by Flaresim for *sonic* flow, as in this case, is 0.1. This means that Flaresim is designed for natural gas flares.

Shell Research Ltd [2], performed a number of tests for six different radiation prediction models, Flaresim included. The test closest to this water curtain project, was a vertical, sonic natural gas jet fire of several million $STDm^3/day$. This showed a ratio of predicted/actual values of 1.48 for flame length, 1.05 for far radiation, and 1.03 for near radiation. Unfortunately, comparisons were not made for release of oil.

3.3.2 Radiation from model

The Optima Flaresim report 05-225, 22^{nd} November 2005, "Case study 1: $1,282m^3/d$ Oil, $1,000,000STD\ m^3/d$ Gas, No Wind, No Water Screen", is very similar to the test conditions. Iso-radiance lines at deck level were plotted for this situation, see figure 6.14. Also, a section of the radiation levels was made, see figure 6.13. These plots show radiation in the range $8-12kW/m^2$ in the well test area with no water curtain present, i.e well above the limit of $1.58kW/m^2$.

An extra 5-8% increase in radiation was added to account for the actual oil flow rate of $1,380m^3/d$ rather than a rate of $1,282m^3/d$, and $1,290,000STD\ m^3/d$ of gas rather than the $1,000,000STD\ m^3/d$ in the simulation. Ideally, a new simulation should have been run after flaring, corresponding to the actual hydrocarbon flow rates. This was a cost/benefit question in the project, and was not given priority.

3.4 Water supply system and estimated water flow rates

In order to make a suitable water curtain, a pipe and nozzle system was made. This arrangement was called a butterfly, and can be seen in the figures, section 5.1. The water supply for the butterfly consisted of one main pump in the

starboard, and one in the port pontoon. In addition, new booster pumps were mounted in the burner boom area, also here with one on starboard and one on port side. 6" pipes, one on each side, supplied water along the burner boom. The water supply system also fed the rig side nozzles with water, and a sketch of all pipes and nozzles can be seen in figure 3.2. Hydraulic calculations were carried out for the complete system of butterfly and rig side cooling. Both the friction losses calculated by Hazen-Williams equation, and static head losses were taken into account according to the European Insurance Committee rules CEA 4001:2000-04. These are the common European rules for sprinklers and deluge.

At stage 1 in this project, the flow in the 6" pipe feeding water to the butterflies, was measured. The flow measurements corresponding to the radiation measurement conditions carried out later, at stage 2, are found in Appendix A, (-"Q", -"port side", -"situation 6", i.e Flare boom cooling. Booster and deluge pump running). The relevant flow for the heat attenuation experiment was $75.6 l/s$.

3.5 Nozzle and coverage

The full name of the applied nozzles is *GW Thermoshield Model 883B Flat Fan Fog Vertical Partition Nozzle*, hereafter referred to as the *GW nozzle*, or simply the *nozzle*. This nozzle type has a K-factor of 260. The K-factor is a constant determined by the geometry of the nozzle, and is defined as $K = \frac{Q}{\sqrt{P}}$, where Q is the water flow measured in l/min, and P is the pressure drop across the nozzle, measured in bar. The idea of the K-factor can be applied to more than a single nozzle. For example, a branch of a pipe and nozzle system, a group of nozzles, or even a complete cooling system has got its own K-factor. As long as the geometry and orientation is defined, the system will follow the equation for the K-factor. This feature has been used when adjusting the calculations from a theoretical, calculated flow over to the actual measured flow.

The water curtain for each nozzle can be described as a rectangular slab, $10m$ high by $11m$ wide by $0.9m$ thick, containing droplets of dispersion 70% $1mm$ dia. and 30% $0.5mm$ dia, to a mass density of $0.18 kg/m^3$ per nozzle.

Experiments with high speed photography of the drop size distribution was attempted in a separate project onshore. Unfortunately, this was no success. It was not possible to determine drop size, speed or mass density from the images.

Therefore, the described distribution was a result of a qualified best guess, resulting from a discussion with one of Norway´s lead experts in the field, prof. Torgrim Log at Stord/Haugesund University College.

More detailed information of nozzle shape, flow characteristics and water curtain sizes are found in figures 5.2 - 5.4.

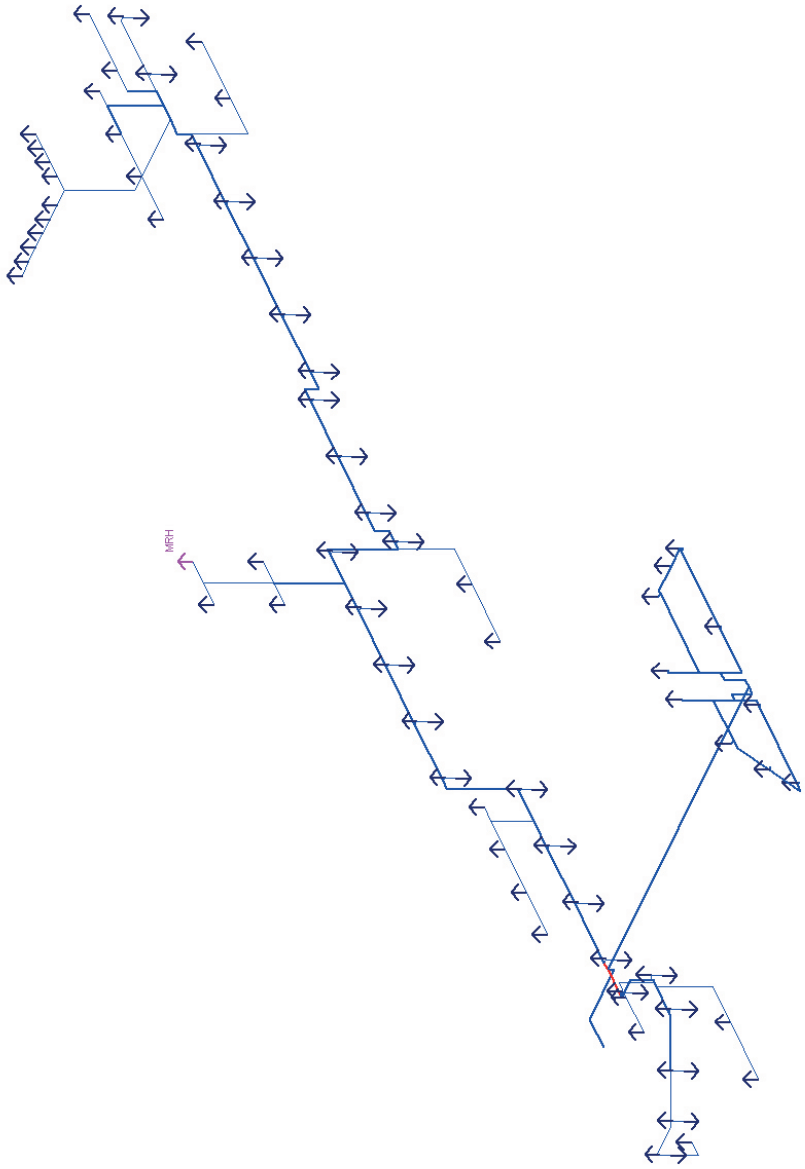

Figure 3.2: STB cooling system, nozzles for water curtain is found at bottom right in this figure

Chapter 4

Applied theory

4.1 Applied procedure

For the design of a water curtain with a proper heat attenuation as described in chapter 2, calculations had to be carried out. The purpose was to find a correct water supply for the proposed butterfly arrangement. A procedure suggested by prof. Torgrim Log was applied. This procedure accounts for water droplet distribution, water curtain density and heat absorption for different wavelengths. By kind permission from prof. Log, the procedure is reported in this section. The non relevant parts of the original article has been left out in this chapter. For more details, see [3].

A combination of discrete monodisperse sprays were initially assumed. There were no information available regarding the size and distribution of droplets produced by the nozzles for any pressure drop across the nozzles.

Information of the size of the curtain from each individual nozzle, the number of nozzles and their directions were combined. New, and better, estimates of the curtain characteristics were then made. The results from this work are plotted in figures 6.15 - 6.18.

4.1.1 Radiative heat transfer

The emissive power of a perfect black body is given by [4]:

$$E_{\lambda T} = \frac{2\pi c^2 h}{\lambda^5} \frac{1}{e^{(ch/\lambda KT)} - 1} \qquad (Wm^{-2}m^{-1}) \tag{4.1}$$

where

c = speed of light in vacuum ($2.9979250 \times 10^{-8} ms^{-1}$)
K= Boltzmann constant ($1.380622 \times 10^{-23} JK^{-1}$)
λ= wavelength (m)
T= temperature (K)

$E_{\lambda T}$ for temperatures relevant for flares is shown in fig 4.1(a). The total emissive power of the black body is given by integration over all wavelengths:

$$E_T = \int_0^\infty E_{\lambda T} d\lambda = \frac{2\pi^5 K^4}{15c^2h^3} T^4 = \sigma T^4 \qquad (Wm^{-2}) \tag{4.2}$$

where

$$\sigma = \text{Stefan-Boltzman constant } (5.67 \times 10^{-8} Wm^{-2} K^{-4})$$

Assuming a "grey body", i.e that the emissivity of the surface is independent of the wavelength, the emissive powers of the "grey body" are simply given by $\varepsilon \cdot E_{\lambda T}$ and $\varepsilon \cdot E_T$, respectively. For luminous flames, like a flare, the radiation is due to small carbon particles behaving like numerous perfect black bodies. If the flame is not optical thick ($\varepsilon = 1$), the Lambert emissivity of the flame is a function of absorption coefficient (α_F) and flame thickness (L_F):

$$\varepsilon_F = 1 - exp(-\alpha_F L_F) \tag{4.3}$$

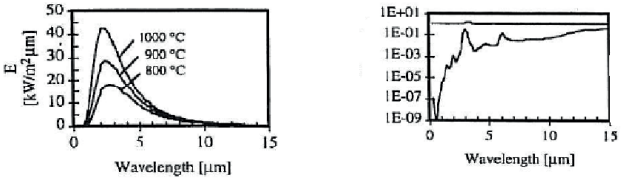

(a) (b)

Figure 4.1: (a) Black body emissive power ($E_{\lambda T}$) and (b) extinction coefficient (k_λ) and refractive index (n_λ) of water

In order to calculate the radiant intensity at a distant point, a geometrical factor (view factor) is introduced. The radiative heat flux from a hot surface dA_1 to a distant object dA_2, is given by [5]:

$$\dot{q}_r'' = E_T \int_0^{A_1} \frac{cos(\theta_1) cos(\theta_2)}{\pi r^2} dA_1 = \phi E_b \tag{4.4}$$

where

ϕ = configuration factor
r = distance between dA_1 and dA_2
θ_1= angle of inception at dA_1
θ_2= angle of inception at dA_2

Values of ϕ are easily obtained by numerical integration of equation 4.4, or from tables and charts in the literature [6][7].

4.1.2 Reflection and absorption in bulk water

The radiant heat flux reduction through water film in air is due to reflection at the two phase boundaries and by absorption in the bulk of the water film. In general, reflection of light by a transparent medium in air is given by Fresnels formulae [8]:

$$R = \frac{1}{2}\frac{sin^2(\theta_i - \theta_r)}{sin^2(\theta_i + \theta_r)}\frac{tan^2(\theta_i - \theta_r)}{tan^2(\theta_i + \theta_r)} \tag{4.5}$$

where

θ_i = angle of inception
θ_r = angle of refraction

Similar to the emissivity of flames, the Lambert absorption is given by:

$$\epsilon_\lambda = 1 - exp(\alpha_\lambda \tau) \tag{4.6}$$

where

τ = path length
α_λ= Lambert absorption coefficient

$$\alpha_\lambda = \frac{4\pi k_\lambda}{\lambda} \tag{4.7}$$

where

λ = wavelength (m)
k_λ= extinction coefficient

The extinction coefficient and the Lambert absorption coefficient are shown in figures 4.1(b) and 4.2(a), respectively. The path length through the water film of thickness L is given by:

$$\tau = \frac{L}{cos(\theta_r)} \tag{4.8}$$

where the angle of refraction (θ_r) is given by Snells law [9]:

$$\frac{sin(\theta_i)}{sin(\theta_r)} = \frac{n_i}{n_r} \tag{4.9}$$

where

θ_i = angle of incidence
n_i = refractive index of the medium of incidence
n_r = refractive index of the medium of refraction

Minimum reflectance is given at normal incidence by ($n_{air} \approx 0$):

$$R_\lambda = \frac{n-1}{n+1}^2 \tag{4.10}$$

see fig. 4.3(b). Minimum absorption is also obtained at normal incidence since the path length (τ) then is equal to the film thickness. Eliminating the minimal amount of light being reflected back and forth within the bulk of the water film, the fraction of thermal radiation being transmitted through the water film and two face boundaries, is obtained by integrating over all wavelengths (integrating from 0.2 μm to 30 μm will do for temperatures observed in fires):

$$\gamma = E_T^{-1} \int_0^\infty a_\lambda E_{b\lambda} (1 - R_\lambda)^2 d\lambda \tag{4.11}$$

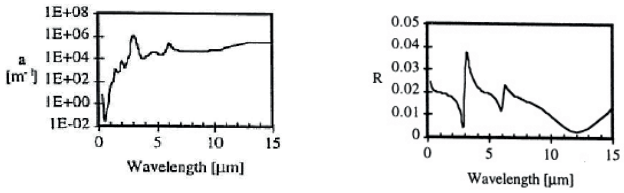

(a) (b)

Figure 4.2: (a) Absorption coefficient of water. (Data for k_λ from Hale et al [8]) and (b) Reflection (R_λ) at the water air face boundary (normal incidence). (Data for n_λ from Hale et al [8])

4.1.3 IR attenuation in water sprays

Defining water spray classes

Mawhinney et al [10] proposed three classes for dividing the water mist into "coarser" and "finer" spray. Plotting the cumulative percent volume distributions (CPVD) of the spray, the CPVD for a "Class 1" spray will plot entirely to the left of the line connecting $D_{v0.1} = 100\mu m$ and $D_{v0.9} = 200\mu m$, see fig 4.3(a). The terms $D_{v0.1}$ and $D_{v0.9}$ refer to the diameters for which 10% and 90% respectively, of the volume of the spray is contained in smaller droplets, measured in standard manner [10] [11]. The CPVD for a "Class 2" water spray will plot entirely to the left of the line connecting $D_{v0.1} = 200\mu m$ and $D_{v0.9} = 400\mu m$. A distribution curve that extends to the right of that line is considered being a "Class 3" water spray.

IR attenuation in monodisperse sprays

The attenuation of radiant heat in water sprays is a complex phenomenon involving absorption and scattering at wavelenths of the size of the smaller droplets. Studies of radiant heat attenuation in a volume containing spheres where both the refractive index and the extinction coefficient are strongly dependent of wavelength, with molecular absorption bands, therefore require simplified models. Two such models have been found in the literature survey.

Beer-Lambert law assumption

The first model, presented by Ravigururajan and Beltran [12], is a simplification based on a Beer-Lambert law assumption, i.e an exponential decay in radiation intensity with path length. The optical properties of water (the complex index $n^* = n - ik$) indicates, however, that diffusion plays an important role compared to absorption, especially at wavelengths below $5\mu m$, i.e where the emissive power is largest (fig.4.1(a)). It is therefore necessary not only to calculate the direct transmitted fluxes, but also the fluxes diffused (scattered) through the water spray.

The two flux method

The second model, presented by Coppalle et al [13] is based on the two flux method [7] [14] [15], which reduces the rays diffused in all directions from a drop to two beams: one travelling in the forward direction of the incident radiation, the other travelling in the opposite (backward) direction, see fig.4.3(b). The larger drops, the more accurate this method works.

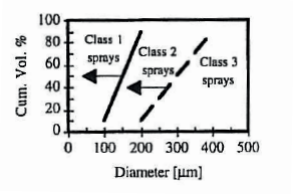

(a)

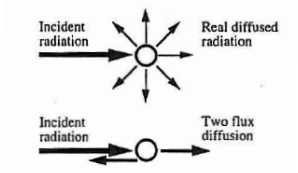

(b)

Figure 4.3: (a) Proposed fine water spray classification system [10] and (b) Principle for the two-flux diffusion model [13]

Given the characteristics of the monodisperse spray: spray length (spray thickness) L, water load M and drop diameter d, the transmitted spectral flux is given by:

$$q_\lambda = E_{\lambda T}\frac{2ge^{(-g\tau)}}{w(1-f)R(e^{(-2g\tau)}-1)+1-wf+g+(g+wf-1)e^{(-2g\tau)}} \quad (4.12)$$

where

k_{ext} = extinction coefficient (=$Q_{ext}L$)
w = the albido of the drop (=ratio of diffusion efficiency to extinction efficiency)
R = reflection factor of the target
τ = effective extinction coefficient
f = angular dissymmetry factor

f is given by:

$$f = \frac{1}{2}\int_0^1 P(\theta)dcos(\theta) \quad (4.13)$$

where $P(\theta)$ is the phase function of the drop. Q_{ext}, w and f are parameters specific to a drop of water of diameter d and index n^*= n-ik. They characterize its optical properties and are calculated in terms of d and n^* according to Mies theory [15], or according to a simplified procedure such as suggested by Coppale et al [13]. Integration of q_λ over the entire range of wavelengths gives the total flux transmitted through the spray:

$$q_{tr} = \int_0^\infty q_\lambda d\lambda \quad (Wm^{-2}) \quad (4.14)$$

The fraction of the heat flux transmitted through the spray may then be calculated by:

$$\tau = \frac{q_{tr}}{E_T} \quad (4.15)$$

In order to calculate the transmitted spectral flux, q_λ, these parameters have to be calculated [13]:

$$\alpha = \frac{\pi d}{\lambda} \tag{4.16}$$

$$X = 2\alpha(n_\lambda - 1) \tag{4.17}$$

$$Y = 4\alpha n_\lambda k_\lambda \tag{4.18}$$

$$Q_{ext} = 2 - \frac{4sin(X)}{X} + \frac{4(1 - cos(X)}{X^2} \tag{4.19}$$

$$Q_{abs} = 1 + \frac{2e^{-Y}}{Y} + \frac{2e^{-Y} - 1}{Y^2} \quad (for\ k < 10^{-3}, Q_{abs} = 0) \tag{4.20}$$

$$w = 1 - \frac{Q_{abs}}{Q_{ext}} \quad (w \geq 0) \tag{4.21}$$

$$if\ \alpha < 1.77, \quad f = 0.5026 - 0.017\alpha + 0.1437\alpha^2 \tag{4.22}$$

$$if\ 1.77 \leq \alpha < 20,\ f = 0.8825 + 0.0318\alpha - 3.9 \times 10^{-3}\alpha^2 + 2.2 \times 10^{-4}\alpha^3 - 5.579 \times 10^{-6}\alpha^4 + 5.218 \times 10^{-8}\alpha^5 \tag{4.23}$$

$$if\ \alpha \geq 20, \quad f = 1 \tag{4.24}$$

$$g = \sqrt{(wf - 1)^2 - w^2(1 - f)^2} \tag{4.25}$$

$$k_{ext} = \frac{6M_w Q_{ext}}{4\rho d} \tag{4.26}$$

$$\tau = k_{ext} L \tag{4.27}$$

4.1.4 Suggested procedure for obtaining IR attenuation of real sprays

Rather than describing a real water spray by an average drop size, the spray is better described by a drop size distribution or by a class according to its drop size distribution. To this point, no procedure for calculating the attenuation potential of real spray distributions have been published. The radiant heat attenuation in sprays containing drops of different sizes is very complex. In order to cope with these difficulties, a very simple calculation procedure involving an imaginary separation of the real spray in monodisperse spray clouds of thickness L, equal to the thickness of the spray cloud, is suggested. This separation is performed according to the measured drop size distribution. The emissive power

of the radiating object is first passed through the first "monodisperse" spray cloud with drop diameter d_1 and water concentration M_1 given by the measured drop size distribution. This results in a slightly reduced and distorted "emissive power" $q_{\lambda 1}$, being transmitted through the "first cloud". This "emissive power" is then passed through the "second cloud" giving a more reduced and distorted "emissive power" $q_{\lambda 2}$. This procedure is repeated successively throughout the $i = 1$ to n measured drop sizes:

$$q_{\lambda(i)} = q_{\lambda(i-1)}(d_i, M_i) \tag{4.28}$$

Integration of $q_{\lambda(n)}$ over all wavelengths gives the total flux transmitted through the spray:

$$q_{tr,s} = \int_0^\infty q_{\lambda(n)} d\lambda \quad (Wm^{-2}) \tag{4.29}$$

Since close to 100% of the energy in fires is radiated at wavelengths below $30\mu m$, all integrations are done numerically from 0 to $30\mu m$. The integration step length was the same as the tabulated data by Hale et al [8]. Target reflection (R) does not exert much influence on the transmission of the spray [13] and was therefore assumed to be zero in the present work.

4.2 Results

4.2.1 Radiant heat attenuation in water films

The spectral flux distribution from a black body at 800^0C transmitted through the water film for $\gamma = 0.25, 0.5$ and 0.75 is shown in fig. 4.4(a). The water film is most transparent atshort wavelengths (Fig.4.2(a)). Since the peak of the spectral emissive power is shifted to shorter wavelengths at increasing temperatures (Fig.4.1(a)), the water film becomes more transparent with increasing temperature of the radiating surface, as seen in Fig.4.5(a).

4.2.2 Radiant heat attenuation in water sprays

Idealized spray classes

The spectral flux distribution from a black body at 800^0C transmitted through the water spray for $\gamma = 0.25, 0.5$ and 0.75 is shown in fig. 4.4(b). Since the largest fraction of the radiant heat is transmitted through the sprays at short wavelengths, the transmittance of sprays also increases with the temperature of the radiating surface, as shown in Fig.4.5(b). The fraction of black body radiation (800^0C) transmitted through water sprays as a function of path length and spray load, are shown in Figs.4.6(a) and 4.6(b), respectively.

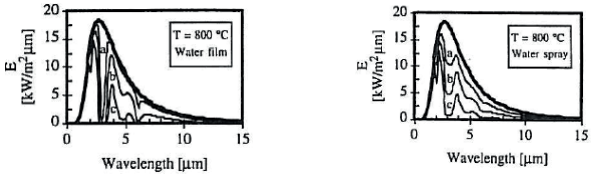

(a) (b)

Figure 4.4: Spectral flux distributions

(a) transmitted through water films,
a: $\gamma = 0.75(L = 2.6 \times 10^{-6}m)$,
b: $\gamma = 0.50(L = 16 \times 10^{-6}m)$,
c: $\gamma = 0.25(L = 64 \times 10^{-6}m)$,

and (b) transmitted through MS-SO-50 water sprays [16], [17]

a: $\gamma = 0.75(L = 0.18m, M = 100gm^{-3})$,
b: $\gamma = 0.50(L = 0.45m, M = 100gm^{-3})$,
c: $\gamma = 0.25(L = 1.06m, M = 100gm^{-3})$,

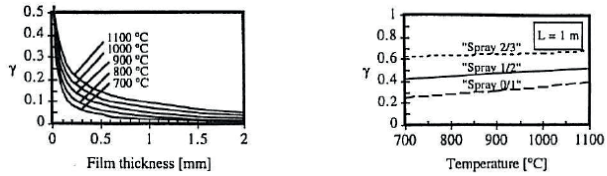

(a) (b)

Figure 4.5: (a) The fraction (γ) of the total emissive power transmitted through water films and (b) The fraction (γ) of the total emissive power transmitted through water sprays as a function of temperature

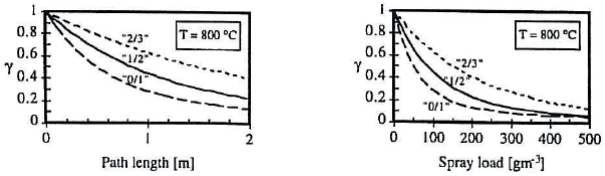

(a) (b)

Figure 4.6: (a) The fraction of the total emissive power transmitted through an idealized water spray as function of path length ($M = 100gm^{-3}$) and (b) The fraction of the total emissive power transmitted through water sprays as function of spray load ($L = 1m$)

4.3 Discussion

Applying the suggested calculation procedure for real sprays to monodisperse spray (separation into 2, 4, 8, 16, 32 groups of drop size D and spray load $M/2, M/4, M/8, M/16, M/32$ respectively) gives errors less than 3% relative to the straight forward calculations of a monodisperse spray of drop size d and spray load M. This indicates that a very small additional error is introduced when applying the suggested procedure.

4.3.1 Radiant heat attenuation in water sprays versus water films

When comparing the transmitted spectral flux distribution of water films and water sprays (i.e figs. 4.4(a) and 4.4(b)) it is seen that spray block the radiation to a large extent by scattering, evident by the lack of complete attenuation at $3\mu m$ (absorption peak of water).

Given the same radiating surface temperature (i.e 800^0C) and the same "water load", as an example a water film of $0.1mm$ thickness (fig. 4.5(a)) compared to a water spray of $100gm^{-3}$ and path length $1m$ (fig. 4.6(a)), the water film most efficiently blocks the radiant heat flux ($\gamma \approx 0.15$) for the drop sizes studied in the present work. Even the finest spray studied, Spray 0/1 ($D_{v0.1} = 50\mu m$ and $D_{v0.9} = 100\mu m$) shows close to twice this transparency ($\gamma \approx 0.28$). In order to achieve similar blocking given the same "water load", extremely small drop sizes are required.

4.3.2 Extinction mechanisms of water sprays

Blocking of radiant heat transfer is not taken into account by most researchers studying extinction mechanisms of water mists [18] [19] [20]. Without further

in depth studies, Mawhinney et.al.[10] stress the potentials of reducing thermal feedback to burning and unburned fuel surfaces by water sprays. Given a spray load of $100gm^{-3}$ and $1m$ path length, a spray on the border line between Class 1 and Class 2 ($D_{v0.1} = 100\mu m$ and $D_{v0.9} = 200\mu m$) is capable of blocking about 60% of the radiant heat from a black body at 800^0C (fig.4.6(a)). When applying high momentum spray nozzles for suppressing fires, local mist concentrations may by far exceed $100gm^{-3}$. Even at distances less than $1ft$, blocking of radiant heat transfer may therefore be an important extinction mechanism since the production of volatiles for sustained burning usually is largely dependent on radiation from the flames to the virgin fuel.

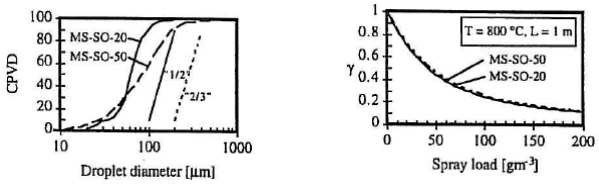

(a) (b)

Figure 4.7: (a) CPVD for the MS-SO-20 and the MS-SO-50 nozzles (measured according to ASTM E 799) [16] and (b) The fraction of the total emissive power transmitted through sprays from MS-SO-20 and MS-SO 50 nozzles as a function of spray load

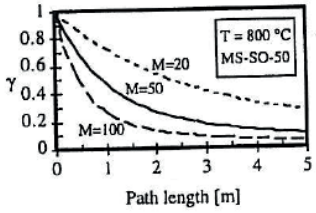

Figure 4.8: The fraction of the total emissive power transmitted through MS-SO-50 water sprays as a function of path length. ($M = 20, 50 and 100gm^{-3}$)

Chapter 5

Experimental apparatus and procedures

5.1 Experimental apparatus

The setup for producing the water curtain is shown in the GA in figure 5.1. The blue booster pump fed sea water from large pumps in the pontoon, increasing the pressure in the 6" pipe leading to the hose and the grey butterfly system. Here, 10 nozzles were mounted in a pattern most easily seen in figure 5.5. The resulting water curtain can be seen in the photographs in figure 5.6. Manometers were mounted on each side of the rig, next to the nozzle placed furthest upstream. This is shown in figure 5.7.

From each of the nozzles, a rectangular water curtain of size $10m$ height and $11m$ width was assumed, based on available data, see figures 5.2 - 5.4. The single curtain from each nozzle could overlap, and there could be any number between 0 and 5 single nozzle curtains positioned between the flame centre and a position onboard the rig. This means that the density of the water curtain varied accordingly.

For the measurements of the radiative heat flux at the defined points in figure 5.2, two identical Stefan-Boltzman radiometers were mounted onto a metal box as shown in figures 5.8 and 5.9. Inside the box was a Fluke Hydra logging unit, connected to a portable PC. For cooling the radiometers, a simple system consisting of hoses, and a bucket filled with water was attached. This was a lightweight, portable system suitable for e.g climbing stairs during the experiment. The equipment was not Ex rated, and a gas detector carried by a separate rig crew person was also a part of the "setup".

Gas and oil flow rates were Statoil property, and kindly released for this project.

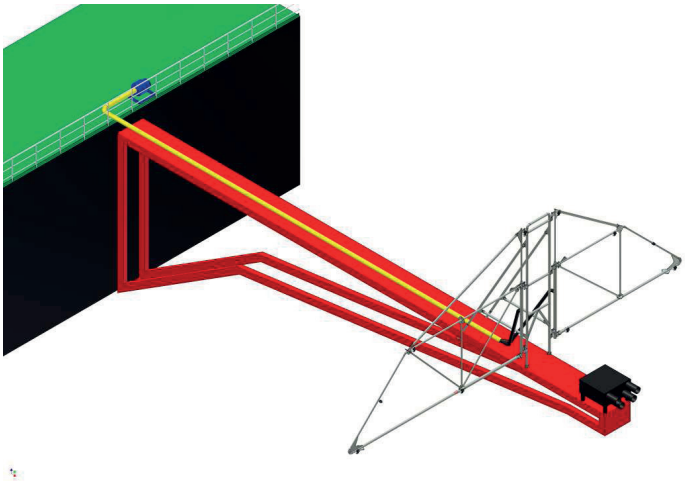

Figure 5.1: General arrangement of water curtain system. Green area is deck, blue box is booster pump being fed from large pumps in pontoons, red part is burner boom, yellow line is 6" *pipe referred to in various sections in Part III, grey lines are pipe and nozzle arrangement referred to as "butterfly", and black box at tip of burner boom are nozzles for oil and gas flow*

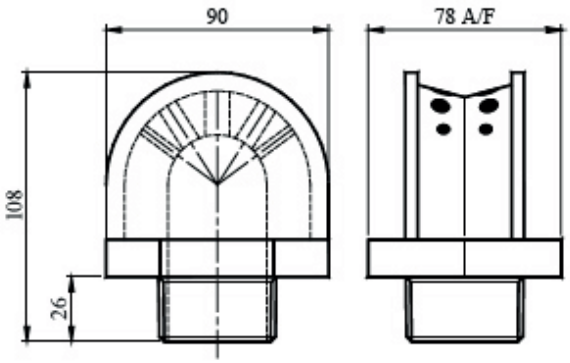

Figure 5.2: The GW nozzle with a K-factor of 260, meaning large drops and large flow compared to e.g normal sprinkler nozzles. 10 of these were mounted on starboard, and 10 on port side in the butterfly arrangement shown in figure 5.5

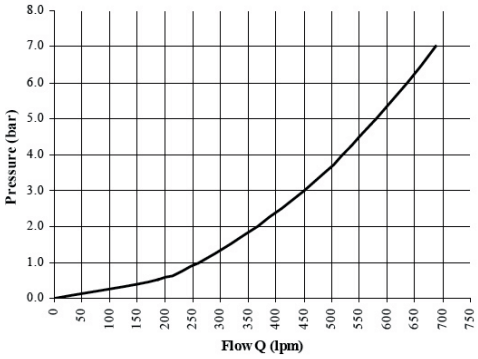

Figure 5.3: Pressure-flow curve for the GW nozzle corresponding to a K-factor of 260. $P = \frac{1}{K^2} \times Q^2$, where P is pressure measured in bar, and Q is flow measured in l/min

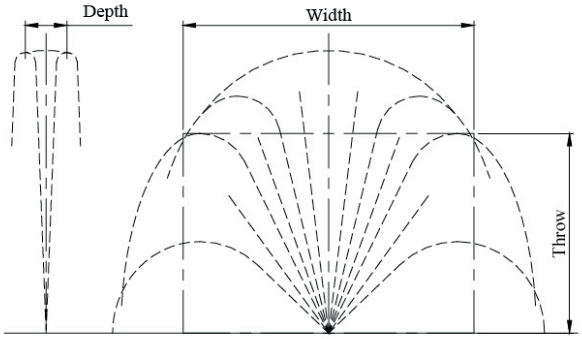

Approximate Spray Pattern Mounted Vertically.					
	1 bar	2 bar	3 bar	4 bar	7 bar
Throw	4 m	5.5 m	6.5 m	8 m	10 m
Width	8 m	10 m	11 m	11 m	11 m
Depth	0.3 m	0.4 m	0.5 m	0.6 m	0.9 m

Figure 5.4: Spray pattern for the GW nozzle as used in the calculations. The pressure during the experiment was 7.2bar for the nozzle furthest upstream. Since all nozzles were reasonably near each other, in a hydraulic sense, an average of 7bar pressure was used for all nozzles, see Appendix A. A spray pattern of 10m throw and 11m width was therefore assumed, according to the table from the manufacturer, and tests carried out onshore with no wind

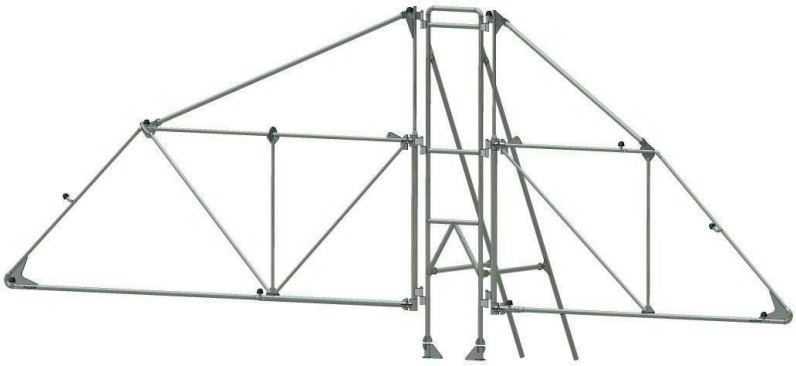

Figure 5.5: Butterfly arrangement showing position of nozzles, 5 on each butterfly wing

(a) (b)

Figure 5.6: Water curtain SB as seen from (a) ca 10m above main deck, and (b) ca 1m above deck level. Some back wind causes the water curtain to deform. The side to flare will always be chosen so that the wind will never have a direction towards the rig

Figure 5.7: Detail showing manometer position. The nozzle next to the manometer is the one furthest upstream at the butterfly

The water flow in the 6" pipe along the burner boom was measured using an ultrasonic flow meter, Polysonic DCT 7088. The meter was mounted at the straight section 7,1 m downstream of the flange connecting the hose to the pipe. This distance is $\gg 17$ times inner diameter of the pipe, which ensured a steady flow to develop before the point of measurement. Other positions were also tried, but bends, branches or nozzles disturbed the flow too much to get steady readings.

In addition, a hand held multi meter was used to obtain information of temperature, moisture content of the air, local wind conditions in the well test area etc.

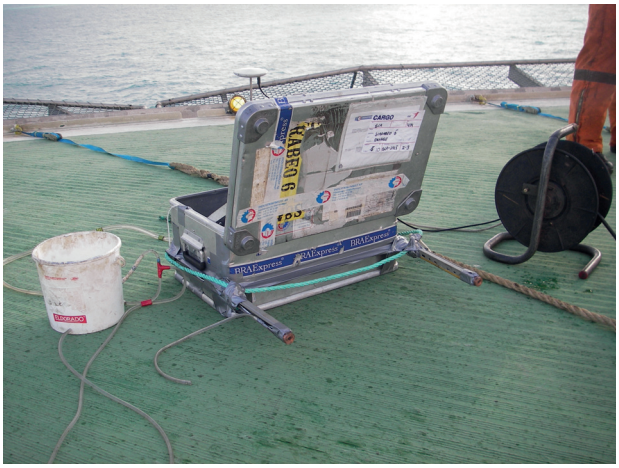

Figure 5.8: Stefan-Boltzman radiometers, range $0 - 50kW/m^2$*, for measuring radiation. The two probes can be seen mounted at each side of the box*

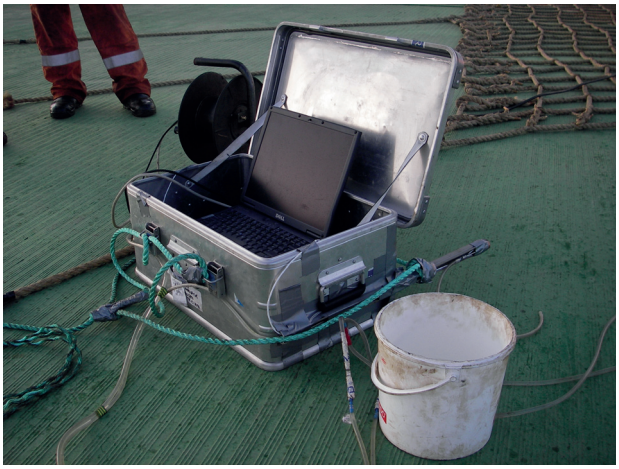

Figure 5.9: Fluke Hydra logging unit, PC, water cooling system (bucket and hoses)

5.2 Experimental procedure

Most of the job was done before the experiment was carried out. During flaring, oil and gas flow data were recorded continuously. Statoil was the owner of the information, and kindly released it for the purpose of this project.

A number of radiation data were collected at the positions shown in figure 5.2. For each position in the figure, data were logged for each $2s$ over a period of $34 - 42s$, using the portable equipment shown in figures 5.8 - 5.9. The results were averaged over the measurement period. All radiation data were collected within the period 17:52 - 19:58 at May 31^{st}, 2006.

After flaring, weather data were collected from the recording system onboard the rig.

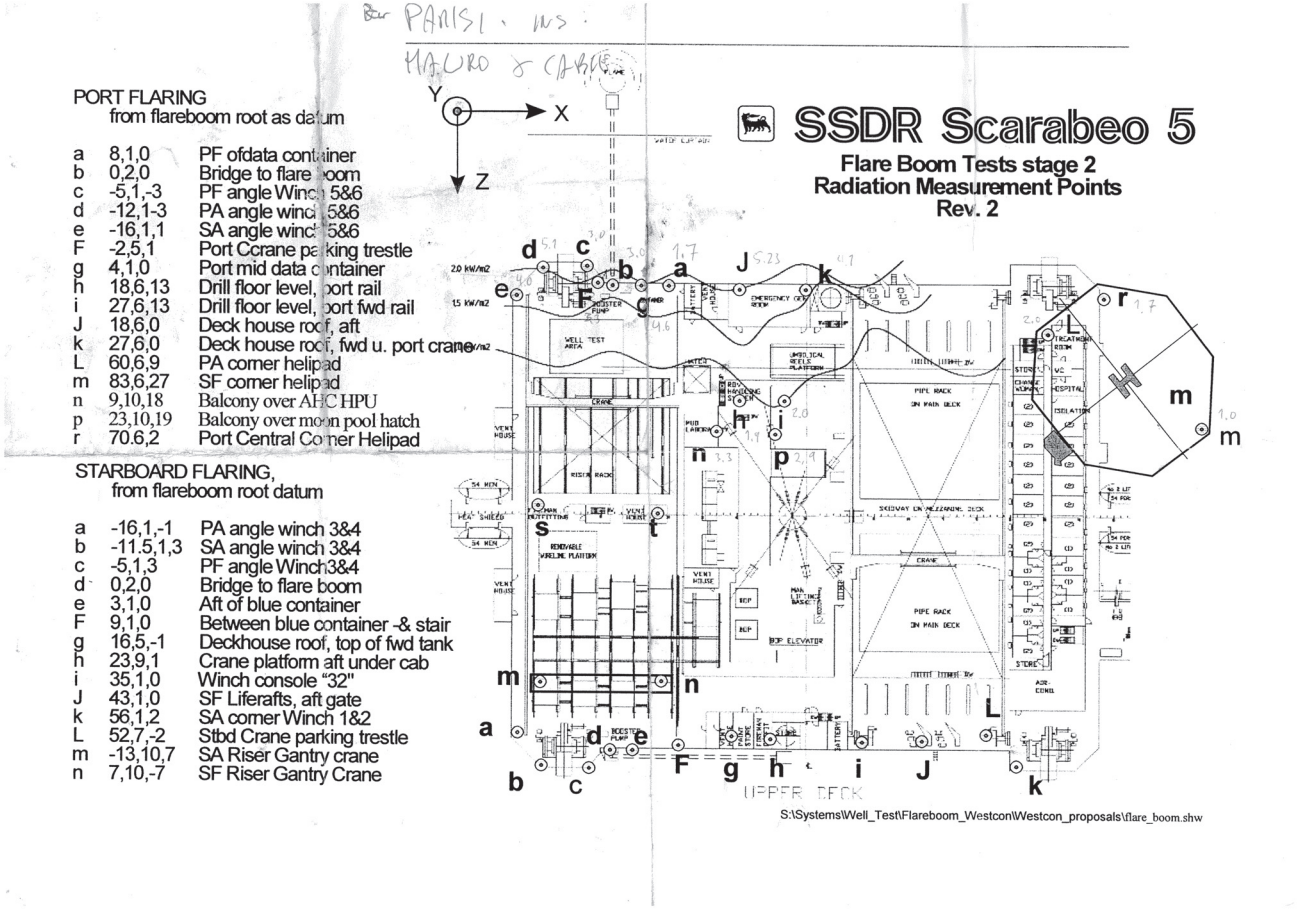

Figure 5.10: Plan of the measuring points for heat radiation. Only the positions in the top half of the figure were used, since flaring was carried out at port side

Chapter 6

Results

6.1 General

In this project, several factors affected the heat radiation from the flare onto the rig. In the start, all of them were calculated from best guess estimates. This included the oil and gas flows and radiation from the flare, the geometry of the flare, the pump/pipeline capacities, the nozzle characteristics, and finally, the heat attenuation properties of the water curtain. All of these were considered in a preliminary report. However, the object has been to find out if the applied heat attenuation theory can give a good estimate of the *real* heat attenuation in the water curtain. Therefore, it has been necessary to do the calculations of the heat attenuation after flaring, when the flare geometry, actual water flow etc had been measured. Only this way, a comparison between the applied theory for heat attenuation and measured results can add information regarding the reliability of the theory applied to a real full scale situation.

For the ease of reading this chapter, images from the experiments are presented first. The basis for carrying out the calculations and measurements are then presented in sections 6.2 and 6.3 to give a thorough background for the comparative results shown in section 6.4. Special attention is drawn to figures 6.15 and 6.16, showing the radiation at deck level. The plots are in the form of iso radiation contours. These two figures provide the largest number of measurement points for comparison. Measurements were also taken at higher elevations, but there were too few data to make separate contour plots possible.

(a) (b)

Figure 6.1: Water curtain seen from port FWD. Note the umbrella shaped water curtain. The reasons for this shape, are wind partly blowing away from the rig, and the buoyancy effect of the flare plume (HRR = 1890MW)

(a) (b)

Figure 6.2: Water curtain seen from port FWD. The experiment showed that the flare and the water curtain co followed the wind, as can be seen in several of these photographs. This means that the drop sizes were fairly well suited for the purpose, flow wise. Heat attenuation wise, it would be preferred to use smaller droplets

The photographs presented at these two pages, are all taken during the final experiment. They show how different images can be, by varying the exposure.

(a) (b)

Figure 6.3: Water curtain seen from port centre. All ten photographs in these two pages are from the same experiment

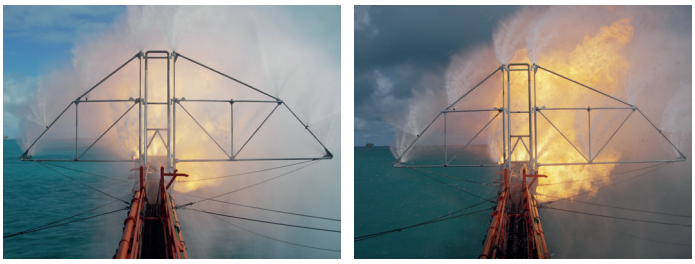

(a) (b)

Figure 6.4: Water curtain seen from root of burner boom

(a) (b)

Figure 6.5: Water curtain seen from port aft

6.2 Basis for measured results

6.2.1 Measured oil and gas flow rates

The flaring was carried out over a time span of 7-8hrs. As can be seen from figure 6.6, it took $\approx 5.5hrs$ to stabilize the oil and gas flows. Therefore, the measurements started a little less than $6hrs$ after the flaring started. At this point, the flow had become fairly stable, at $1380m^3/d$ oil flow rate, and $\approx 1,290,000STD\ m^3/d$ gas flow rate. This flow rate was close to one of the scenarios in the Flaresim simulations, which made it possible to do a reliable comparative study.

It should be noted that even during the test period, the flow varied to some extent, and there were one major and two minor drops in the oil flow rate. However, since a jet fire has close to zero inertia, this was not considered a problem. It can be seen from figures 6.7 - 6.9 and table 6.1 that each single measurement was carried out at fairly constant flow rates, both for oil and gas.

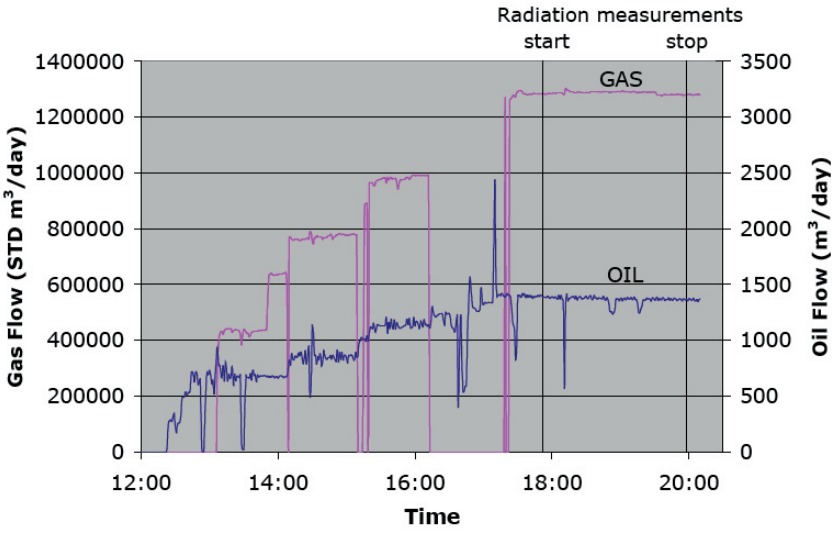

Figure 6.6: Flow rates for entire period of flaring. All measurements were carried out in the time span 17:52-19:58. As shown, there were one major and two minor drops in the oil flow rate in this period. None of them occurred during the actual measurements. Since jet fires have close to zero inertia, it was assumed that these drops in flow rate had no impact on the measurements

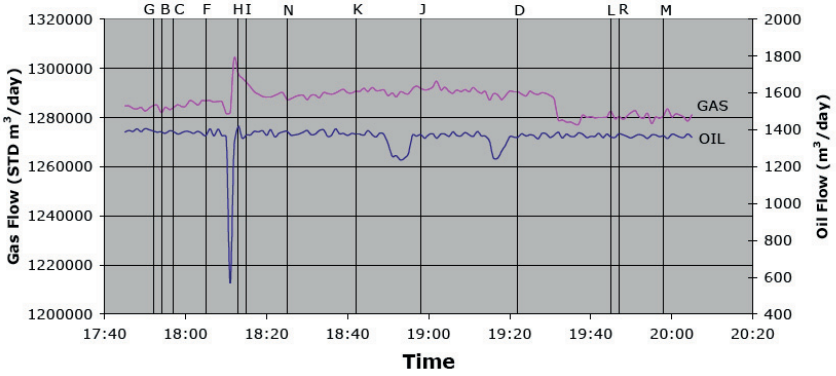

Figure 6.7: Flow rates for each specific point, mainly corresponding to the two vertical "start" and "stop" lines in figure 6.6. The letters at top of the diagram refer to the measurement points shown in figure 5.2. Note that the flow rate scales (y-axis) do not cross the x-axis at pt (0, 0). Some variations in flow rates can be observed. The rates are shown in table 6.1

Table 6.1: Oil and gas flow rates during flaring. The letters refer to the recording positions shown in the plan view of the rig in figure 5.2. The time was noted for each single radiation recording, in order to find the exact flow rate at that specific time. The table shows that there were stable oil and gas flow rates. In the "Deviation" columns, at the "Average" line, the standard deviations for the oil and the gas flows are listed. Note that these deviations were small, 1.2% *and* 0.4% *of the flow rates for oil and gas, respectively. The measurements were carried out at the Kristin field in the Norwegian Ocean, May 31. 2006, at the times stated in the table*

Position	*Time*	*Oil flow rate* (m^3/d)	*Deviation oil*	*Gas flow rate* ($STD\ m^3/d$)	*Deviation gas*
G2	17:52	1395	14	1284913	-2344
B2	17:54	1390	9	1282078	-5179
C2	17:57	1391	11	1284023	-3234
F2	18:05	1367	-13	1286874	-383
H2	18:13	1419	38	1297816	10559
I2	18:15	1373	-7	1294335	7078
N2	18:25	1393	13	1287304	47
K2	18:42	1376	-4	1290726	3469
J2	18:58	1374	-6	1291897	4640
D2	19:22	1359	-21	1290505	3248
L2	19:45	1361	-19	1282491	-4766
R2	19:47	1379	-2	1280478	-6779
M2	19:58	1368	-12	1280895	6362
Average		**1380**	16 **(=1.2%)**	**1287257**	5246 **(=0.4%)**

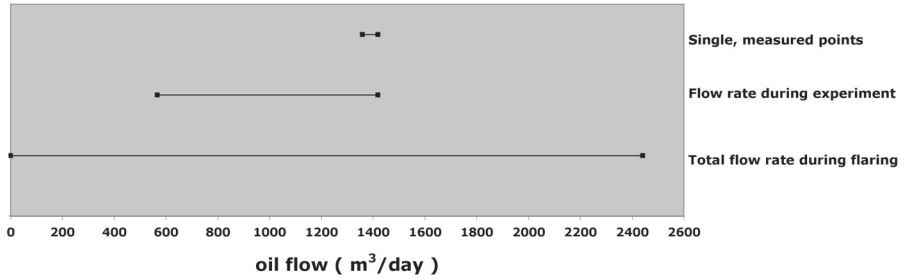

Figure 6.8: The measured rates during flaring. A complete set of data is shown in figure 6.6. The flow varied much throughout the period of flaring. The oil flow rate was in the range $0 - 2,441 m^3/d$. *However, in the period between the first and last measurements, this range narrowed down to* $567 - 1,419 m^3/d$. *This is also shown in figure 6.7. The actual measurements at separate points in time, narrowed the range even further down, to* $1,359 - 1,419 m^3/d$. *The average rate, used in the calculations, was* $1,380 m^3/d$ *The flow rate could be characterized as "stable" in the sense that the standard deviation was* 1.2%. *This is shown in table 6.1*

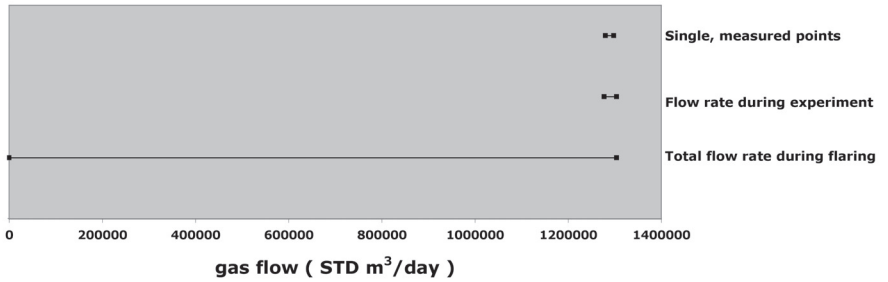

Figure 6.9: The measured rates during flaring. A complete set of data is shown in figure 6.6. The flow varied much throughout the period of flaring. The gas flow rate was in the range $0 - 1,304,046 STD\ m^3/d$. *However, in the period between the first and last measurements, this range narrowed down to* $1,277,282 - 1,304,046 STD\ m^3/d$. *This is also shown in figure 6.7. The actual measurements at separate points in time, narrowed the range even further down, to* $1,280478 - 1297816 STD\ m^3/d$. *The average rate, used in the calculations, was* $1,290,000 STD\ m^3/d$. *The flow rate could be characterized as "stable" in the sense that the standard deviation was* 0.4%. *This is shown in table 6.1*

6.2.2 Measured water flow rates

The water flow rates for different uses of pump and valve opening combinations were measured by an ultrasonic flow meter, mounted to the 6" pipe along the

burner boom. The relevant measured water flow rate during flaring was $75.6l/s$, see appendix A. Although this rate was measured at an earlier stage, no changes were made to the setup between the time of measurements and time of flaring.

6.3 Basis for calculated results

It is important to point out that the calculations have been based on measurements of the water flow and flame size, and simulations of the radiation from the flare. This means that only the *heat attenuation* has been calculated. It is clear that if the heat attenuation calculations should be based on the theoretically calculated flow, and the measured heat attenuation based the real flow, the comparison would not make sense.

The water curtain system was designed to have the densest cover in the well test area at the root of the burner boom. Therefore, the nozzles were placed in a manner to provide as large overlaps as possible between the flame centre and the well test area.

The average pressure drop through the nozzle furthest upstream was $7.2bar$. Since the nozzles were placed at non reachable positions at the butterfly, it was not possible to measure the pressure drop through each individual nozzle. Therefore, the water flow through the 6" pipe along the burner boom was measured directly, showing a flow of $75.6l/s$, and resulting in an area-density (path length times density) of $0.18kg/m^2$. The area density was found by a combination of calculating the detention time for water falling freely after leaving the nozzle, the volume flow of water through each nozzle and the geometry of the water curtain.

Even though some of the nozzles were positioned at the upper part of the butterfly, an undisturbed volume fraction of the flame could be viewed from some positions onboard. Therefore, the volume fraction not covered by the water curtain, was estimated, and the radiative heat from this part was added for the positions where this occurred.

The calculated results were based on a number of assumptions:

1. There was no contribution from the rig side cooling system
2. 70% of the water volume consisted of $1mm$ dia.drops, and 30% consisted of $0.5mm$ dia.drops
3. There was no absorption done by water when it was positioned below the nozzle it had departed from
4. All the water within its rectangular coverage area (ref. spray pattern, figure 5.4) went up and down within its rectangular "boundaries"
5. The flame height during flaring was $22m$. The centre of the flame was $38m$ out from the rig side, and $11m$ above deck level (in accordance with measurements from photographs).
6. There was a partial view of the flame, above or to the side of the water curtain from various locations at the rig. The view fraction increased with height, especially at 20 m above deck level.

7. All nozzles were assumed to provide the same water curtain size and density.

Comments to the assumptions:

1. Saipem was required to minimise surface spraying. Thus, the calculations were made for supply of water to the flare boom cooling only.

2.-3. Assumptions were discussed with prof. Log, one of the leading experts in the field, and found reasonable. Although the drop size distribution clearly was not exact, they were expected to give reasonable estimates of the absorption. It was as good as it could get with our (lack of) knowledge of drop size distributions and experiments in the field.

4. Apparently wrong, but two neighbouring nozzles would feed each other with water, such that the assumption is fairly accurate, especially in the middle sections

5. Estimates of flame height and position were based on measurements from photographs taken during flaring

6. The flare *volume* fraction was estimated, rather than the *area* fraction, since a thick flame has a larger emissivity than a thin flame.

7. This assumption was a simplification that was found necessary and as close as practically obtainable. See chapter 7 for a more detailed discussion of this assumption.

As mentioned in chapter 3, the least water consuming solution to provide sufficient cut in radiant heat, was to increase the blocking capacity of the first barrier on the flare boom, i.e the water curtain. According to Schlumberger, the flare boom spray shield on Scarabeo 5, before the new butterflies were mounted, cut 50% of the radiant heat which occured while flaring. Since heat attenuation in water sprays does not follow a simple Beer-Lamberts law, a doubling of the spray capacity of this shield will result in a little less than 50% additional relative cut in heat radiation. Based on the assumption that most of the mass of the water spray consists of droplets larger than $0.5mm$, and taking into account that both absorption and scattering is dependent on wavelength, doubling the spray curtain capacity will result in $\approx 46-47\%$ additional relative cut in radiant heat. Calculations made by Log [21], presented here in tables 6.2 and 6.3 show this. Based on these tables and an assumed drop size distribution of 70% $1mm$ dia. drops, and 30% $0.5mm$ dia. drops, a diagram was made, showing the heat attenuation fractions for the actual water curtain, used for the actual flow rate, as a function of the *coverage*.

Coverage: By close inspection of the geometry of the water curtain from each individual nozzle, and the flame shape, each position at the rig could be regarded as covered by "n" individual water curtains. The combined heat absorption and scattering could then be calculated in accordance with figure 6.10. If the line between the flame centre and a point at the rig ran through the water curtain from one single nozzle, the coverage was 1, if it ran through the water curtains

from two nozzles, the coverage was 2 and so on. This is shown in figure 6.10. Note that the results were computed for the actual, measured water flow.

In addition to the coverage, most points on the rig had a direct view to a part of the flame. Undisturbed radiation from the volume fraction of the flame not covered by any water curtain, could be estimated. Thus, the total radiation from the flare, onto any point of the rig, was regarded as the sum of the radiations from the covered and the undisturbed view of the flare. The results from calculations are shown in figures 6.10 - 6.15 and 6.17 - 6.18.

The ambient sunlight was not taken into account, a factor varying from ≈ 0 (dark night), to $\approx 1.0kW/m^2$ (bright daylight in summer).

Table 6.2: Required area-density (path length times density) of mono disperse water spray to achieve 50% cut in radiant heat from a black body source at 1100^0C*. From Log [21]*

Drop size	$1.0mm$	$0.5mm$	$0.1mm$
Area density	$0.537kg/m^2$	$0.295kg/m^2$	$0.084kg/m^2$

Table 6.3: Further relative cut in radiant heat from a black body source at 1100^0C *at double are-densities (path length times density) from table 6.2. From Log [21]*

Drop size	$1.0mm$	$0.5mm$	$0.1mm$
Area density	$1.074kg/m^2$	$0.590kg/m^2$	$0.168kg/m^2$
Cut	47%	46%	38%

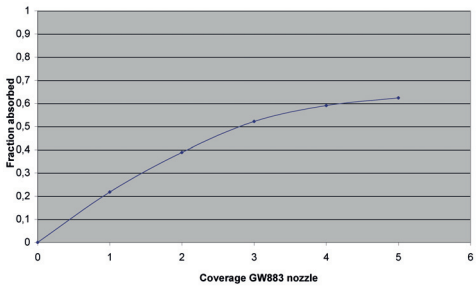

Figure 6.10: Calculated heat absorption. The coverage at the x-axis denotes how many nozzles whose water spray covers the line between the flame centre and the position in question. Note that the numbers apply to the actual measured water flow in through the nozzles. The measured flow was 63% of the calculated. The reason for a reduced actual flow was mainly due to less capacity of the pumps and pipes upstream of the booster pump

6.4 Main results visualized

In this section, the main findings in the project are presented in the form of plots that reveal the main features of the water curtain properties in a visual and easy to read form. Firstly, figure 6.11 shows the radiation along the rig side with no water curtain from the Flaresim simulations, compared to the similar calculated value. The calculated values produce a more flat curve due to a denser water curtain in the areas where the flare causes the largest radiative load. This was intentional, since there is a lot of fragile equipment and personnel positioned in this area during flaring. In this period, there was a constant $6m/s$ wind from aft. Since flaring was carried out at port side, this was a cross wind.

In figure 6.12, a comparison has been made between the radiation at different levels with the water curtain present. Unfortunately, the geometry of the rig only allowed a verification of the calculated results to be carried out at deck level. At higher levels, it was not possible to access a sufficient number of measuring positions. At elevation $20m$, the radiation was only slightly higher than the radiation at $15m$. At these elevations, the coverage was the same (i.e the water curtain from the same number of nozzles covered the two elevations), but a slightly larger view of the flame caused this difference. Similar observations were made for elevations $0 - 10m$. Note that the curve "With water curtain" in figure 6.11 is the same as the curve "elevation 0m" in figure 6.12.

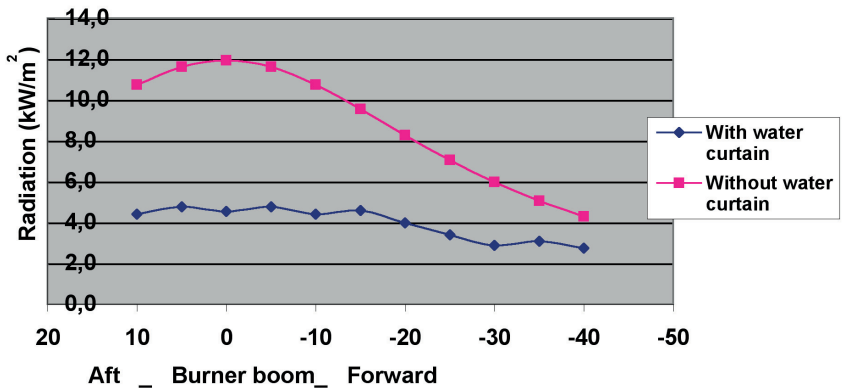

Figure 6.11: A comparison between radiation onto the side of the rig facing the flare, for flaring with no water curtain (from Flaresim calculations), and the calculated values (for the actual measured water flow in the curtain). The numbers along the x-axis denotes the eastings, measured in metres. Note the flat curve for the water curtain case. This is due to a denser water curtain covering the well test area

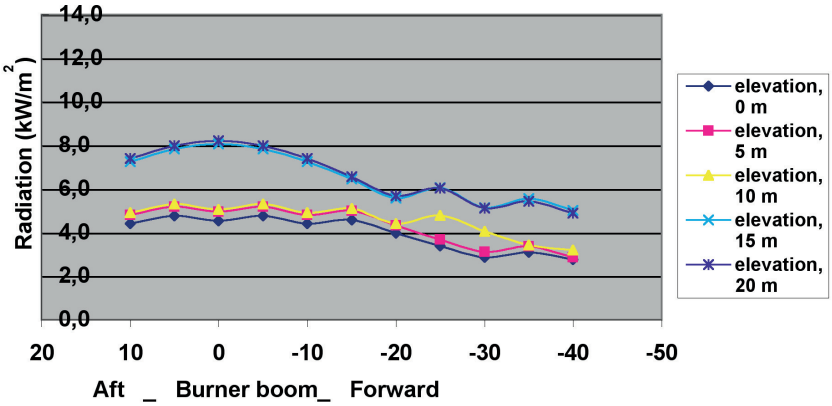

Figure 6.12: Radiation at different elevations, based on the Flaresim calculations for radiation, and calculated values for the actual measured water flow in the curtain. The numbers along the x-axis denotes the eastings, measured in metres. From 15*m and above, the coverage is very limited, and the radiation varies only marginally with elevation*

In the following pages, iso radiation contour plots have been made in order to show the radiative calculated and measured loadings both in plan and elevated views. The plots show loadings both with and without the water curtain present. All radiation from the flare is calculated using Flaresim. All iso contours are made using the calculation model shown in chapter 4.1, summarized in section 6.3, except for the measured values in figure 6.16. These results were obtained by radiometers.

In figures 6.13 and 6.14, plots are shown, showing the radiation levels during flaring, when no water curtain was present. This is for illustration only, and due to the high radiation levels, the situation had to be avoided. The plots were made in order to compare with the results for the presence of the water curtain.

The only direct comparison between the calculation model and measured results, can be found by comparing figures 6.15 and 6.16. These two figures represent the main findings of this project. As the figures show, the measured results showed slightly better absorption properties than the calculated. This is discussed in chapter 7. In addition, the uneven distribution of water can easily be seen for the measured results. This is shown by the irregular iso radiance curves. The calculated results, based on water droplets evenly distributed within a number of rectangular shaped water curtains, does not show this feature. Still, there are some irregularities even for the calculated plots. These come from the varying views of the undisturbed volume fraction of the flare.

In the final two plots, figures 6.17 and 6.18, iso contours have been presented for levels 10*m* and 20*m* above deck, respectively. The situation in these two cases are for flaring and the water curtain present. As explained, it was not possible to obtain measured values, due to lack of access to a sufficient number

of measuring positions. However, it was of interest to find out how efficient the water curtain was at these levels. These plots can be compared to the radiation levels in the no water curtain case in figure 6.14. Even though this plot is for deck level, one can see from the section view in figure 6.13, that the radiation with no water curtain only varies marginally for a given distance, between levels $0 - 20m$.

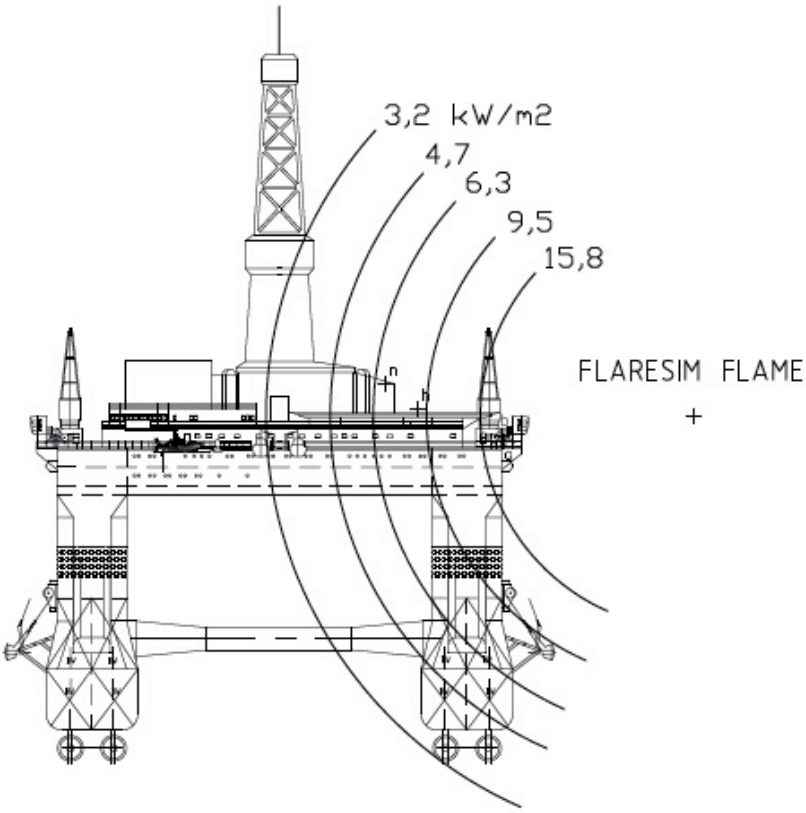

Figure 6.13: Heat radiation, transverse sectional view, no water curtain, Flaresim calculation. It can be seen that the radiation, undisturbed by a water curtain, is close to constant for a given distance away from the flare, in the range $0 - 20m$ *above deck level. Point "n" is at level* $10m$*, and illustrates this point*

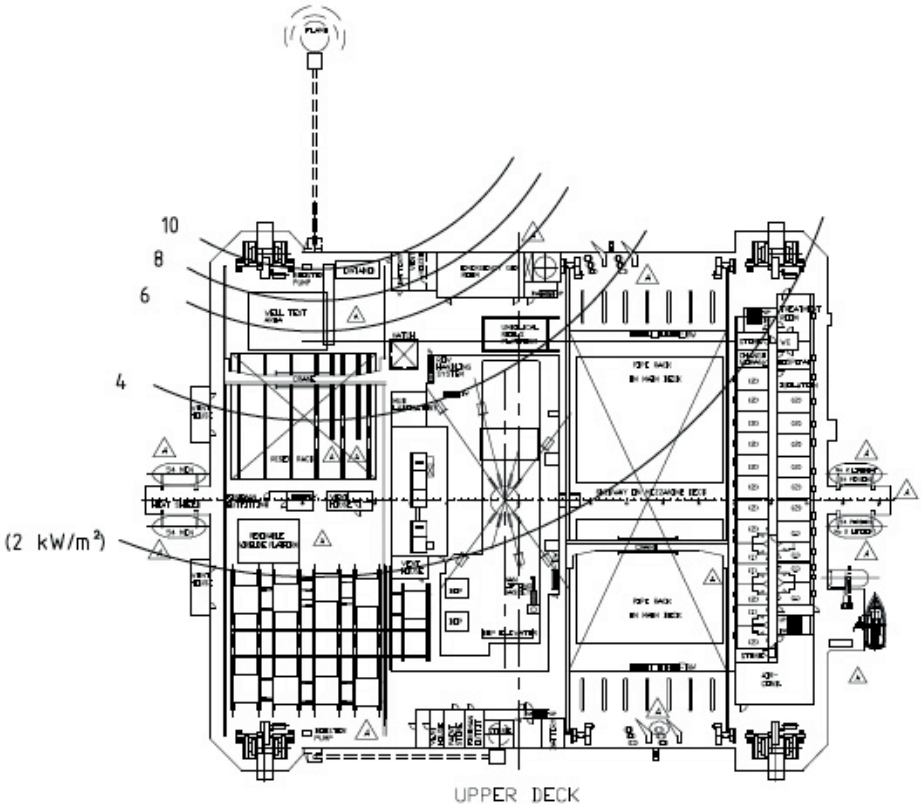

Figure 6.14: Heat radiation at deck level, no water curtain, Flaresim calculations. Note the radial shape of the contours, and the increasing distance between equal radiation increments of $\Delta \dot{q}_r'' = 2kW/m^2$. *The reason for this, is that the radiation decreases approximately with the square of the relative increase in distance r. The reason for putting the* $2kW/m^2$ *iso unit in a bracket, was that most of this line is beyond the centre line of the rig. This means that when flaring from the opposite side, the radiation levels will increase*

Since the exact drop size distribution was not known, the sensitivity to a varying distribution was calculated. The original assumption was a drop size distribution of 70% $1mm$ dia. and 30% $0.5mm$ dia. drops. Calculations were performed for 1. a 50% increase in drop size (i.e 70% $1.5mm$ dia. and 30% $0.75mm$ dia. drops) and 2. a 100% increase in small droplet fraction (i.e 40% $1mm$ dia. and 60% $0.5mm$ dia. drops), keeping the flow rate constant. The flow rate was kept constant, since it was measured. The calculations showed that the

sensitivity varied with the coverage, i.e the number of nozzles covering a specific point, and situation 1. or 2. The calculations showed that in the worst case, the absorbing capacity of the water curtain would be reduced by 7%, absolute value. This is the case with larger drops, and for a coverage of 1 nozzle. In the opposite end, where a double fraction of smaller drops were covered by 5 nozzles, the calculations showed that an increased absorbing capacity of 18% absolute value, would be expected.

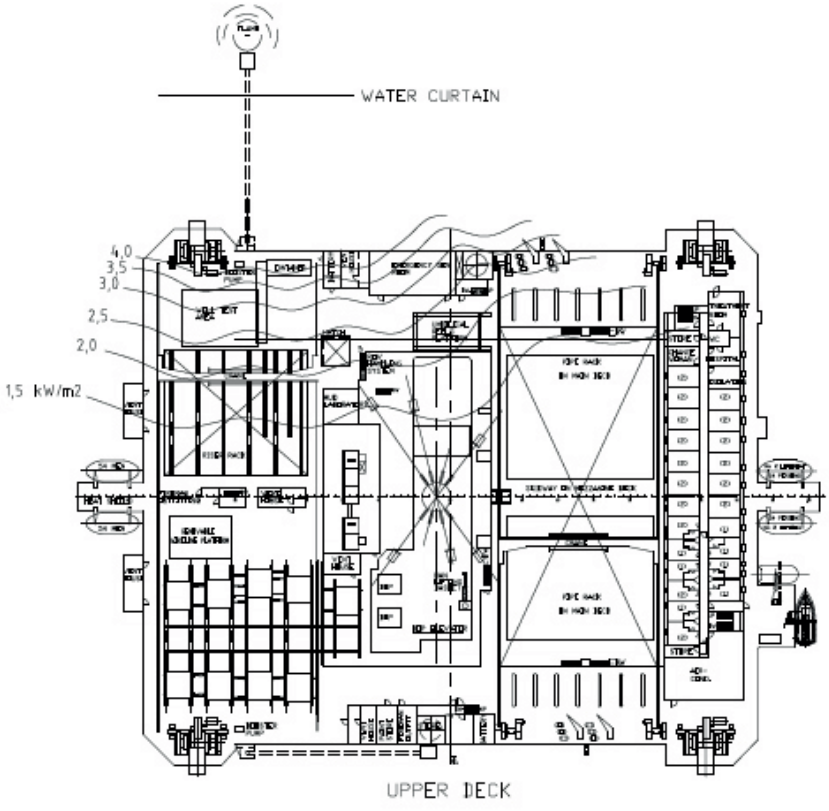

Figure 6.15: Heat radiation at deck level, with water curtain, calculated values. The reason for the wave shaped iso contours is that there is a varying number of nozzles covering each position, and a varying fraction of undisturbed view towards the flame for the different positions

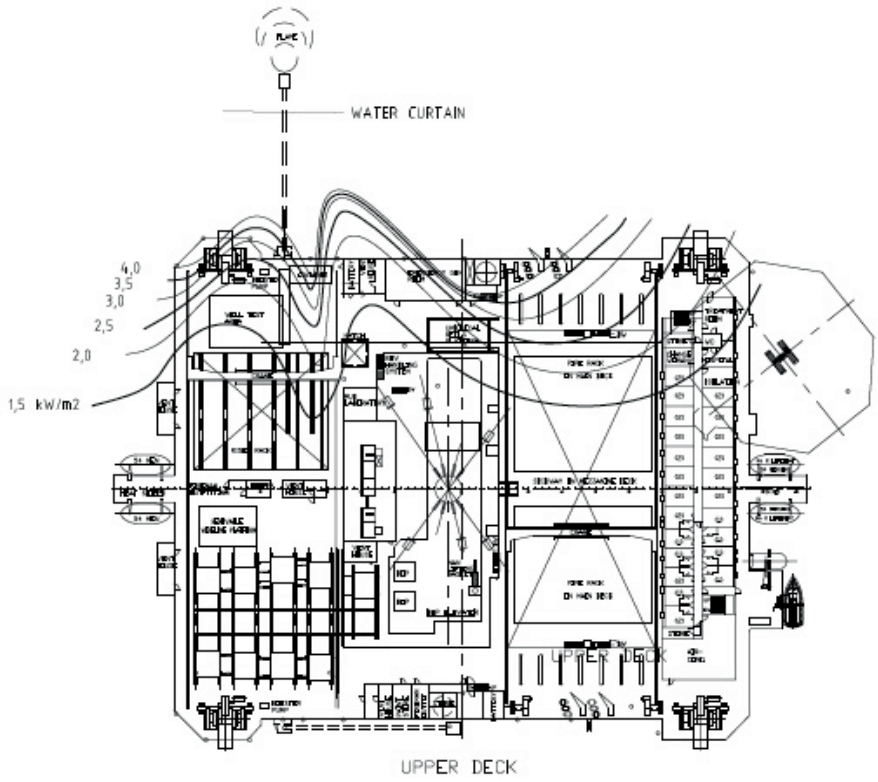

Figure 6.16: Heat radiation at deck level, with water curtain, measured values. As for figure 6.15, the reason for the wave shaped iso contours is that there is a varying number of nozzles covering each position, and a varying fraction of undisturbed view towards the flame for the different positions. However, there is an additional feature, causing the contours to vary even more than in figure 6.15. This is the effect from the uneven water curtain produced by each nozzle. This effect is not accounted for in the calculations

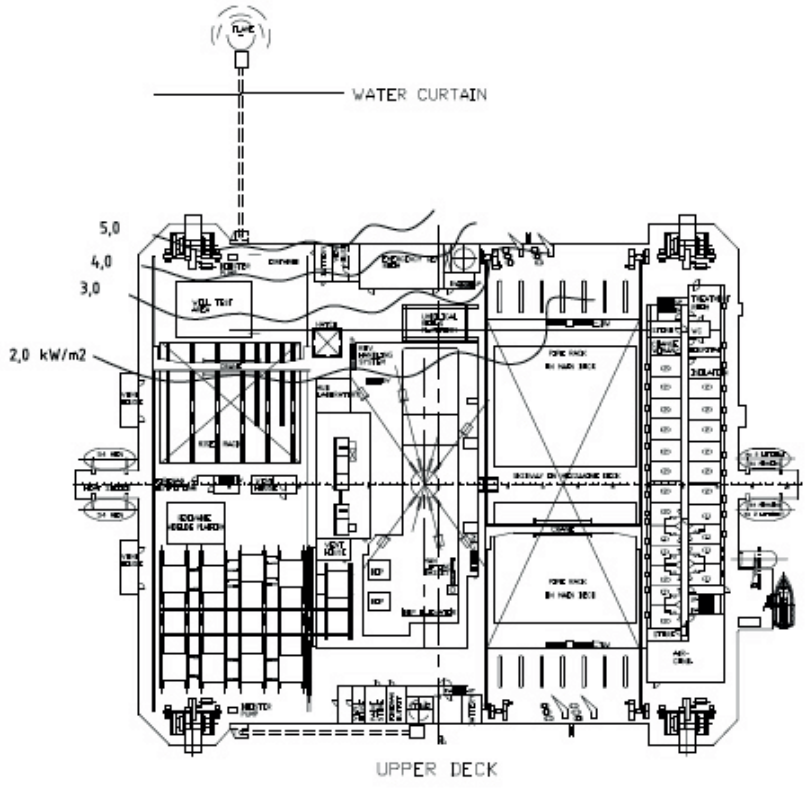

Figure 6.17: Heat radiation at 10*m above deck level, with water curtain, calculated values. Values from these plots can be compared to the values at deck level, with no water level present, for efficiency estimates. The reason is that the undisturbed radiation varies only marginally with elevation, as can be seen in figure 6.13*

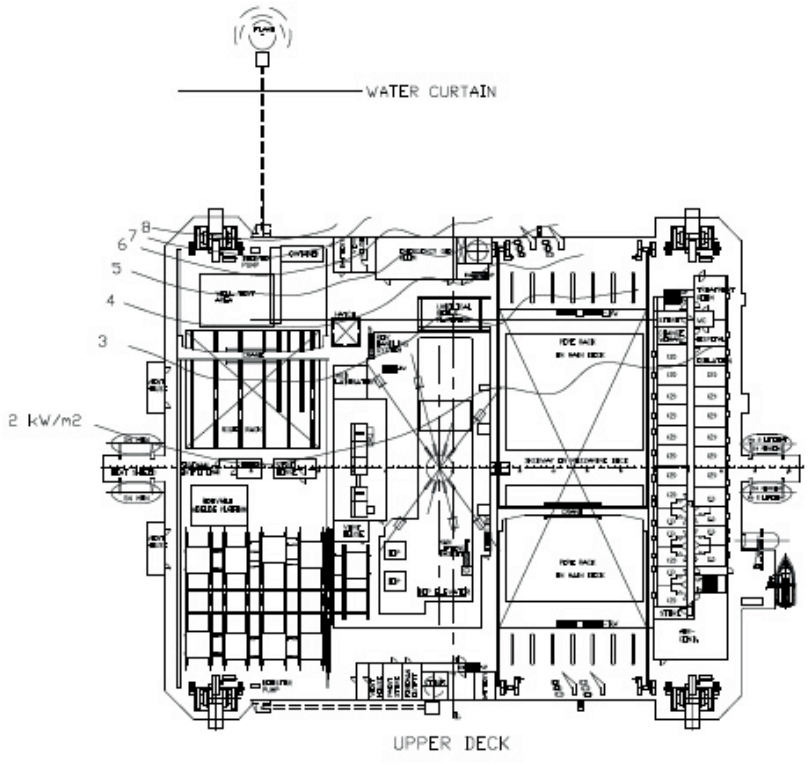

Figure 6.18: Heat radiation at 20*m above deck level, with water curtain, calculated values. As for figure 6.17, values from these plots can be compared to the values at deck level, with no water level present, for efficiency estimates. The reason is that the undisturbed radiation varies only marginally with elevation, as can be seen in figure 6.13*

Chapter 7

Discussion

7.1 Some practical aspects

In this project, no fundamental laws of heat attenuation have been challenged. This has not been a topic. The focus has been on the application of some of these laws in a real full scale flare situation, to see if it is meaningful to apply the theory to these kinds of situations. The project was influenced by the fact that the main activity in the critical phase when flaring, was *not* to run this project, but to collect data from an oil and gas well. In addition, main safety issues, such as not exposing the rig to unwanted levels of radiation, limited the opportunity to measure radiation for e.g a reduced, or non existent, water curtain. Therefore, the project has implied very much work in order to obtain only a few data.

With the exception of radiometer and logging devices, the complete setup was dictated by the focus on the well test. The situation gave some advantages and some disadvantages compared to a laboratory setup:

The main advantage was that the project gave access to a full scale situation. Although building a test site of these dimensions would be the best for collecting data, it would not be realistic.

The disadvantages were the lack of control of the factors involved, i.e no experimental control of oil and gas flow, meaning that e.g the access to data for varying flow, and therefore radiation conditions, were not possible. One obvious problem of running an experiment offshore, was the wind. As discussed earlier, problems with strong wind causing the small droplets in the original water curtain to blow sideways was a major challenge. However, for the new water curtain, this turned out to be less of a problem than expected:

The influence of the wind on the oil and gas flames was significant, especially at the downstream ends, where most of the momentum was lost. But the upward moving plume caused by the flare itself, tended to stabilize the conditions. With a heat release rate of $1890MW$, the resulting air expansion and buoyancy effect caused the water to form a stable, umbrella shaped curtain partly surrounding the flame. All these effects combined, caused the water curtain and the flare to follow each other closely, as the wind changed. The photographs in figures 6.1 - 6.5 illustrate this.

An obvious weakness of the project, has been the limited description of

the water curtain. The drop size distribution was not measured. High speed photography of droplets at different sections within the water curtain from a single nozzle was performed onshore. This resulted in images not suited for assessing neither drop speed, size distribution nor total coverage. Therefore, no results from this part has been reported, and assumptions had to be made instead, see section 6.3. This also applied to the shape of the water curtain from each nozzle.

The photographs in the beginning of chapter 6, especially the two in figure 6.5, are examples of non uniform shaped water curtains. There were individual sprays from each hole in the nozzles, some areas close to the side of the nozzles were not covered at all (nozzles at bottom line, the upper nozzles are covered from the lower nozzles), and the shape of the water curtains were not rectangular. All nozzles were assumed to produce the same water curtain, although they were placed at different elevations and at different positions along the supply pipes. These were simplifications that were found necessary in order to reach a result when performing the calculations.

There were a lot of factors affecting the water curtains. The side wind of $6m/s$ can have caused the smaller droplets to blow out of the defined area faster than the larger. The fan shaped nozzle hole arrangement complicated the calculation of the detention time for each droplet within the curtain. Also, an estimate of the view from any point towards the undisturbed volume fraction of the flame, was based on drawing the flame and water curtain, and approximations of the fractions based on this. These are all possible error sources.

The total flow through the nozzles were measured using a high quality flow meter. Therefore, it was possible to achieve an accurate total volume rate of water that was supplied to the water curtain. The flow was stable throughout the experiment, see subsection 6.2.2 for more details.

In addition to the limited description of the water curtains, it was assumed that the Flaresim calculations were correct. In a laboratory facility, the radiation from a flare not covered by a water curtain would be measured. Due to the significantly reduced safety caused by an action like that, it was not possible to do so in this experiment. However, validation of the Flaresim model for similar situations, have shown good accuracy, see subsection 3.3.1 for more details.

Waiting for a stabilization of the flow was essential to the experiment. This was advised by the rig personnel, and caused all measurements to be taken towards the end of the flaring, Therefore, the oil and gas flow rates varied only marginally through the measurements. This caused a stable radiation load on the water curtain, see subsection 6.2.1 for more details.

7.2 Heat attenuation in water curtains

Light (and IR attenuation) traveling through most semi transparent media is reduced in intensity in accordance with the Beer-Lamberts law, the relative reduction in radiation intensity traveling at length L equals the relative reduction for each new path length L.

In water spray shields, heat will be attenuated by both absorption (extinction) and scattering (diffusion) due to the water droplets. The interaction between light and particles (droplets) for water, where both the absorption coefficient and refraction index is dependent on wavelength, is rather complex. The

reduction in radiation intensity therefore does not follow a simple Beer-Lambert law approach [21].

When traveling through a water spray, the radiation at some wavelengths may be reduced to zero. Increasing the path length through the water spray, or increasing the spray density, will therefore not contribute in further reduction at these wavelengths. The over all reduction in radiant heat intensity by increasing the path length, or increasing spray density, will therefore be less than estimated by a simple Beer-Lambert law approach. In order to fully estimate the radiant heat intensity, a calculation procedure as explained in chapter 4.1 should then be performed [21]. However, in this experiment, this was not a problem, see subsection 7.3 below.

7.3 Treatment of calculations and observations

In this experiment, the combined density and path lengths were mainly within the 50% and the following $46 - 47\%$ double path length reductions as shown in tables 6.2-6.3. Only the positions covered by individual water curtains from 5 nozzles at the same time, the double path length limit was exceeded. This applied to 3 of the 55 separate positions that were calculated. In all cases, the curve in figure 6.10 was used, and that implied a short extrapolation of table 6.3.

By simple geometry, behind the water curtain, the radiation intensity was assumed to be reduced with the inverse of the square of the radius. Some additional reductions would be present due to water vapor and CO_2 absorption and scattering. This effect could be neglected, since the path length was tenths of meters rather than thousands.

Regarding the observations, an mV signal from each of the radiometers were translated into a kW/m^2 value in accordance with the calibrated values of the instruments. Since two radiometers were mounted, each pair of readings was averaged to find the radiation at any point.

7.4 Potential applications of the model

one of the objects of this work was to present a verified model for engineering use. This meant that the model should be used either directly, or with adjustments. As can be seen in the iso radiance plots in figures 6.15 and 6.16, there is small difference between the calculated and the measured results. The calculation model used in this experiment, should not be applied in general without further verification, due to the inaccurate description of the water curtain properties. This leads to the need for more measurements before a verified model can be presented.

Chapter 8

Conclusions

This project has applied a known heat attenuation model to a full scale flare situation, where the model predictions have been compared to measured values during flaring, in order to find out if the model was suited for this purpose. These were the main findings:

- the model predictions slightly under estimated the capacity of the water curtain
- there were uncertainties regarding the water curtain properties. Attempts were made in order to measure these properties, but the attempts did not succeed. More detailed measurements are necessary in order to present a verified model for engineering use
- for the extreme situations of an underestimate of drop sizes, where the actual drop sizes are 50% larger than estimated, or where the actual small drop fraction is doubled, calculation errors will be caused in the range -7% to +18%, in absolute terms
- the calculation model is not capable of identifying irregularities within the water curtain. This will have importance relating to maximum allowable radiation limits where people are exposed
- the effect of wind on turbulent oil, gas and water flows in air, and their interaction during combustion, should be studied in greater detail

Chapter 9

Recommendations for further work

One of the main focuses ahead should be on the water curtain properties. Most of this work can be carried out under controlled laboratory conditions. There is generally very little knowledge of drop size distributions for the different nozzles producing water curtains. This is not a fixed distribution, even for a single nozzle type. Since the water droplet distribution produced is a function of pressure and ambient conditions, especially air movement of any kind (wind, turbulence), in addition to the geometry of the nozzle itself, varying size distributions will be produced. The manufacturers of the nozzles do not supply this kind of information.

In order to assess the efficiency of a water curtain, it will thus be necessary to measure the drop size distributions for different pressures for a number of nozzles. In addition, it is necessary to study the interaction between the droplets and the ambient, especially for cooling systems offshore, where the ambient may be the single most important factor for the functioning of a system, more than the nozzle arrangement or the water flows and pressures themselves.

Also, the general water curtain shape produced by the different nozzle arrangements should be studied more in detail. The density will vary in different areas of the curtain. A description of this, e.g by identifying holes in the curtains and more dense/less dense sectors should be studied.

This is only one small step towards obtaining knowledge about the efficiency of water curtains for full scale flaring. A lot more measurements should be carried out. Only through the collection of a large number of data for different flares and water curtains, a reliable tool can be made.

Appendix A

- Water curtain - Stage 1 measurements

Test, stage 1, Flare Boom Cooling System
Measurements

P1 = booster pump inlet pressure
P2 = booster pump outlet pressure
P3 = 6" pipe pressure at 3 m downstream from hose connection
P4 = pressure at nozzle furthest upstream

Situation	
1	All valves closed, pontoon pump running
2	Rig side cooling. Deluge pump running
3	Rig side cooling. Deluge and booster pump running
4	Flare boom and rig side cooling. Deluge and booster pump running
5	Flare boom and forward rig side cooling. Deluge and booster pump running
6	Flare boom cooling. Deluge and booster pump running
7	Flare boom cooling. 2 deluge pumps and booster pump running
8	Flare boom cooling. Port deluge pump and starboard booster pump running

Situation	Variable	Calculated value	Port			Starboard			Unit
			Measured value	Absolute deviation	Rel. to calc.(%)	Measured value	Absolute deviation	Rel. to calc.(%)	
1	P2		6,2			7,0			bar
2	P2		6,0			6,0			bar
3	P1	5,0	6,3	1,3	126	5,5	0,5	110	bar
	P2		12,2			12,0			bar
	I_{in}		129,7			137,0			A
	I_{steady}		80,9			96,0			A
	P					46,6			kW
	kVA					78,3			kVA
4	P1	4,6	2,4	-2,2	52	1,5	-3,1	33	bar
	P2	9,2	7,2	-2,0	78	7,0	-2,2	76	bar
	P3	8,9	6,8	-2,1	76	6,8	-2,1	76	bar
	P4	7,8	5,8	-2,0	74				bar
	I_{in}								A
	I_{steady}		174,6			172,0			A
	P					45,0			kW
	kVA								kVA
	Q	119	69,0	-50,0	58	77,0	-42,0	65	l/s
	v		3,6			4,0			m/s
5	P1	4,6	3,1	-1,5	67	2,1	-2,5	46	bar
	P2		8,1			7,8			bar
	P3		7,7			6,6			bar
	P4		6,1						bar
	I_{in}								A
	I_{steady}		164,0						A
	P		42,7						kW
	kVA		79,2						kVA
	Q		71,0						l/s
	v		3,7						m/s
6	P1	4,8	4,0	-0,8	83	3,2	-1,6	67	bar
	P2		9,3			9,3			bar
	P3		8,9			8,4			bar
	P4		7,2						bar
	I_{in}		(525)						A
	I_{steady}		154-160						A
	P		41,4			40,0			kW
	kVA		71,4						kVA
	Q		75,6			86,0			l/s
	v		5,0			4,7			m/s

7	P1	5,0		3,5	-1,5	70	bar
	P2	9,9		9,5	-0,4	96	bar
	P3	9,6		8,8	-0,8	92	bar
	P4	8,2					bar
	I_{in}			(525)			A
	I_{steady}						A
	P						kW
	kVA						kVA
	Q	119		96,0	-23,0	81	l/s
	v			5,1			m/s
8	P1	4,8		3,3	-1,5	69	bar
	P2	9,2		9,3	0,1	101	bar
	P3	8,9		8,8	-0,1	99	bar
	P4	7,8		8,0	0,2	103	bar
	I_{in}			404,0			A
	I_{steady}			150,0			A
	P						kW
	kVA						kVA
	Q	119		96,0	-23,0	81	l/s
	v			5,1			m/s

Note: The pressures, P1, are based on Lux Brannteknologi report no. H-R-03-004, repeated in WCN report 3813-11-05, rev. 2., section 4.5.
Values are estimated for less flow in situations 3, 6, 7 and 8 within the boundaries stated in the above mentioned section

Bibliography

[1] Wikipedia on internet

[2] Cowley, L.T.; Johnson, A.D.
Blast and Fire Engineering Project for Topside Structures, Fire Loading series,
Shell International Research Mij. BV, Feb, 1991

[3] Log, T.
Radiant Heat Attenuation in Fine Water Sprays,
InterFlam96, 26-28 March 1996, pp 425-434

[4] Bird, R.B.; Stewart, W.E.; Lightfoot, E.N.
Transport phenomena,
John Wiley & Sons, 1960

[5] Drysdale, D.
An Introduction to Fire Dynamics,
John Wiley & Sons Ltd, 1996

[6] McGuire, J.H.
Heat Transfer by Radiation,
Fire Research Special Report No.2, HMSO, London, 1953

[7] Hottel, H.C.; Sarofim, A.F.
Radiative Transfer,
McGraw-Hill, New York, 1967

[8] Hale, G.M.; Querry, M.R.
Optical Constants of Water in the 200-nm to 200-μm Wavelength Region,
Applied Optics, 12(3), 555-63, 1973

[9] Weast, R.C.; Strasser, A.; Grumer, J.
CRC Handbook of Chemistry and Physics,

58th ed., CRC Press Inc., West Palm Beach, Florida, 1977

[10] Mawhinney, J.R.; Dlugogorski, B.Z.; Kim, A.K.
A Closer Look at the Fire Extinguishing Properties of Water Mist,
Proc. 4th IAFSS Symp. on Fire Safety Science, Ottawa, Canada, 47-60, 1994

[11] Mawhinney, J.R.
Design of Water Mist Fire Suppression Systems for Shipboard Enclosures,
in Proc. Int.Conf. Water Mist Fire Sup. Systems, Borås, Sweden, 1993

[12] Ravigururajan, T.S; Beltran, M.R.
A model for Attenuation of Fire Radiation Through Water Droplets,
Fire Safety Journal, 1989, pp 171-181

[13] Coppale, A.; Nedelka, D.; Bauer, B.
Fire Protection; Water Curtains,
Fire Safety Journal, 20, 241-55, 1993

[14] Schuster, A.
Astrophysical J.,
21, 1-22, 1905

[15] van de Hulst, H.C.
Light Scattering by Small Particles,
Dover Publ., N.Y., USA, 1981

[16] Log, T.
Responstider for Temperaturdetektorer til Vanntåkesystem ved Brannbeskyttelse av Stavkirker etc,
Report, 1990

[17] Log, T.; Cannon-Brookes, P.
Water Mist for Fire Protection of Historic Buildings and Museums,
Museum Management and Curatorship, 13 (in press)

[18] Braidech, M.M.; Neale, J.J.; Matson, A.F.; Dufour, R.E.
The Mechanism of Extuingishment of Fire by Finely Divided Water,
U.L Inc. for the National Board of Fire Protection, N.Y., 73 p, 1955

[19] Rasbash, D.L.; Rogowski, Z.W.; Stark, G.W.V.
Mechanisms of Extinction of Liquid Fuel Fires with Water Sprays,
Combustion and Flame 4, 223-234, 1960

[20] Wighus, R.; Aune, P.; Drangsholt, G; Stensaas, J.P.
Full Scale Water Mist Experiments,
Proc. of the Int. Conf on Water Mist Fire Suppression Systems, Borås, Sweden, Nov. 4-5, 1993

[21] Log, T.
Radiant Heat Attenuation in Spray Shields,
Attachment to Lux Branntеknologi report H-R-03-004, 2003